

A Diffused Interface Non-local Crystal Plasticity Model to Capture Hall-Petch Effect in Polycrystals

A Thesis Submitted

in Partial Fulfillment of the Requirements

for the Degree of

Master of Technology

by

Devesh Tiwari

19101016



**DEPARTMENT OF AEROSPACE ENGINEERING
INDIAN INSTITUTE OF TECHNOLOGY, KANPUR**

August 2021

CERTIFICATE

It is certified that the work contained in the thesis titled "**A DIFFUSED INTERFACE NON-LOCAL CRYSTAL PLASTICITY MODEL TO CAPTURE HALL-PETCH EFFECT IN POLYCRYSTALS**," by **Devesh Tiwari** has been carried out under my supervision and that this work has not been submitted elsewhere for a degree.

Date: 23 August 2021

Dr. Pritam Chakraborty

(Thesis Supervisor)

Assistant Professor

Department of Aerospace Engineering

Indian Institute of Technology Kanpur

DECLARATION

This is to certify that the thesis titled "**A DIFFUSED INTERFACE NON-LOCAL CRYSTAL PLASTICITY MODEL TO CAPTURE HALL-PETCH EFFECT IN POLYCRYSTALS**," has been authored by me. It presents the research conducted by me under the supervision of **Dr. Pritam Chakraborty**.

To the best of my knowledge, it is an original work, both in terms of research content and narrative, and has not been submitted elsewhere, in part or in full, for a degree. Further, due credit has been attributed to the relevant state-of-the-art and collaborations (if any) with appropriate citations and acknowledgements, in line with established norms and practices.

Signature

Name: Devesh Tiwari

Programme: MTech

Department: Aerospace Engineering

Indian Institute of Technology Kanpur

Kanpur, 208016

ABSTRACT

Grain Boundaries (GBs) have a strong influence on the elasto-plastic behavior of polycrystals by affecting the transmission of dislocations across them. The inhibition of dislocation transmission across the GBs results in pile-up of dislocations which can develop additional resistances to slip leading to size dependent elasto-plastic response of polycrystals. In this work, we propose a diffused interface based non-local Crystal Plasticity (CP) model to capture the GB micro-mechanics and its effect on the elasto-plastic behavior. The model introduces a finitely thick grain boundary region incorporating the properties of all the adjoining grains. The GB model is based on penalising the slip rate on the slip systems of single crystals in the GB region with an extra activation energy term. The energy penalty is based on minimizing the remnant dislocation line on GB for the incoming and outgoing slip systems. Moreover, the energy penalty is modelled to evolve with slip accumulation to account for the saturation of remnant dislocations on GB. Owing to the non-uniformity of plastic flow in the GB regions, the deformation behavior becomes heterogeneous and results in the formation of Geometrically Necessary Dislocations (GNDs). The GNDs are incorporated in the CP model in addition to the Statistically Stored Dislocations (SSDs) which render the model size dependent.

The model has been implemented in a CP Finite Element Method (FEM) code and used to analyze the quasi-static deformation behavior of two dimensional polycrystal domains subjected to uni-axial tensile strain. The simulation results show that the model is able to capture the Hall-Petch behavior in polycrystals. The effect of misorientation of grains on Hall-Petch factor is also verified. The computational results are discussed and compared with experimental observations.

ACKNOWLEDGEMENT

I would like to express my deepest gratitude to my thesis supervisor **Dr. Pritam Chakraborty** for his guidance and constant support in my academic research as well as in personal life. The space and freedom provided by him helped me to grow and develop the foundations for independent research skills. It was a real privilege and honor for me to share of his exceptional scientific knowledge but also of his extraordinary human qualities.

My sincere thanks to **Dr. Daniel Paquet** for his constant support, availability and technical contributions, which were determinant for the accomplishment of work presented in the thesis.

Special thanks to my labmates Shalvi, Nazim, Mustafa, Vipin, Shivnag, Jothi and Selva for their companionship and for providing a so pleasurable and friendly working atmosphere. I am also truly thankful for their always prompt help, whenever I needed it.

I am also thankful to my friends Kavindra, Akshat, Atul, Saurav, Ratnesh, Radhika and Vishakha who made my life at IITK cherishable forever. The moments of leisure shared together helped to overcome the difficult moments with laughter and joy.

My joy knows no bounds in expressing my cordial gratitude to my sister and brother-in-law for being with me through thick and thin. Finally, I would like to thank my parents and my brother for their love and encouragement throughout my life and without whom this work would not have been possible.

DEDICATION

To my niece, *Nitya*

"the sweet little sunshine"

Seeing your smile always brings smile upon others.

TABLE OF CONTENTS

	Page
ACKNOWLEDGEMENTS	v
LIST OF FIGURES	xii
LIST OF TABLES	xiii
Chapter 1: Introduction	1
1.1 Objectives of the Thesis	5
1.2 Outline of the Thesis	5
Chapter 2: CPFEM Based Non-local GB Model and Numerical Implementation	6
2.1 Kinematics	6
2.2 Single Crystal Constitutive Model	8
2.3 GB Region Constitutive Model	10
2.4 Numerical Implementation	18
2.4.1 Calculation of Nye's Dislocation Tensor	21
Chapter 3: Numerical Study Using a Two-Grain Representative Volume . .	24
3.1 Problem Description	24
3.2 Reduced Slip Systems of FCC Single Crystal in Plane Strain	25
3.3 Convergence Study	27
3.3.1 Optimal Physical Thickness of GB Region	28
3.3.2 Converged Time Step Size	31
3.3.3 Mesh Sensitivity Analysis	32
3.4 Verification of Single Crystal Effect	33
3.5 Independence of GB Resistance to Relative Orientation of Grains	37
3.6 Initialization of Size Dependent GND Density in a Microstructure	41

3.7	Hall-Petch Effect in Bicrystal	43
3.7.1	Spatial Variation of CPFEM Variables under Bicrystal Deformation	46
3.8	Effect of Misorientation of Grains on Hall-Petch Behavior	62
3.9	Effect of Energy Penalty Evolution	65
Chapter 4:	Hall-Petch Effect in Polycrystals	68
4.1	Model Description	68
4.2	Verification of Hall-Petch Effect	70
4.3	Spatial Variation of CPFEM Variables under Polycrystal Deformation . .	71
4.3.1	Slip System Resistance Components	71
4.3.2	Components of Plastic Strain	73
4.3.3	Components of Stress	76
4.4	Orientation Dependent Yielding of Grains in a Polycrystal	78
4.5	Discussion of Experimentally Observed Hall-Petch Effect	81
Chapter 5:	Conclusion and Future Scope	83
5.1	Conclusion	83
5.2	Scope of Future Work	85
REFERENCES	89

LIST OF FIGURES

Figure	Title	Page
2.1	Decomposition of deformation gradient.	6
2.2	Schematic illustration of a hypothetical slip transmission event at a triple point. A_1 to A_4 , B_1 to B_4 and C_1 to C_4 represent the slip systems of the grains A, B and C respectively.	12
2.3	Schematic of slip transmission event across GB in a bicrystal.	16
2.4	Schematic of four noded element with four Gauss points.	22
3.1	Schematic of a bicrystal in plane strain condition and subjected to uniaxial loading.	24
3.2	Reduced slip systems for FCC crystal for 2D plane strain CPFEM simulations. Plane of loading is highlighted in yellow. N_1 to N_4 are the slip plane normals. M_1 to M_8 are the modified slip directions. A_1 to A_3 , B_1 to B_3 , C_1 to C_3 and D_1 to D_3 are the original slip directions on the octahedral planes.	26
3.3	Effect of physical thickness of the GB region on macroscopic stress-strain response. D represents the grain diameter.	28
3.4	GB thickness convergence with two different grain size without considering the effect of GND. (a) macroscopic stress vs strain and (b) maximum of all the slip system resistances due to SSDs.	30
3.5	Macroscopic stress-strain response for three different sizes of time step.	31
3.6	Macroscopic stress-strain response for three different element sizes of finite element mesh.	33
3.7	(a) Comparison of macroscopic stress vs strain between bicrystal with zero misorientation and single crystal. Comparison of (b) maximum of all slip system resistances caused by GNDs, (c) maximum of all slip system resistances caused by SSDs, (d) maximum of all total slip system resistances, (e) normal stress component in the loading direction, and (f) normal strain component in the loading direction, between bicrystal with zero misorientation and single crystal on a line $(0, L_2/2)$ to $(L_1, L_2/2)$ at applied uniaxial strain of 1%.	36
3.8	Two bicrystals with the following grain orientations: (a) Euler angle of left grain = 45° and right grain = 0° ; (b) Euler angle of left grain = 0° and right grain = 45°	37

3.9 (a) Comparison of macroscopic stress vs strain between the bicrystals with different orientations. Comparison of (b) maximum of all slip system resistances caused by GNDs, (c) maximum of all slip system resistances caused by SSDs, (d) maximum of all total slip system resistances, (e) normal stress component in the loading direction, and (f) normal strain component in the loading direction, between the bicrystals with different orientations on a line $(0, L_2/2)$ to $(L_1, L_2/2)$ at applied uniaxial strain of 1%.	40
3.10 Macroscopic stress-strain response for unloading-reloading technique applied to (a) elasto-plastically deformed specimen, and (b) elastically deformed specimen, for initializing the size dependent GND density in a microstructure.	42
3.11 Distribution of maximum slip system resistance due to GND amongst all the slip systems after unloading for the bicrystal with grains having 45° and 0° Euler angles. (a) Contour, and (b) line plot along $(0, L_2/2)$ to $(L_1, L_2/2)$.	43
3.12 Bicrystal microstructure used for verifying the Hall-Petch effect. In the bicrystal the Euler angle of the left grain = 45° and the Euler angle of the right grain = 0° .	44
3.13 Effect of grain size on yield stress of the material. (a) Macroscopic stress-strain response for three different grain sizes; (b) Hall-Petch slope at three different strain levels.	46
3.14 Variation of accumulated slip on the slip system having the maximum value for a bicrystal with Euler angle of left grain = 45° and Euler angle of right grain = 0° at applied uniaxial strain of 1%. (a) Contour plot and (b) variation on a line $(0, L_2/2)$ to $(L_1, L_2/2)$.	48
3.15 Variation of accumulated slip on individual slip systems for a bicrystal with Euler angle of left grain = 45° and Euler angle of right grain = 0° . (a) to (h) represent the eight slip systems of the grains.	49
3.16 Variation of maximum GND based slip system resistance amongst all the slip systems at 1 % applied strain for the bicrystal with grains having 45° and 0° Euler angles. (a) Contour, and (b) line plot along $(0, L_2/2)$ to $(L_1, L_2/2)$.	50
3.17 Variation of maximum SSD based slip system resistance amongst all the slip systems at 1 % applied strain for the bicrystal with grains having 45° and 0° Euler angles. (a) Contour, and (b) line plot along $(0, L_2/2)$ to $(L_1, L_2/2)$.	51
3.18 Variation of maximum total lip system resistance amongst all the slip systems at 1 % applied strain for the bicrystal with grains having 45° and 0° Euler angles. (a) Contour, and (b) line plot along $(0, L_2/2)$ to $(L_1, L_2/2)$.	52
3.19 Variation of maximum GND density amongst all the slip systems at 1 % applied strain for the bicrystal with grains having 45° and 0° Euler angles. (a) Contour, and (b) line plot along $(0, L_2/2)$ to $(L_1, L_2/2)$.	54

3.20 Variation of maximum SSD density amongst all the slip systems at 1 % applied strain for the bicrystal with grains having 45° and 0° Euler angles. (a) Contour, and (b) line plot along $(0, L_2/2)$ to $(L_1, L_2/2)$	55
3.21 Variation of ϵ_{11}^p at 1 % applied strain for the bicrystal with grains having 45° and 0° Euler angles. (a) Contour, and (b) line plot along line A-B.	56
3.22 Variation of ϵ_{22}^p at 1 % applied strain for the bicrystal with grains having 45° and 0° Euler angles. (a) Contour, and (b) line plot along line A-B.	57
3.23 Variation of ϵ_{33}^p at 1 % applied strain for the bicrystal with grains having 45° and 0° Euler angles. (a) Contour, and (b) line plot along line A-B.	57
3.24 Variation of ϵ_{12}^p at 1 % applied strain for the bicrystal with grains having 45° and 0° Euler angles. (a) Contour, and (b) line plot along line A-B.	58
3.25 Variation of σ_{11} at 1 % applied strain for the bicrystal with grains having 45° and 0° Euler angles. (a) Contour, and (b) line plot along $(0, L_2/2)$ to $(L_1, L_2/2)$	59
3.26 Variation of σ_{22} at 1 % applied strain for the bicrystal with grains having 45° and 0° Euler angles. (a) Contour, and (b) line plot along $(0, L_2/2)$ to $(L_1, L_2/2)$	60
3.27 Variation of σ_{33} at 1 % applied strain for the bicrystal with grains having 45° and 0° Euler angles. (a) Contour, and (b) line plot along $(0, L_2/2)$ to $(L_1, L_2/2)$	61
3.28 Variation of σ_{12} at 1 % applied strain for the bicrystal with grains having 45° and 0° Euler angles. (a) Contour, and (b) line plot along $(0, L_2/2)$ to $(L_1, L_2/2)$	62
3.29 Bicrystal microstructures to evaluate the influence of misorientation on Hall-Petch behavior. (a) Grains having Euler angles of 30° and 0° , and (b) Grains having Euler angles of 15° and 0°	63
3.30 Misorientation effect in bicrystal. (a) Macroscopic stress vs strain for three grain sizes and (b) Variation of yield stress with grain size highlighting Hall-Petch behavior.	64
3.31 Effect of energy penalty evolution on macroscopic response.	66
3.32 Evolution of energy penalty for individual slip systems of $45^\circ - 0^\circ$ bicrystal.	66
 4.1 (a) Distribution of Euler angles in the polycrystalline domain. (b) Geometrical parameters of the polycrystal domain and FEM mesh.	69
4.2 (a) Macroscopic stress strain response on the polycrystal for four different grain sizes. (b) Variation of yield stress with grain size highlighting Hall-Petch behavior.	70
4.3 Spatial distribution of maximum slip system resistance amongst all the slip systems at applied strain of 0.5%. (a) g_{SSD} , (b) g_{GND} , and (c) total slip resistance.	73
4.4 Spatial distribution of components of plastic strain (a) ϵ_{11}^p , (b) ϵ_{22}^p , (c) ϵ_{33}^p and (d) ϵ_{12}^p for uniaxial plane strain deformation of polycrystal at applied strain of 0.5%.	75

4.5 Spatial distribution of components of Cauchy stress (a) σ_{11} , (b) σ_{22} , (c) σ_{33} and (d) σ_{12} for uniaxial plane strain deformation of polycrystal at applied strain of 0.5%	78
4.6 Orientation dependent yielding of grains.	80

LIST OF TABLES

Table	Title	Page
2.1	Hypothetical slip transmission event at a triple point.	13
2.2	Parameters of the non-local grain boundary model.	17
3.1	Reduced slip systems of FCC crystal for 2D plane strain CPFEM simulations.	27
3.2	Hall-Petch slopes at three different strain levels for a bicrystal with 45° misorientation.	46
3.3	Effect of misorientation of grains on Hall-Petch behaviour.	65
4.1	Hall-Petch constants for 16 grain polycrystal	71
4.2	Comparision of Hall-Petch parameters for Aluminum	81

CHAPTER 1

Introduction

The micro-mechanical analysis of polycrystalline aggregates plays a crucial role in understanding of materials. The trend of product miniaturization and need for the development of high strength metallic alloys has motivated researchers over last few decades to develop better simulation models that can reduce the material design time and number of experiments. The plastic deformation in metallic alloys is mainly caused by the motion of dislocations under the effect of applied shear stress when it reaches a critical value termed as critical resolved shear stress. Any obstructions offered to the motion of these dislocations leads to strengthening of the alloys. The slipping of dislocations is preferred on some specific planes (having highest planer density) and in specific directions (having highest linear density), collectively known as slip systems. It makes the local plastic deformation mechanism of individual crystals anisotropic. The traditional phenomenological plasticity models such as J_2 plasticity theory, an isotropic plasticity model, cannot account for the anisotropic and heterogeneous nature of microscale deformation. Whereas, in crystal plasticity theory that is widely used for analysing deformation mechanism at mesoscales, the very inhomogeneous anisotropic behaviour of plasticity is introduced into the plastic deformation tensors by incorporating the preferred slip directions and planes.

The micro-structure of metallic alloys consist of randomly orientated grains of different sizes and the interfaces separating them termed as grain boundaries (GBs). To study the polycrystalline plasticity, Taylor [1] first proposed a fully constrained model for relationship between texture evolution and crystallographic slip. Study of texture evolution in metal forming operations has been studied and validated by Asaro and Needleman [2] and Harren et al. [3] using the Taylor-type polycrystal model. In his approach, based on the assumption that the local deformation of each grain matches with the global deformation, the compatibility condition in the polycrystal and the equilibrium conditions in each grain are trivially satisfied. However, the equilibrium condition between the neighbouring

grains is violated that yields a stiffer response. To address the inherent shortcomings of Taylor's model, self-consistent scheme was developed by Kroner's [4] and Budiansky et al. [5]. In this class of models, each grain of a polycrystal is treated as an inclusion within the matrix of all surrounding grains having a average response. Variants of these models were also developed by relaxing some of the strain constraints [6; 7] that up-to certain extent of accuracy can predict mechanical behaviour and texture evolution. However, these conventional models can only provide a reasonable estimate of the effective response of a polycrystal due to deformation of underlying single crystals and they fail to capture the inter-granular variations of state. Therefore, these models are mostly usable for capturing texture evolution during metal forming processes or any other macroscopic response where the intergranular variations can be ignored. To capture these variations, Crystal Plasticity based Finite Element Method (CPFEM) has received significant attention. A review article by D. Raabe et al. [8] presents a wide range of applications where CPFEM has been successfully used. Most of the CPFEM studies of polycrystal mechanics use rather simple constitutive formulations where flow and hardening rule are expressed as power laws [9]. Although these power law descriptions are useful simplifications of the visco-plastic response of polycrystals, under dynamic loading conditions and at simulation scales that can exhibit size effects, they reveal some disadvantages demanding for the development of better constitutive laws to model anisotropic response of polycrystals [10].

GBs predominantly govern the mechanical properties of polycrystalline materials by modifying the deformation mechanism in two ways. First, they lead to the formation of dislocation pile-ups which cause an increase in the critical resolved shear stress for further dislocation slip and, thus, leads to the well known Hall-Petch behaviour [11; 12]. Second, they promote heterogeneous deformation of single crystals within the polycrystal [13; 14; 15]. The GB micro-mechanics is important to understand in both the cases to model mechanical response of polycrystals. The non-homogeneous plastic deformation stimulated by GBs leads to development of strain and orientation gradients. Hossen et al. have experimentally verified the GB induced hardness gradient during nano-indentation in BCC metals [16]. The development of strain gradients during deformation can lead

to the accumulation of Geometrically Necessary Dislocations (GNDs) in addition to the Statistically Stored Dislocations (SSDs) which mainly accounts for the statistically averaged homogeneous deformation within the single crystal [17]. The SSDs mainly evolve in the grain interior region as a result of less obstructed and more intensive plastic flow in that region, while the GNDs are more concentrated near GBs because of the lattice mismatch between neighbouring grains [18]. Moreover, the local constitutive models should be extended to non-local ones, which can consider the interplay between texture and dislocation evolution on the basis of different behavior of neighboring material points. Since local crystalline orientation gradients are necessarily associated with the storage of GNDs, it is an obvious requirement that a non-local constitutive model should be built based on dislocation densities rather than on empirical hardening functions. S.Ghosh et al. have suggested a coupled equation for the evolution of SSDs and GNDs in which the GNDs are evaluated as a function of Nye's dislocation tensor that is evaluated from the curl of plastic deformation tensor (closure failure) [19]. The Nye's dislocation tensor can be used to express the constraints imposed on a material point by its neighbourhood. The inherent length scale associated with GNDs also renders the model scale sensitive. The scale dependence of mechanical response of polycrystalline materials has also been verified experimentally [20; 21]. Many efforts have been devoted over the last few decades to develop the gradient plasticity theories based on GNDs to capture these experimentally observed size effects [22; 23; 24; 25]. However, for the models which aim to capture the size effect with the intrinsic length scale associated with GNDs, the initial yield stress of polycrystals appears to be independent of the grain size because the GNDs evolve with the applied strain and hence the initial responses depend only on the initial SSD density. To address this, some grain size dependent initial GND density should also be stored to account for initial micro-structure [26]. W.A. Counts et al. have introduced an initial fictitious deformation to determine the initial GND state [27], whereas Evers et al. have expressed GND density in terms of GB dislocation densities having similar geometrical nature [28].

The grain boundary strengthening mechanism depends mainly on influential factors such as crystallographic lattice rotation, grain misorientation [29] and ease of slip trans-

mission across GBs [30]. Depending upon the orientation and structure, the GBs can partially or completely obstruct the motion of dislocations across interfaces. However, very few existing models elucidate the effect of GB micro-mechanics on elasto-plastic deformation behaviour. Ma et al. introduced an energy penalty based GB CPFEM model with a separate GB element to elucidate the dislocation interaction with GBs for a bicrystal interface [31]. In their model half of the gauss points in the GB element are assigned the properties of one crystal while the other half of gauss points are assumed to reside in the other crystal. However, this representation restricts the shape of the GB to the sides of a square grain as well allow only one element to mesh the GB. Moreover, in realistic problems the interfaces may exist as multigrain junctions and the GB elements must incorporate the properties of all the adjoining grains. The representation provided in [31] would fail to capture this scenario. The energy penalty must also evolve with the dislocation accumulation to model the additional barrier offered by piled-up dislocations for further incoming dislocations. Peng et al. have proposed the evolution of GB energy in a work-conjugate gradient crystal plasticity framework [32]. However, in such models the GNDs are solved as additional degrees of freedom making it computationally inefficient.

Traditionally, the CPFEM analysis is done using sharp GBs. The term sharp indicates the jump in response and phase variables across the interface. However, the sharp representation creates difficulty to incorporate physical models of grain boundary behavior and microstructure evolution [33]. In further advancements, stepped interfaces are used in which the elements are assigned to either of the grains, thus rendering a stepped structure of the interface. A stepped interface is still sharp but without a smooth geometry. Hojun Lim et al. observed that the voxelated (stepped) interface, at the local level, in contrast to the smooth interfaces, showed some fake stress concentrations, which affects in determining the damage mechanism such as crack initiation [34]. To address the issues related to a suitable representation of the GB region both to avoid numerical errors as well as to incorporate a suitable GB constitutive law, a diffused interface model an energy penalty based diffused interface GB model is developed in this thesis. The specific objectives of this work are presented next.

1.1 Objectives of the Thesis

Based on the observed deficiencies in micro-mechanical modelling of polycrystals using CPFEM, the following tasks have been identified:

- To develop a non-local CPFEM model for capturing elasto-plastic behaviour of polycrystal.
- To develop a diffused interface GB model.
- To capture the Hall-Petch effect for polycrystals using the model.

1.2 Outline of the Thesis

The thesis is organised as follows:

Chapter 1: A brief introduction of the current status of micro-mechanical modelling of polycrystalline aggregates is provided. Background and motivation of the thesis is discussed based on the literature survey of existing models.

Chapter 2: Details of CPFEM based non-local GB model are discussed. Basics of CP framework, dislocation interaction based flow rule of gradient plasticity and concept of energy penalty based GB model are explained. The numerical implementation of grain boundary CPFEM is also discussed in this chapter.

Chapter 3: Results of various case studies for the bicrystal problem are discussed. The Hall-Petch behaviour and the effect of misorientation of grains is presented for bicrystal problem.

Chapter 4: Hall-Petch effect is verified for polycrystals. The simulation results are discussed in reference to experimental data available in literature.

Chapter 5: The thesis is concluded and the scope of future work is discussed.

CHAPTER 2

CPFEM Based Non-local GB Model and Numerical Implementation

2.1 Kinematics

Many useful materials, such as conventional structural metals, can carry only very small amounts of elastic strain. We can take advantage of this behavior to simplify the description of the deformation of such a material. Since the behavior is so common, the assumption that the elastic strains are always small forms the basis of such inelastic material models. This section discusses the description of the deformation for this case.

A multiplicative decomposition is typically used in crystal plasticity where the deformation gradient $\underline{\underline{F}}$ is decomposed into elastic and plastic parts as (see Figure 2.1)

$$\underline{\underline{F}} = \underline{\underline{F}}^e \underline{\underline{F}}^p \quad (2.1)$$

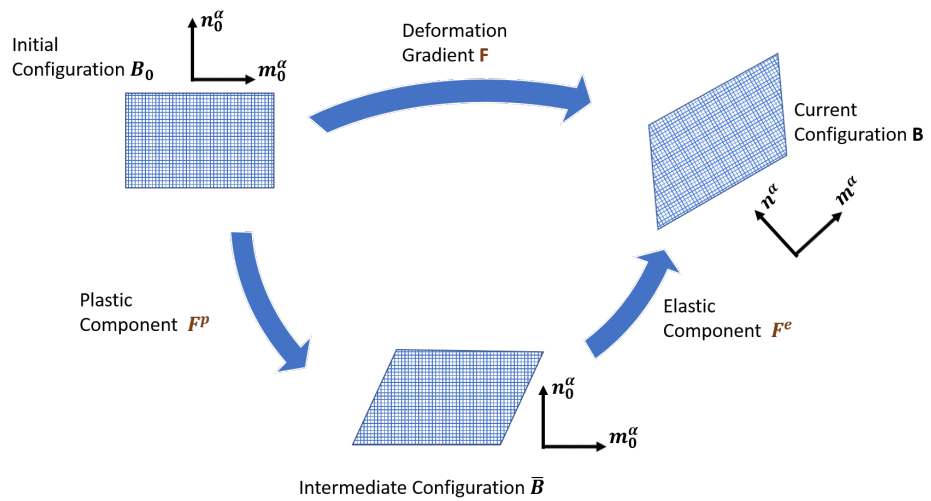


Figure 2.1: Decomposition of deformation gradient.

From Equation (2.1) we can obtain the velocity gradient as

$$\underline{\underline{L}} = \underline{\underline{L}}^e + \underline{\underline{F}}^e \cdot \underline{\underline{L}}_0^p \cdot \underline{\underline{F}}^{e-1} \quad (2.2)$$

where, $\underline{\underline{L}}^e = \dot{\underline{\underline{F}}}^e \cdot \underline{\underline{F}}^{e-1}$ and $\underline{\underline{L}}_0^p = \dot{\underline{\underline{F}}}^p \cdot \underline{\underline{F}}^{p-1}$ are the elastic and plastic velocity gradients respectively. For the materials of concern here, we now assume that the elastic strains $\underline{\underline{\epsilon}}^e$ are very small compared to unity. Using this together with the left polar decomposition of elastic deformation, we can write

$$\underline{\underline{F}}^e = \underline{\underline{V}}^e \cdot \underline{\underline{R}}^e = (\underline{\underline{I}} + \vartheta \underline{\underline{A}}) \cdot \underline{\underline{R}}^e \quad (2.3)$$

in which $|\vartheta| \ll 1$ and $A = A^T$, $\|A\| = 1$. We can use this decomposition of $\underline{\underline{F}}^e$ in Equation (2.2) to obtain

$$\underline{\underline{L}} = \underline{\underline{L}}^e + (\underline{\underline{I}} + \vartheta \underline{\underline{A}}) \cdot \underline{\underline{R}}^e \cdot \underline{\underline{L}}^p \cdot \underline{\underline{R}}^{eT} \cdot (\underline{\underline{I}} - \vartheta \underline{\underline{A}}) \quad (2.4)$$

Now we define, $\underline{\underline{L}} = \underline{\underline{D}} + \underline{\underline{W}}$, $\underline{\underline{L}}^e = \underline{\underline{D}}^e + \underline{\underline{W}}^e$ and $\underline{\underline{L}}^p = \underline{\underline{D}}^p + \underline{\underline{W}}^p$, where $\underline{\underline{D}}$ and $\underline{\underline{W}}$ denote the symmetric and antisymmetric parts of each velocity gradient respectively. Using these definitions and neglecting the higher-order term, the velocity gradient can now be expressed as

$$\begin{aligned} \underline{\underline{L}} &= \underline{\underline{D}}^e + \underline{\underline{W}}^e + \underline{\underline{R}}^e \cdot (\underline{\underline{D}}^p + \underline{\underline{W}}^p) \cdot \underline{\underline{R}}^{eT} \\ &\quad + \vartheta \underline{\underline{A}} \underline{\underline{R}}^e \cdot (\underline{\underline{D}}^p + \underline{\underline{W}}^p) \cdot \underline{\underline{R}}^{eT} - \vartheta \underline{\underline{R}}^e \cdot (\underline{\underline{D}}^p + \underline{\underline{W}}^p) \cdot \underline{\underline{R}}^{eT} \cdot \underline{\underline{A}} \end{aligned} \quad (2.5)$$

We are assuming small deformation in this work which results in $\underline{\underline{W}}^e = \underline{\underline{W}}^p = \underline{\underline{0}}$ and $\underline{\underline{R}}^e = \underline{\underline{I}}$ and reduces Equation (2.5) to

$$\dot{\underline{\underline{\epsilon}}} = \dot{\underline{\underline{\epsilon}}}^e + \dot{\underline{\underline{\epsilon}}}^p \quad (2.6)$$

where $\dot{\underline{\underline{\epsilon}}}^e$ and $\dot{\underline{\underline{\epsilon}}}^p$ are the elastic and plastic strain rates respectively.

2.2 Single Crystal Constitutive Model

The plastic strain rate in the grain interior (outside GB region) is modeled using the conventional single crystal constitutive law. In this model, the plastic strain rate is expressed in terms of the slip rate on different slip systems, following

$$\underline{\dot{\epsilon}}^p = \sum_{\alpha=1}^{n_{slip}^{int}} \dot{\gamma}^\alpha \underline{\underline{S}}_0^{\alpha sym} \quad (2.7)$$

where n_{slip}^{int} is the number of slip systems in the grain interior and $\dot{\gamma}^\alpha$ is the slip rate on each slip system. In Equation (2.7) the term $\underline{\underline{S}}_0^{\alpha sym}$ is the symmetric Schmid tensor given as

$$\underline{\underline{S}}_0^{\alpha sym} = \left[\frac{\underline{\underline{S}}_0^\alpha + \underline{\underline{S}}_0^{\alpha T}}{2} \right] \quad (2.8)$$

with

$$\underline{\underline{S}}_0^\alpha = \underline{\underline{m}}_0^\alpha \otimes \underline{\underline{n}}_0^\alpha \quad (2.9)$$

where $\underline{\underline{m}}_0^\alpha$ and $\underline{\underline{n}}_0^\alpha$ are slip direction and slip normal vectors of a slip system. In this work, the slip systems of the FCC crystal are reduced to a total number of 8 pseudo slip systems such that the out of plane plastic shear strains are zero. These reduced slip systems are presented in Section 3.2.

The slip rate on every slip system, α , is expressed using an activation enthalpy based flow rule adopted from [10] given by

$$\dot{\gamma}^\alpha = \dot{\gamma}_0^\alpha \exp \left[-\frac{Q_{slip}^\alpha}{k_B \theta} \left\{ 1 - \left(\frac{|\tau^\alpha|}{g^\alpha} \right)^p \right\}^q \right] sign(\tau^\alpha) \quad (2.10)$$

where Q_{slip}^α denotes the activation barrier to slip, $\dot{\gamma}_0^\alpha$ is the reference slip rate on slip system α , k_B represents Boltzmann's constant, θ is the absolute temperature in Kelvin, τ^α and g^α are the resolved shear stress and effective slip system resistance on slip system α respectively, p and q are modelling parameters. The resolved shear stress (τ) on the slip system α is expressed as

$$\tau^\alpha = \underline{\underline{\sigma}} : \underline{\underline{S}}_0^\alpha \quad (2.11)$$

where $\underline{\sigma}$ is the Cauchy stress tensor.

Material hardening is captured at slip system level through slip system resistance g^α in Equation (2.10). The orientation of the grains changes across GBs resulting in gradient of plastic strain at and near them. Due to these gradients, some extra amount of net dislocation must be stored in addition to the SSDs. Hence, the evolution of slip system resistance in this work is assumed to be controlled by two types of dislocations, viz. SSDs and GNDs. Based on this understanding, the hardening law used in this work assumes that the critical resolve shear stress g^α , initially equals g_0 and then evolves as

$$\dot{g}^\alpha = \sum_{\beta} h^{\alpha\beta} |\dot{\gamma}^\beta| + k_0 \frac{\hat{\alpha}^2 G^2 \|b\|}{2(g^\alpha - g_0^\alpha)} \sum_{\beta} \lambda^\beta |\dot{\gamma}^\beta| \quad (2.12)$$

The above equation for the evolution of slip system resistance is adopted from [19]. In the equation, the first and second terms correspond to the effect of SSDs and GNDs on work hardening respectively. Here k_0 and $\hat{\alpha}$ are dimensionless constants, b is the magnitude of burgers vector, G is the shear modulus, g_0^α is the initial slip system resistance. The term $h^{\alpha\beta}$ are the components of the hardening matrix capturing the influence of slip on the β_{th} slip system on the resistance of the α_{th} slip systems. A linear hardening model is considered in this work and is given by

$$h^{\alpha\beta} = h_0^\alpha q^{\alpha\beta} \quad (2.13)$$

$$q^{\alpha\beta} = \begin{cases} 1 & \text{if } \alpha = \beta \\ 1.4 & \text{otherwise} \end{cases} \quad (2.14)$$

The term λ^β in Equation (2.12) is a scalar measure of slip plane lattice incompatibility and can be expressed for each slip plane as a function of slip plane normal \underline{n}^β and incompatibility tensor $\underline{\underline{\Lambda}}$ as

$$\lambda^\beta = (\underline{\underline{\Lambda}} \underline{n}^\beta : \underline{\underline{\Lambda}} \underline{n}^\beta)^{\frac{1}{2}} \quad (2.15)$$

In the above equation, the dislocation density tensor $\underline{\underline{\Lambda}}$, also known as the Nye's dislocation tensor, is a measure of GND density. It can be expressed using the curl of the plastic

strain tensor as

$$\underline{\underline{\Lambda}} = \nabla^T \times \underline{\underline{\epsilon}}^p \quad (2.16)$$

The single crystal equations discussed above are modified in the GB region to incorporate the slip transmission mechanism across GB, which is discussed in the next section.

2.3 GB Region Constitutive Model

The GB model developed in this work is adopted from [31] and introduces a finitely thick diffused interface region at the GB having the properties of all the adjoining grains. This is achieved by assuming that the total number of slip systems in the GB region (n_{slip}^{GB}) is

$$n_{slip}^{GB} = n_{slip}^{int} n_{grain}^{GB} \quad (2.17)$$

where n_{grain}^{GB} is the count of number of grains lying within the GB region. A volume average term is introduced to find the averaged response of the constituent grains and is expressed as

$$v^{frac} = \left(\frac{1}{n_{grain}^{GB}} \right) \quad (2.18)$$

It is assumed that a material point at the GB region satisfies the stress equilibrium (uniform stress) and strain compatibility (uniform strain rate), while the plastic strain rate follows a mixture rule such that

$$\underline{\underline{\dot{\epsilon}}}^p = \sum_{i=1}^{n_{grain}^{GB}} v_i^{frac} \underline{\underline{\dot{\epsilon}}}_i^p \quad (2.19)$$

where $\underline{\underline{\dot{\epsilon}}}_i^p$ represents the plastic strain rate of constituent grain present in the GB region. The total plastic strain rate of a constituent grain is determined from the slip rate due to the activation of slip systems within that grain and the slip getting transmitted to it from different slip systems of the other constituent grains present in the GB region. Thus,

$$\underline{\underline{\dot{\epsilon}}}_i^p = \sum_{\alpha=1}^{n_{slip}^{int}} (\dot{\gamma}_{self}^\alpha + \dot{\gamma}_{trans}^\alpha) \underline{\underline{S}}_0^{\alpha sym} \quad (2.20)$$

where, $\dot{\gamma}_{self}^{\alpha}$ and $\dot{\gamma}_{trans}^{\alpha}$ are activated and incoming transmitted slip rates respectively, on slip system α of the i_{th} constituent grain. The slip rate contribution to a grain due to the activation of its slip systems is defined as

$$\dot{\gamma}_{self}^{\alpha} = \frac{1}{m^{\alpha}} \dot{\gamma}_0^{\alpha} \exp \left[-\frac{Q_{slip}^{\alpha} + Q_{GB}^{\alpha}}{k_B \theta} \left\{ 1 - \left(\frac{|\tau^{\alpha}|}{g^{\alpha}} \right)^p \right\}^q \right] \text{sign}(\tau^{\alpha}) \quad (2.21)$$

where Q_{GB}^{α} is an additional energy penalty due to the resistance offered by GB to transmit dislocations across it. The selection of slip system in the other grains for slip transmission is based on minimizing the remnant dislocation line on GB for incoming and outgoing slip systems and is discussed in Section 2.3. In Equation (2.21), m^{α} is the number of grains, including this grain, in which the activated slip rate is getting distributed. The concept of introducing this factor is based on a physical assumption that if the dislocations of slip system α in a grain in GB region finds a slip plane in some other constituent grain having the minimum energy penalty for slip transmission, then the slip rate of that slip system gets equally divided in all the shared grains. This also suggests that a transmitted slip rate for the other slip systems should also be considered and is given by

$$\dot{\gamma}_{trans}^{\alpha} = \sum_{\beta=1}^{n_{trans}} \frac{1}{n^{\alpha\beta}} \left(\dot{\gamma}_{self}^{\beta} \right) \quad (2.22)$$

where n_{trans} is the number of slip systems in other grains which transmit dislocations to the α slip system and $n^{\alpha\beta}$ is the number of slip systems in this grain to which a slip system β in the other grain is transmitting dislocation.

The distribution of transmitted slip is schematically explained below using Figure 2.2.

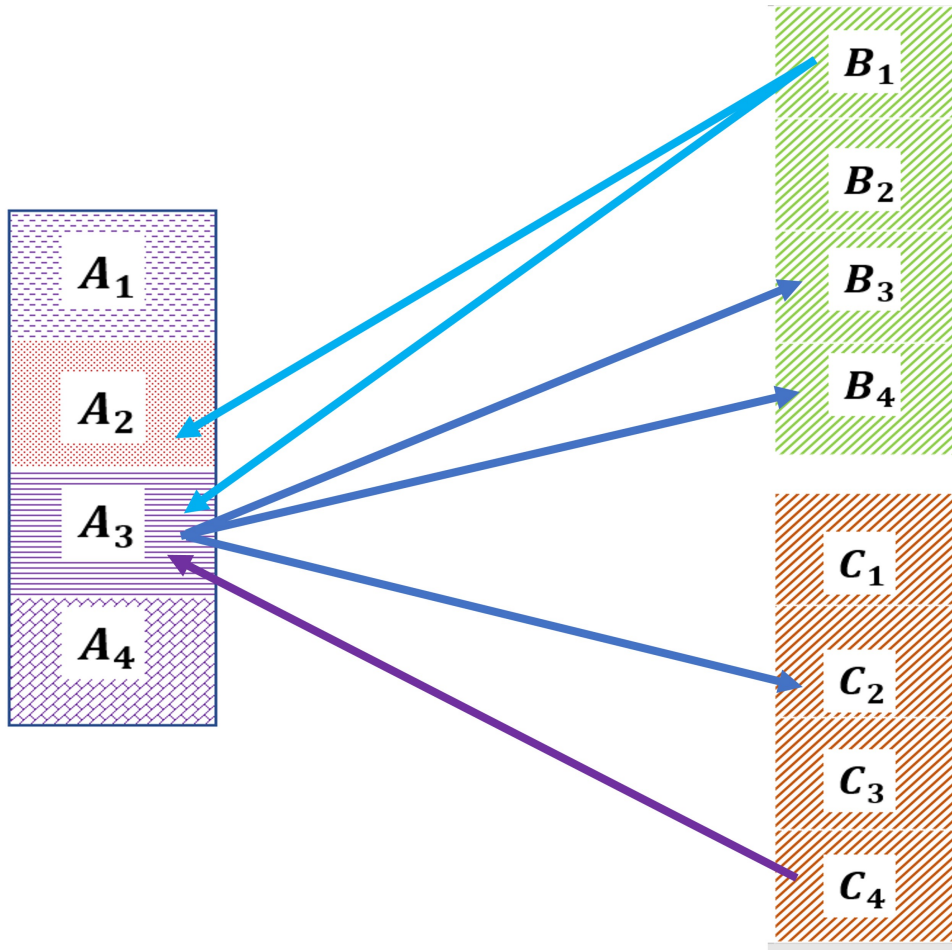


Figure 2.2: Schematic illustration of a hypothetical slip transmission event at a triple point. A_1 to A_4 , B_1 to B_4 and C_1 to C_4 represent the slip systems of the grains A, B and C respectively.

Consider a hypothetical slip transmission event shown in Figure 2.2. Here A , B and C represent three different grains and the four subdivisions in each of them represent four different slip systems belonging to them. The arrows show the direction of slip transmission. By looking at the figure we can say that the slip from 3^{rd} slip system of grain A is getting transmitted to (2^{nd}) slip system of grain C and also to $(3^{rd} \& 4^{th})$ slip systems of grain B . The 3^{rd} slip system of grain A is also receiving the slip getting transmitted from 4^{th} slip system of grain C and 1^{st} slip system of grain B which is also transmitting slip to 2^{nd} slip system of grain A . The table below shows various terms involved in the slip transmission formulation in Equations (2.19) to (2.22) for the hypothetical slip transmission events that may occur at a triple point and shown in Figure 2.2.

Table 2.1: Hypothetical slip transmission event at a triple point.

α^i	<i>Transmitting to</i>	m^α	<i>Receiving from</i>	m^β	$n^{\alpha\beta}$	Total slip
3^A	$3^B, 4^B$	3	1^B	2	2	$\dot{\gamma}^{3A} + \frac{1}{2} \cdot \dot{\gamma}^{1B} + \frac{1}{1} \cdot \dot{\gamma}^{4C}$
	2^C		4^C			
2^A	—	1	1^B	2	2	$\dot{\gamma}^{2A} + \frac{1}{2} \cdot \dot{\gamma}^{1B}$
1^B	$2^A, 3^A$	2	—	—	—	$\dot{\gamma}^{1B} + \frac{1}{2} \dot{\gamma}^{1B} + \frac{1}{1} \dot{\gamma}^{4C}$
3^B	—	1	3^A	3	2	$\dot{\gamma}^{3B} + \frac{1}{2} \cdot \dot{\gamma}^{3A}$
4^B	—	1	3^A	3	2	$\dot{\gamma}^{4B} + \frac{1}{2} \cdot \dot{\gamma}^{3A}$
2^C	—	1	3^A	3	1	$\dot{\gamma}^{2C} + \frac{1}{1} \cdot \dot{\gamma}^{3A}$
4^C	3^A	2	—	—	—	$\dot{\gamma}^{4C}$
<i>Total</i>	—	—	—	—	—	$\dot{\gamma}^{3A} + \dot{\gamma}^{2A} + \dot{\gamma}^{1B} + \dot{\gamma}^{3B} + \dot{\gamma}^{4B} + \dot{\gamma}^{2C} + \dot{\gamma}^{4C}$

From the last entry shown in Table 2.1, we can also verify that the total slip rate is redistributed but it remains conserved. The evolution of slip system resistance in a grain at the GB region is obtained from Equations (2.13) and (2.14), and is assumed to be only affected by the self and latent hardening of other slip systems in that grain only.

Grain Boundary Energy Penalty

The GB energy penalty appearing in Equation (2.21) is given by

$$Q_{GB}^\alpha = Q_{0-GB}^\alpha (1 + k_q \gamma_a^\alpha) \quad (2.23)$$

where, Q_{0-GB}^α is the energy penalty applied to account for the GB barrier based on minimizing the remnant dislocation line on GB for incoming and outgoing slip systems. This additional energy for the transmission event is the energy of formation of GB dislocations which are left as debris during the penetration event. The GBs can absorb these debris dislocations up to certain extent but as the concentration of these GB dislocations keep on increasing the GBs can not simply absorb these dislocations and the required energy

penalty to transmit across the GB increases gradually. To model this behavior, the term $(1 + k_q \gamma_a^\alpha)$ is added in the formulation to account for the evolution of Q_{GB}^α . Here, γ_a^α is the accumulated slip on slip system α , given by

$$\gamma_a^\alpha = \int \dot{\gamma}^\alpha dt \quad (2.24)$$

and the coefficient k_q is taken as a constant here, which controls the rate of evolution of energy penalty with slip accumulation. The spatial distribution of accumulated slip for a bicrystal problem is presented in Section 3.7.1. The effect of evolution of penalty energy on the macroscopic response and its pattern of evolution for individual slip system is also discussed in Section 3.9 for the bicrystal problem. The method of calculating the misorientation based energy penalty Q_{0-GB}^α is discussed below.

Figure 2.3 shows the schematic of a typical slip transmission event across GB in a bicrystal. We are considering the transmission of dislocations from crystal I to crystal II separated by the GB having normal vector \underline{n}_{GB} . If a slip system of crystal I is described by the slip direction \underline{m}_0^α and slip plane normal \underline{n}_0^α then the task is to identify the slip systems $(\underline{m}_0^\beta, \underline{n}_0^\beta)$ in crystal II which offers the minimum energy barrier or the smallest misalignment to slip transmission. The dislocation line elements on the two sides of GB can be expressed as

$$\underline{l}^\alpha = b^\alpha (\underline{m}_0^\alpha \times \underline{n}_0^\alpha) \quad (2.25)$$

$$\underline{l}^\beta = b^\beta (\underline{m}_0^\beta \times \underline{n}_0^\beta) \quad (2.26)$$

where, b^α and b^β are the magnitudes of the respective Burgers vector. It is assumed that these dislocation line elements (\underline{l}^α and \underline{l}^β) will align with the GB plane during the transmission event. These aligned dislocation lines are obtained from

$$\underline{l}^{\alpha'} = \| \underline{l}^\alpha \| (\underline{n}_{GB} \times \underline{n}_0^\alpha) \quad (2.27)$$

$$\underline{l}^{\beta'} = \| \underline{l}^\beta \| (\underline{n}_{GB} \times \underline{n}_0^\beta) \quad (2.28)$$

For an arbitrary slip transmission event across GBs, it is possible that the incoming dislo-

cations do not have a corresponding geometrically coherent slip system on the other side of the GB. Therefore, the combined effect of the aligned dislocation line elements and the Burgers vector have been considered to obtain a second order tensor

$$\underline{b}_{GB}^{\alpha} \otimes \underline{l}_{GB}^{\alpha} = b^{\alpha} \underline{m}_0^{\alpha} \otimes \underline{l}^{\alpha'} - b^{\beta} \underline{m}_0^{\beta} \otimes \underline{l}^{\beta'} \quad (2.29)$$

quantifying the remnant lattice defects in the GB. The additional energy required to produce such extra misfit dislocations acts as an energy barrier measure for transmission events. The out-going slip system is the one that has the minimum energy barrier amongst all the possible slip systems of the surrounding grains. Thus, Q_{0-GB}^{α} is chosen as

$$Q_{0-GB}^{\alpha} = \min_{\beta} \frac{1}{2} G \|\underline{b}_{GB}^{\alpha}\|^2 \|\underline{l}_{GB}^{\alpha}\| \quad (2.30)$$

where $\|\underline{b}_{GB}^{\alpha}\|$ and $\|\underline{l}_{GB}^{\alpha}\|$ correspond to remnant Burgers vector and length of GB dislocations. The magnitude of the Burgers vector of these misfit dislocations can be expressed in terms of lattice Burger vector as

$$\|\underline{b}_{GB}^{\alpha}\| = c \|\underline{b}\| \quad (2.31)$$

where, $\|\underline{b}\|$ is the magnitude of lattice burger vector. The length of misfit dislocation line elements ($\underline{l}_{GB}^{\alpha}$) can be calculated using Equation (2.29) as

$$\|\underline{l}_{GB}^{\alpha}\| = \frac{\|\underline{b}^{\alpha} \otimes \underline{l}^{\alpha'} - \underline{b}^{\beta} \otimes \underline{l}^{\beta'}\|}{\|\underline{b}_{GB}^{\alpha}\|} \quad (2.32)$$

Therefore, the minimum energy penalty required for a typical penetration event across GB can be calculated as

$$Q_{0-GB}^{\alpha} = \min_{\beta} c \frac{1}{2} G \|\underline{b}\|^2 \frac{\|\underline{b}^{\alpha} \otimes \underline{l}^{\alpha'} - \underline{b}^{\beta} \otimes \underline{l}^{\beta'}\|}{\|\underline{b}\|} \quad (2.33)$$

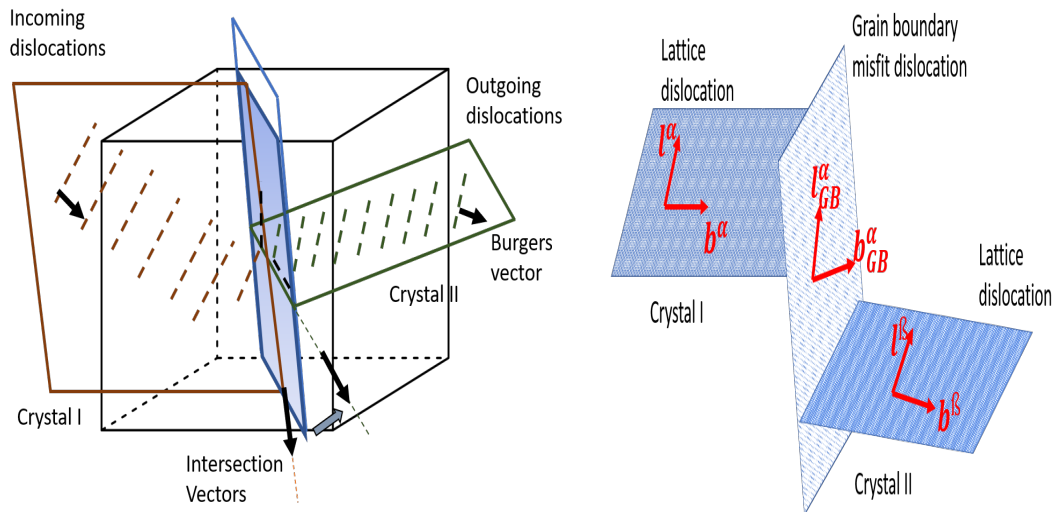


Figure 2.3: Schematic of slip transmission event across GB in a bicrystal.

The typical values of various modelling parameters used in the above formulations are presented in Table 2.2.

Table 2.2: Parameters of the non-local grain boundary model.

Symbol	Value	Meaning
γ_0	$1.732 \times 10^6 \text{ s}^{-1}$	Reference shear rate
p	0.141	Flow rule modelling parameter
q	1.1	Flow rule modelling parameter
E	$70 \times 10^9 \text{ Pa}$	Young's modulus
ν	0.3	Poisson's ratio
G	$25 \times 10^9 \text{ Pa}$	Shear modulus
g_0	$30 \times 10^6 \text{ Pa}$	Reference slip system resistance
h_0	$250 \times 10^6 \text{ Pa}$	Hardening coefficient
k_0	2	GND modelling parameter
$\hat{\alpha}$	10	GND modelling parameter
θ	298 K	Absolute temperature
b	$0.3 \times 10^{-9} \text{ m}$	Magnitude of burgers vector
k_B	$1.38 \times 10^{-23} \text{ JK}^{-1}$	Boltzmann's constant
Q_{slip}	$3 \times 10^{-19} \text{ J}$	Activation energy for slip
c	1	Coefficient of energy penalty
k_q	1×10^2	Coefficient of energy penalty evolution

2.4 Numerical Implementation

In typical finite element calculations using non-linear constitutive models, the discretized principle of virtual work (PVW), which enforces weak-form equilibrium and traction boundary conditions, generates an estimated incremental displacement field Δu . These fields drive the calculation of stress and other fields at the end of a time increment. If the calculated stress field does not satisfy the PVW, then the estimate of Δu is revised, and a new end-of-increment stress field is calculated. This iterative process continues until the PVW is satisfied to within acceptable tolerances.

Let us assume that at the beginning of a time increment step (say t_{n+1}) the following are given:

- (a) The time independent slip systems $(\underline{m}_0^\alpha, \underline{n}_0^\alpha)$.
- (b) Slip system resistances (g_n^α) , Cauchy stress $(\underline{\sigma}_n)$, the total strain tensor $(\underline{\epsilon}_n)$ and plastic strain tensor $(\underline{\epsilon}_n^p)$;
- (c) The total strain tensor $(\underline{\epsilon}_{n+1})$ for a suitably small (but finite) increment obtained from the estimated displacement field Δu

where n and $n + 1$ are points designating the beginning and end of a incremental displacement field given by Δu . The incremental problem is to calculate $\underline{\epsilon}_{n+1}^p$, g_{n+1}^α , $\underline{\sigma}_{n+1}$ and Δu at the end of time increment defined by $\Delta t = t_{n+1} - t_n$.

The time integration procedure employs a two level scheme. At the global level, suitable nodal Δu are evaluated iteratively such that the nodal force balance is ensured. In order to obtain the nodal forces in every element, stresses, plastic strain, etc. needs to be computed at every Gauss quadrature point in every element and is the local level. The evaluation of the quadrature point state is also determined from a two level scheme. In this approach, the stress is determined in the first level (inner loop) of the Newton-Raphson method while the slip system resistance is updated in the second level (outer loop). The iteration flag for the outer loop is chosen as (k) and for inner loop it is chosen as (m) . In the first level of iterative process, to achieve stress convergence the slip resistance (g_k) remains constant. Here, (g_k) denotes the updated value of slip resistance at k_{th} iteration of the outer loop. Since the total strain for the iteration $(\underline{\epsilon}_{n+1})$ is determined using

incremental displacement field, the total incremental strain can be calculated as

$$\Delta \underline{\underline{\epsilon}} = \underline{\underline{\epsilon}}_{n+1} - \underline{\underline{\epsilon}}_n \quad (2.34)$$

The Nye's dislocation tensor (given by Equation (2.16)) is also estimated here based on the plastic strain of the previous increment field ($\underline{\underline{\epsilon}}_n^p$), the method to calculate it is discussed in Section 2.4.1.

In the evaluation of stress, plastic strain, etc. at a Gauss quadrature, the outer loop is set to start with iteration flag $k = 1$. The initial guess for the Cauchy stress $\underline{\underline{\sigma}}_{(k=1,m=1)}$ is taken as the value of the previous time point, or, $\underline{\underline{\sigma}}_n$. Similarly, the initial guess for incremental plastic strain is taken as zero

$$\Delta \underline{\underline{\epsilon}}_{(k=1,m=1)}^p = 0. \quad (2.35)$$

The residual to obtain the Cauchy stress at any iteration is given by

$$\underline{r}_m = \underline{\underline{\sigma}}_m - \underline{\underline{\sigma}}_n - \left[\underline{\underline{\underline{\underline{C}}}} \left(\Delta \underline{\underline{\epsilon}} - \Delta \underline{\underline{\epsilon}}_m^p \right) \right] \quad (2.36)$$

where $\underline{\underline{\underline{\underline{C}}}}$ is the fourth order elasticity tensor. When this calculated residual (\underline{r}_m) comes within the defined tolerance,

$$\max \left(\left| \underline{r}_m \right| \right) \leq r_{tolerance} \quad (2.37)$$

the Cauchy stress is considered to be converged and we move to the outer level of iteration for updating the slip system resistances. However, if the estimated residual by Equation (2.36) does not satisfy the stress convergence condition, then we start the inner loop here (m=1), and calculate the Jacobian

$$A_{ijkl} = \delta_{ik}\delta_{jl} + C_{ijpq} * \frac{\partial}{\partial \tau_m^\alpha} \dot{\gamma}^\alpha(\tau_m^\alpha, g_k^\alpha) * \Delta t * S_{0pq} * S_{0kl} \quad (2.38)$$

In the above equation the resolved shear stress is calculated from

$$\tau_m^\alpha = \underline{\underline{\sigma}}_m : \underline{\underline{S}}_0^\alpha \quad (2.39)$$

and the slip rate $\dot{\gamma}_m^\alpha(\tau_m^\alpha, g_k^\alpha)$ is calculated using Equation (2.10). Subsequently the Cauchy stress is updated following

$$\underline{\underline{\sigma}}_{m+1} = \underline{\underline{\sigma}}_m - \underline{\underline{A}}_m^{-1} \underline{\underline{r}}_m \quad (2.40)$$

With the updated Cauchy stress, the resolved stress for the next iteration gets updated as

$$\tau_{m+1}^\alpha = \underline{\underline{\sigma}}_{m+1} : \underline{\underline{S}}_0^\alpha \quad (2.41)$$

the slip rate $\dot{\gamma}_{m+1}^\alpha(\tau_{m+1}^\alpha, g_k^\alpha)$ is calculated using Equation (2.10) and the incremental plastic strain is updated using

$$\Delta \underline{\epsilon}_{m+1}^p = \Delta \underline{\epsilon}_m^p + \sum_\alpha \dot{\gamma}^\alpha(\tau_{m+1}^\alpha, g_k^\alpha) \underline{\underline{S}}_0^\alpha \quad (2.42)$$

The above strategy is modified in the GB region according to Equation (2.20) as discussed in Section 2.3. Once the plastic strain is updated, a new residual is estimated from

$$\underline{\underline{r}}_{m+1} = \underline{\underline{\sigma}}_{m+1} - \underline{\underline{\sigma}}_n - \left[\underline{\underline{C}} \left(\Delta \underline{\epsilon} - \underline{\epsilon}_{m+1}^p \right) \right] \quad (2.43)$$

and checked for convergence condition defined by Equation (2.37). This iterative process in the inner loop is continued until the convergence condition is satisfied. The converged values of Cauchy stress, resolved shear stress, slip system resistances and slip rates for k_{th} iteration of outer loop are denoted as $\underline{\underline{\sigma}}_k$, τ_k^α , g_k^α , $\dot{\gamma}_k^\alpha$ respectively.

Once convergence is achieved in the inner loop, the slip systems resistances are updated in the outer loop using

$$\begin{aligned} g_{k+1}^\alpha &= g_k^\alpha + \sum_\beta h^{\alpha\beta} \left| \dot{\gamma}_k^\beta(\tau_k^\beta, g_k^\beta) \right| \\ &\quad + k_0 \frac{\hat{\alpha}^2 G^2 b}{2(g_k^\alpha - g_0^\alpha)} \sum_\beta \lambda^\beta \left| \dot{\gamma}_k^\beta(\tau_k^\beta, g_k^\beta) \right| \end{aligned} \quad (2.44)$$

and the following

$$|g_{k+1}^\alpha - g_k^\alpha| \leq g_{tolerance} \quad (2.45)$$

is checked. If the above criterion is not satisfied then we repeat the process in the inner loop with the updated slip system resistance value (g_{k+1}^α) .

The converged values of Cauchy stress and slip system resistances depict the state of the Gauss quadrature point at t_{n+1} . The Cauchy stress is used to calculate the elemental CPFEM residual. The assembly of all the elemental residuals yields the global residual which represents the incremental principle of virtual work (PVW). It is checked whether the norm of the global residual is within the acceptable tolerance. If *not* then the incremental displacement field (Δu) is updated and the two level iterative process is repeated. This iterative process continues until the PVW is satisfied.

2.4.1 Calculation of Nye's Dislocation Tensor

As discussed in the previous Section, for every incremental displacement field applied for the convergence of state variables during numerical time integration, the slip system resistance is required to be updated. As we have seen in Equation (2.12), the total slip resistance has two components. The second term, which represents the contribution of GNDs to the total slip system resistance, is calculated based on the Nye's dislocation tensor ($\underline{\underline{\Lambda}}$). For our approach using additive decomposition of strain rates, the Nye's tensor is defined as the *curl* of the plastic strain tensor ($\underline{\underline{\epsilon}}^P$) (Equation (2.16)). In the previous Section we have seen that after every iteration of displacement update (Δu), the converged plastic strain tensor is obtained at each integration points or Gauss quadrature points. The schematic of an iso-parametric four noded rectangular element with four Gauss points used in this work is shown in Figure 2.4, where red squares represent position of the nodes while blue dots are the positions of Gauss points.

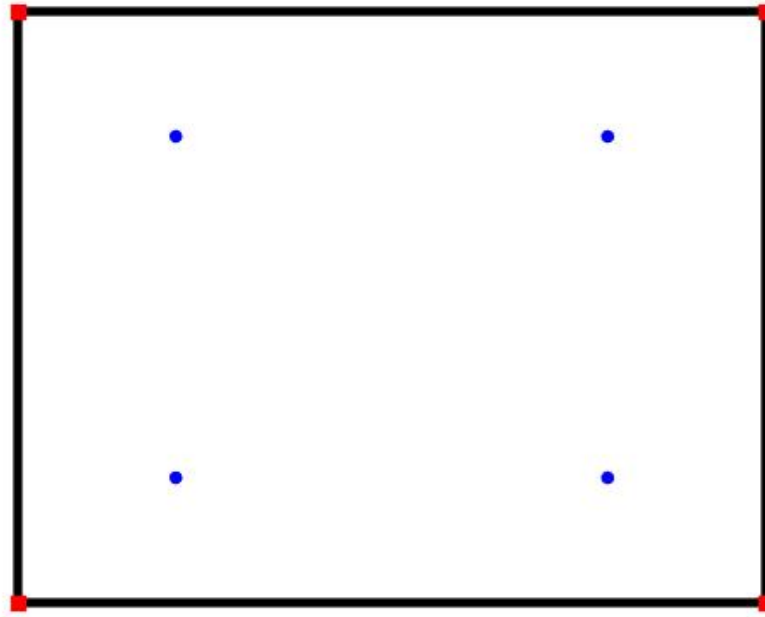


Figure 2.4: Schematic of four noded element with four Gauss points.

The Nye dislocation tensor ($\underline{\underline{\Lambda}}$) can be expressed as

$$\underline{\underline{\Lambda}} = \nabla^T \times \underline{\underline{\epsilon}}^p = \epsilon_{ijk} \frac{\partial \epsilon_{mj}^p}{\partial x_i} \underline{e}_k \otimes \underline{e}_m \quad (2.46)$$

where ϵ is the Levi-Civita symbol, \underline{e}_k and \underline{e}_m are the basis vectors of the three dimensional space. The above expression is simplified for the case of plane strain deformation as

$$\underline{\underline{\Lambda}} = \begin{bmatrix} 0 & 0 & (\epsilon_{231} \epsilon_{33,2}^p) \\ 0 & 0 & (\epsilon_{132} \epsilon_{33,1}^p) \\ (\epsilon_{213} \epsilon_{11,2}^p + \epsilon_{123} \epsilon_{12,1}^p) & (\epsilon_{213} \epsilon_{21,2}^p + \epsilon_{123} \epsilon_{22,1}^p) & 0 \end{bmatrix} \quad (2.47)$$

For calculating the various spatial derivatives involved in Equation (2.46) at a Gauss point, the plastic strain values at the Gauss points are required to be extrapolated to the nodes. Once we have the values at the nodes we can interpolate them again in terms of elemental shape functions. We know that the value of any variable at a Gauss point inside the 2D

rectangular element can be related to the nodal values using

$$y_{gauss} = \sum_i N_i y_{i_{node}} \quad (2.48)$$

If we apply the same for the plastic strain components then a relation can be established between their values at the Gauss points and nodes. This relation is a simple linear map expressible as a matrix-vector operation following

$$\{\epsilon^p\}_{gauss} = [N] \{\epsilon^p\}_{node} \quad (2.49)$$

where N is the matrix of shape functions evaluated at the Gauss points. As the map is unique and the matrix is invertible hence the nodal values of plastic strain components is found from

$$\{\epsilon^p\}_{node} = [N]^{-1} \{\epsilon^p\}_{gauss} \quad (2.50)$$

For the nodes which are getting shared the total extrapolated values at these node are averaged to get the value at the node. Once we have the values at the nodes the Equation (2.47) is applied to obtain the Nye's tensor at the Gauss points. The entire algorithm described above is aimed at expressing the Gauss point values of the curl of a tensor within an element using the shape functions defined in natural coordinates.

CHAPTER 3

Numerical Study Using a Two-Grain Representative Volume

3.1 Problem Description

The schematic illustration of uniaxial plane strain tensile deformation of a bicrystal domain is shown in Figure 3.1. The geometry, boundary conditions and FEM mesh are displayed in this figure. The dotted and solid black lines represent the mesh and the outer surfaces of the domain respectively. ‘ $L_1 = 2D + W_{GB}$ ’ and ‘ $L_2 = D$ ’ are the dimensions of the shown bicrystal domain, where ‘D’ represents the grain width and W_{GB} is the width of GB region. The solid red lines symmetrically spaced in the middle of the domain separate the grain boundary region from the grain interior regions. The point of lower left corner is hinged while roller supports are provided along the lower edge of domain. The left and right edges of domain are free while displacement is applied on the top edge.

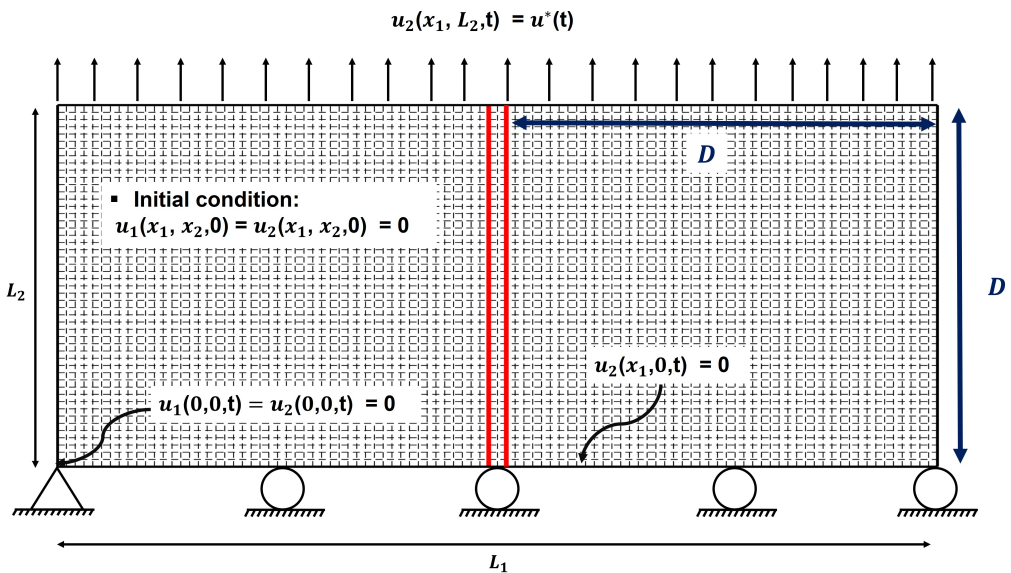


Figure 3.1: Schematic of a bicrystal in plane strain condition and subjected to uniaxial loading.

3.2 Reduced Slip Systems of FCC Single Crystal in Plane Strain

Generally, the three-dimensional CPFEM computations are required to capture realistic deformation behaviour of crystals. However, three-dimensional simulations are computationally expensive and also may not always help to get an insight into the fundamental understanding of the physical phenomenon. In contrast, the two-dimensional computations under plane strain conditions are more efficient and can provide effective information on the fundamental deformation behavior of such materials. Thus, in this work plane strain two dimensional analyses have been performed.

The FCC slip systems if simulated in 2D on any plane can result in out-of-plane shear components of plastic strain and stress. However, a suitable plane (or a family) can be chosen for 2D analysis involving FCC crystals that can eliminate out-of-plane shear components. This will primarily happen due to the symmetric and anti-symmetric response of certain slip systems when the FCC crystal is loaded on this plane. Considering this slip behavior on the chosen plane (or family) the total number of slip systems of the FCC crystal can be reduced. These planer pseudo slip systems are the contractions of the actual crystallographic slip systems with a particular crystal orientation that the out-of-plane shear component of plastic strain cancels out. Such simplified versions have been often employed in the past to study the crystal deformation behaviour [35; 36; 37; 38]. Crack problems were investigated under plane strain conditions in [39; 40]. In experimental studies [41; 42], plane strain specimens were employed to explore the fundamental nature of GND storage in a macroscopic strain gradient field and hence this representation can be useful.

The slipping of dislocations is naturally preferred on some specific planes (close packed planes) and in specific directions (close packed directions). In FCC crystal structures, there are 4 octahedral planes (111) , $(\bar{1}11)$, $(1\bar{1}1)$ and $(11\bar{1})$, and 3 $\langle 110 \rangle$ directions on each plane, resulting in a total of 12 slip systems. In the present work, the twelve slip systems of face-centered cubic (FCC) crystal is reduced to a two-dimensional plane strain version having eight effective slip systems. These Slip system are schematically

illustrated in Figure 3.2. In the figure, the yellow colored plane represents the plane of loading, M_1 to M_8 are the modified slip directions, and N_1 and N_4 are the slip plane normals. From this figure we can see that the three slip directions of any octahedral plane of FCC crystal can be resolved into two slip directions. The arrangement of slip directions are such that the plastic strain rate obtained from Equation (2.7), and stress has zero out of plane shear components. Table 3.1 presents the slip directions and planes for these slip systems where, $V_1 = \sqrt{2/3}$, $V_2 = \sqrt{1/3}$.

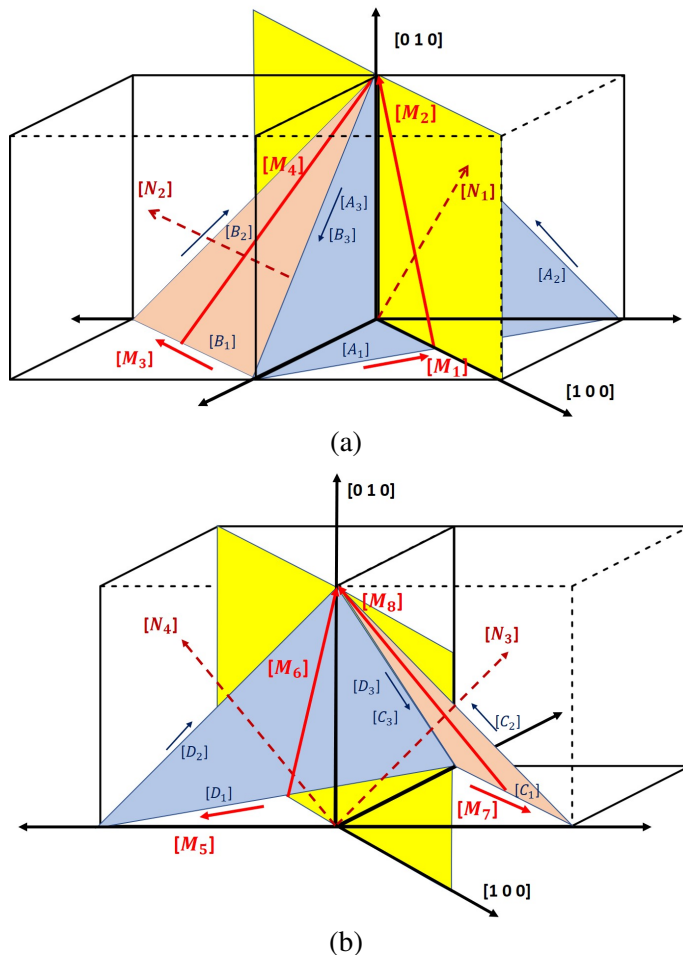


Figure 3.2: Reduced slip systems for FCC crystal for 2D plane strain CPFEM simulations. Plane of loading is highlighted in yellow. N_1 to N_4 are the slip plane normals. M_1 to M_8 are the modified slip directions. A_1 to A_3 , B_1 to B_3 , C_1 to C_3 and D_1 to D_3 are the original slip directions on the octahedral planes.

Table 3.1: Reduced slip systems of FCC crystal for 2D plane strain CPFEM simulations.

No.	Slip Plane Normal	Slip Direction	Label
1	($V_1 \ V_2 \ 0$)	[0 0 1]	M1
2	($V_1 \ V_2 \ 0$)	[$\bar{V}_2 \ V_1 \ 0$]	M2
3	(0 $V_2 \ V_1$)	[1 0 0]	M3
4	(0 $V_2 \ V_1$)	[0 $V_1 \ \bar{V}_2$]	M4
5	($\bar{V}_1 \ V_2 \ 0$)	[0 0 1]	M5
6	($\bar{V}_1 \ V_2 \ 0$)	[$V_2 \ V_1 \ 0$]	M6
7	(0 $V_2 \ \bar{V}_1$)	[1 0 0]	M7
8	(0 $V_2 \ \bar{V}_1$)	[0 $V_1 \ V_2$]	M8

3.3 Convergence Study

The aim of the formulation using the diffused representation of GB region is to model the Hall-Petch behavior by penalising the transmission of dislocations across the GBs, which in turn can lead to develop a gradient of plastic deformation and increase the resistance offered to slipping of dislocations. However, the physical thickness of the GB region should not directly affect the macroscopic responses by virtue of its size which is very small compared to the grain dimensions in actual microstructure of the metallic alloys . Moreover, the macroscopic elasto-plastic responses should not be affected by the element size of FEM mesh and the time step used in implicit-explicit numerical integration scheme discussed in Chapter 2. To ensure these conditions, convergence studies are performed to determine the optimal physical thickness of the GB region, element size of FEM mesh and the time step size before performing bicrystal and polycrystal CPFEM simulations to explore Hall-Petch effect. These convergence studies are presented next.

3.3.1 Optimal Physical Thickness of GB Region

For determining the optimal physical thickness of GB region a bicrystal problem confirming with the one described in Section 3.1 is chosen. The grain width (D) is kept to be constant as $D = 50\mu m$. The thickness of the GB region is varied as 0%, 1%, 2%, 4% and 6% of D which comes to be $0\mu m$, $0.5\mu m$, $1\mu m$, $2\mu m$ and $3\mu m$ respectively. Here the 0% case is the one where no actual interface region is present, but the gradients induced by the misorientation between neighbouring grains is captured by GND. The time step and size of finite element mesh is kept constant for running these simulations. The chosen time step is 0.001 *second* and the domain is discretized into elements of $0.5\mu m \times 0.5\mu m$ dimension which are also later on verified to be converged in Section section 3.3.2 and Section 3.3.3 respectively. The true macroscopic stress is plotted against applied tensile strain in Figure 3.3 to understand the effect of physical thickness of the GB region on elasto-plastic response. The figure shows that the macroscopic elasto-plastic responses are almost converged for the cases when the physical thickness of the GB region is dropped to less than or equal to 2% of the grain diameter (D).

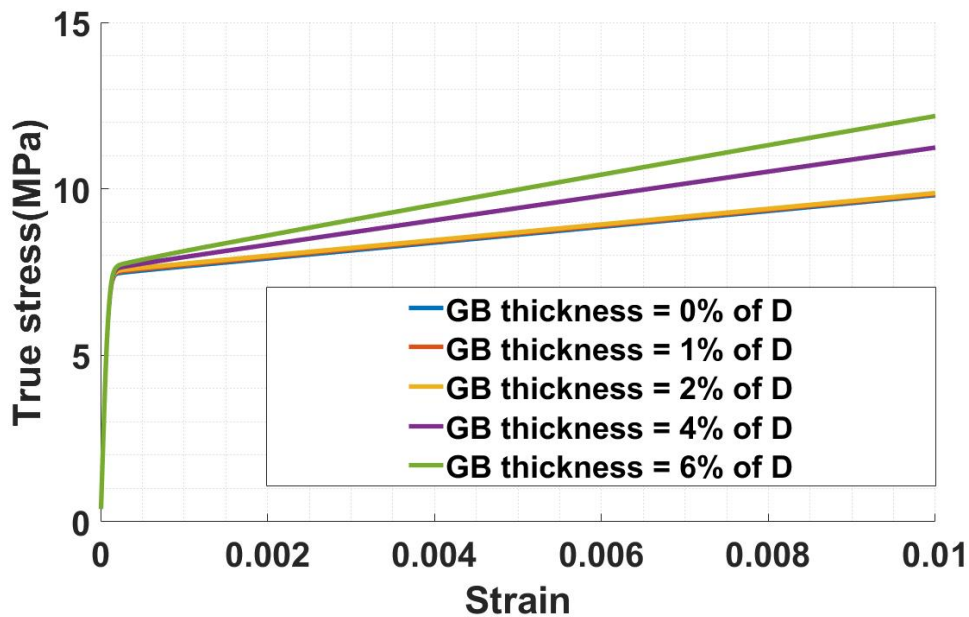


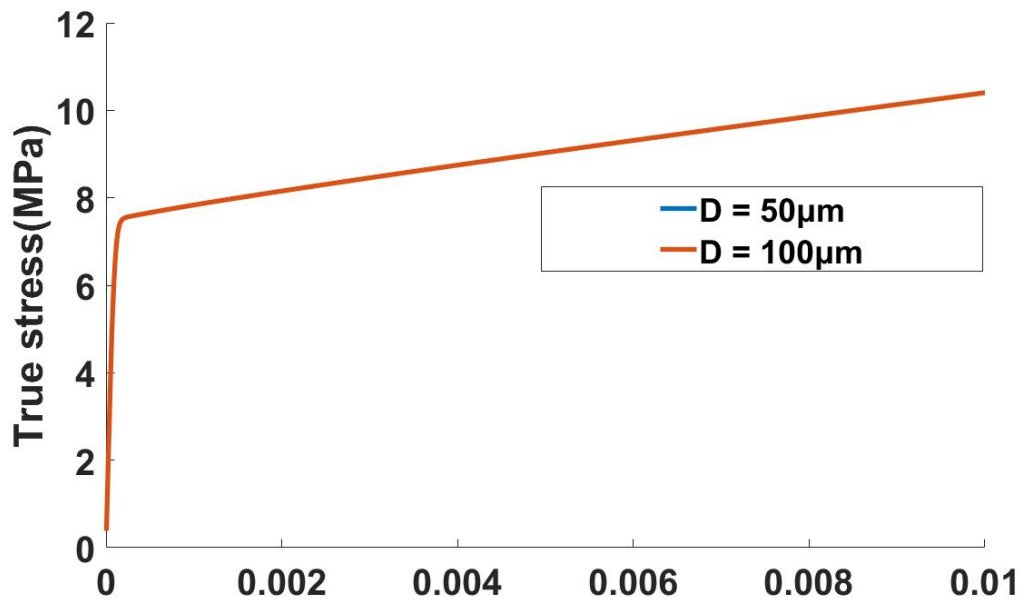
Figure 3.3: Effect of physical thickness of the GB region on macroscopic stress-strain response. D represents the grain diameter.

In continuation with the above conclusion, it is further required to prove that the con-

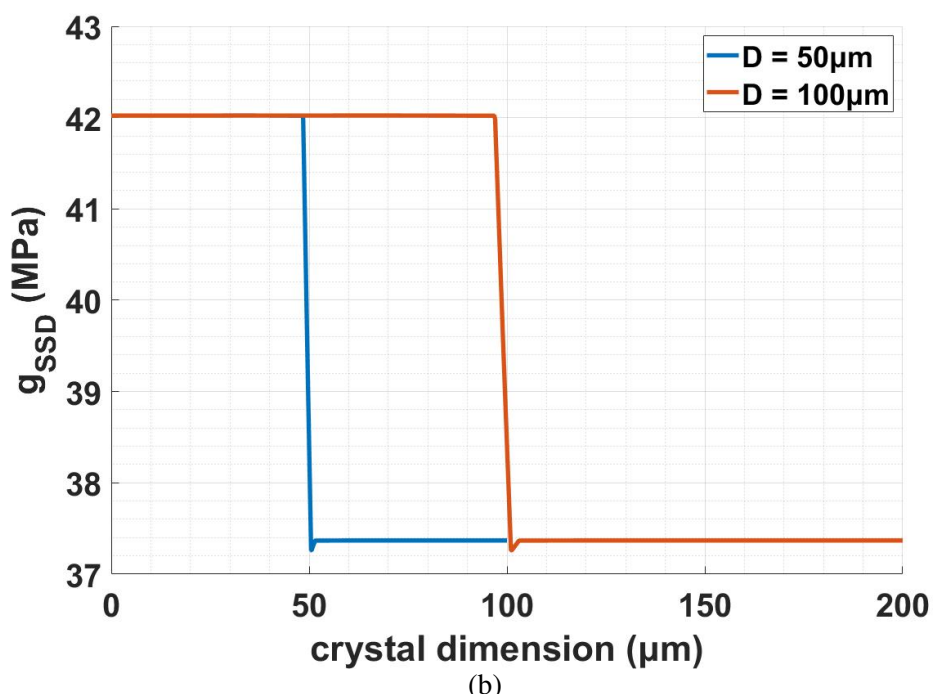
vergence with interface thickness can be given in terms of a normalized quantity such as the ratio of thickness to grain diameter and not the absolute thickness value, i.e., the responses are converged with the GB region having thickness as 2% of grain diameter or lower and not the absolute value $1\mu m$ which is the same for the above defined set of case studies. To verify this, similar plane strain tensile deformation problem was chosen, but with two different grain sizes (Figure 3.1) of $L_1 = 100\mu m$ and $L_1 = 200\mu m$. In both the cases thickness of GB region (W_{GB}) is taken as 2% of D , i.e. in first case it is $1\mu m$ while for later one it is $2\mu m$. The GNDs are turned off for these cases so that the macroscopic stress-strain responses are not affected because of the grain size effect captured by GNDs.

The comparisons of macroscopic and local results are shown in the figures below. In Figure 3.4 (a) we can see that the macroscopic responses remain unaffected for the two cases with different grain size and therefore with two different absolute physical thickness of GB region. From this we can conclude that the GB region thickness convergence is obtained for 2% percent of grain diameter for which the absolute thickness value can vary with the chosen grain diameter. The response can be explained using Figure 3.4 where we can clearly see that the slip system resistance caused by SSDs remains almost unaffected for chosen thickness of GB region.

From the results of previous two sets of case studies it can be educed that if the thickness of the GB region is chosen to be less than or equal to 2% of the grain diameter then the GB region does not directly affect the local as well as the macroscopic responses due to the use of a different constitutive model. Rather the GB region bring in the desired grain size effect by affecting transmission of dislocations across it.



(a)



(b)

Figure 3.4: GB thickness convergence with two different grain size without considering the effect of GND. (a) macroscopic stress vs strain and (b) maximum of all the slip system resistances due to SSDs.

3.3.2 Converged Time Step Size

An implicit-explicit time integration scheme is adopted in this work as discussed in Section 2.4. The explicit method to calculate Nye's tensor can introduce error in the solution if a large time step size is used and a suitable size should be chosen to get accurate results along with minimum computational overhead. The typical time step size used for simulating the case studies presented in this thesis varies from $dt = 0.001 \text{ second}$ to $dt = 0.0005 \text{ second}$ depending upon the size of the problem. The convergence study is performed with an even smaller time step $dt = 0.0001 \text{ second}$ to show that the responses are converged in the range of time step size used for the simulations in this thesis. The bicrystal problem with $L_1 = 100\mu\text{m}$ and GB region thickness as $1\mu\text{m}$, described in Section 3.1, is chosen to obtain the converged time step. The domain is discretized into elements of size $0.5\mu\text{m} \times 0.5\mu\text{m}$, and is kept the same for all three cases of different time step size. The macroscopic stress strain curves for the chosen time step sizes are shown in Figure 3.5. As can be seen from the figure, the macroscopic responses are almost overlapping for all the three cases and hence $dt = 0.001 \text{ second}$ can be considered as a suitable time step size to obtain accurate results.

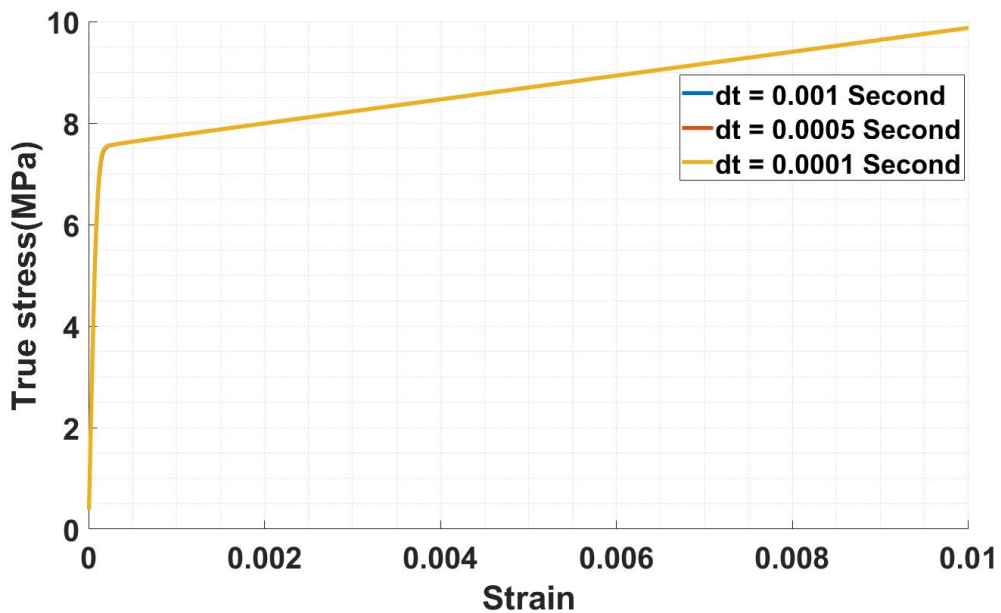


Figure 3.5: Macroscopic stress-strain response for three different sizes of time step.

3.3.3 Mesh Sensitivity Analysis

Discretizing the domains into certain number of finite elements is a method of finding numerical solutions for several real life problems. However, theoretically the domains should be discretized into infinite number of small elements to find accurate solutions, but it will make it computationally infeasible. Therefore, finite element meshes with the mesh sizes for which the responses appears to be converged with an error in the range of defined acceptable tolerance are chosen for numerical simulations. Executing the GB models with having uniform mesh usually become computationally heavy for the converged time step size and converged physical thickness of GB region as discussed in Section 3.3.1. The challenge is even more for simulating actual polycrystal problems as the required number of elements are significantly large depending on the number of grains and may require even smaller time steps for convergence of Newton Raphson iterations.

The purpose of doing a mesh sensitivity analysis is to find the largest possible element size for which the responses are converged with error lying in the range of accepted tolerance. In this work an upper limit for possible element size is set by the converged optimal thickness of GB region defined in Section 3.3.1, $W_{GB} = 1\mu m$ in this case where the GB discretized using one element. In the mesh sensitivity analysis the bicrystal problem described in Section 3.1 is used with $L_1 = 100\mu m$, $W_{GB} = 1\mu m$ and $dt = 0.0005$ second. Three different element sizes of $1\mu m \times 1\mu m$, $0.33\mu m \times 0.33\mu m$ and $0.25\mu m \times 0.25\mu m$ are taken.

Figure 3.6 shows that the macroscopic responses are almost converged for the mesh sizes $0.33\mu m \times 0.33\mu m$ and $0.25\mu m \times 0.25\mu m$, while for element size $1\mu m \times 1\mu m$ we can see the small deviation from the converged response near 1% strain. Though the divergence of responses is very small, the computational time involved gets significantly increased for the smaller element size mesh. Hence, we are considering the mesh size of $1\mu m \times 1\mu m$ in subsequent simulations.

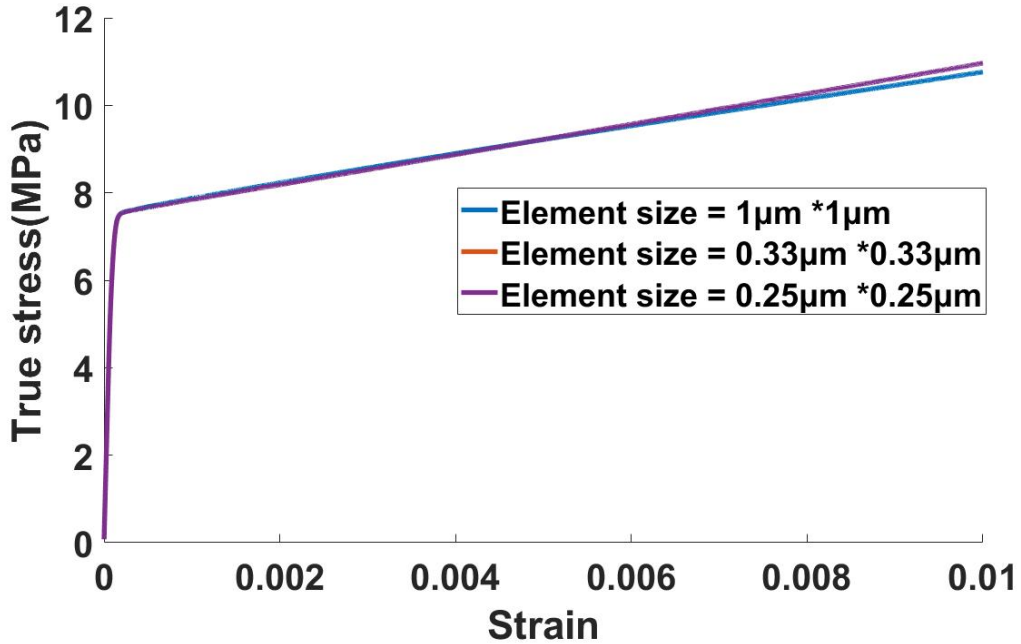


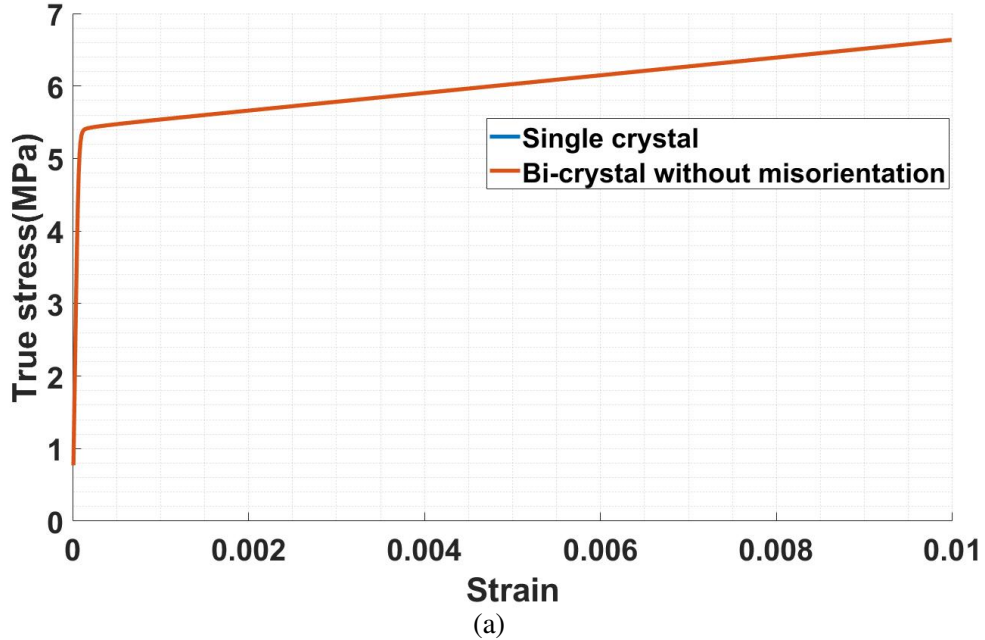
Figure 3.6: Macroscopic stress-strain response for three different element sizes of finite element mesh.

3.4 Verification of Single Crystal Effect

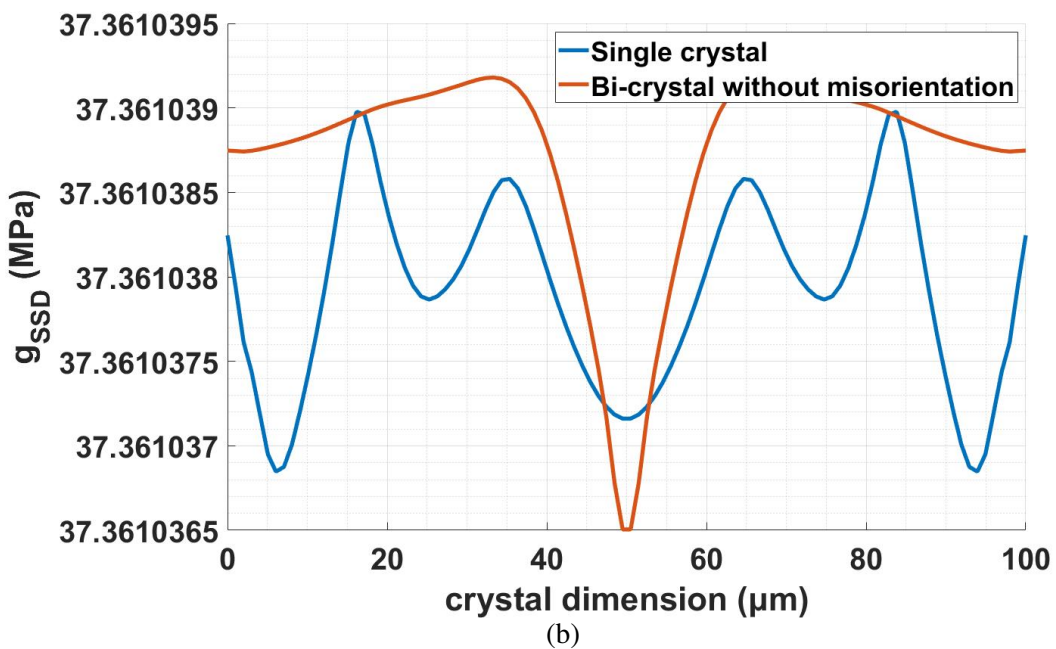
Here we consider a bicrystal in which both the crystal have the same orientation. Since both the grains have the same orientation then slip transmission across the GB should not encounter any resistance and the bicrystal response as obtained from the model should be same as that of the single crystal. In this comparison the response of a single crystal with no GB region is compared with a bicrystal having the same orientation when subjected to uniaxial tensile strain of 1% as described in Section 3.1. For both the single crystal and bicrystal geometries, $L_1 = 100\mu m$, and $L_2 = 50\mu m$. Additionally for the bicrystal $D = 49.5\mu m$ and $W_{GB} = 1\mu m$ which also produces $L_1 = 100\mu m$.

A comparison of the macroscopic and local responses of the bicrystal and single crystal under uniaxial strain is shown in the figures below. In Figure 3.7 we can see that (a) the macroscopic response are exactly the same for the two cases. The local response is obtained on a material line from $(0, L_2/2)$ to $(L_1, L_2/2)$ (see Figure 3.1). The comparisons are shown in Figure 3.7(b) to (f). As it can be seen from the figures, the variations

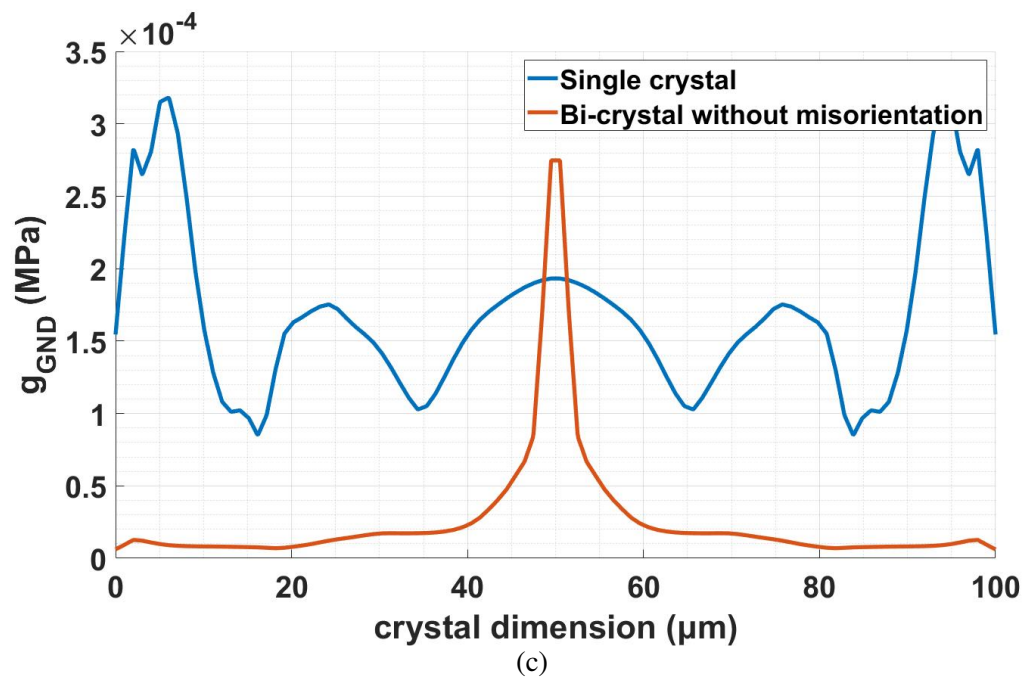
in g_{SSD} , g_{GND} , g_{total} , σ_{22} and ϵ_{22} are also within the tolerance limits. Another important inference we can develop is that for the cases of very small misorientation, the slip system resistance caused by GNDs is negligibly small compared to total slip system resistance caused due to SSDs.



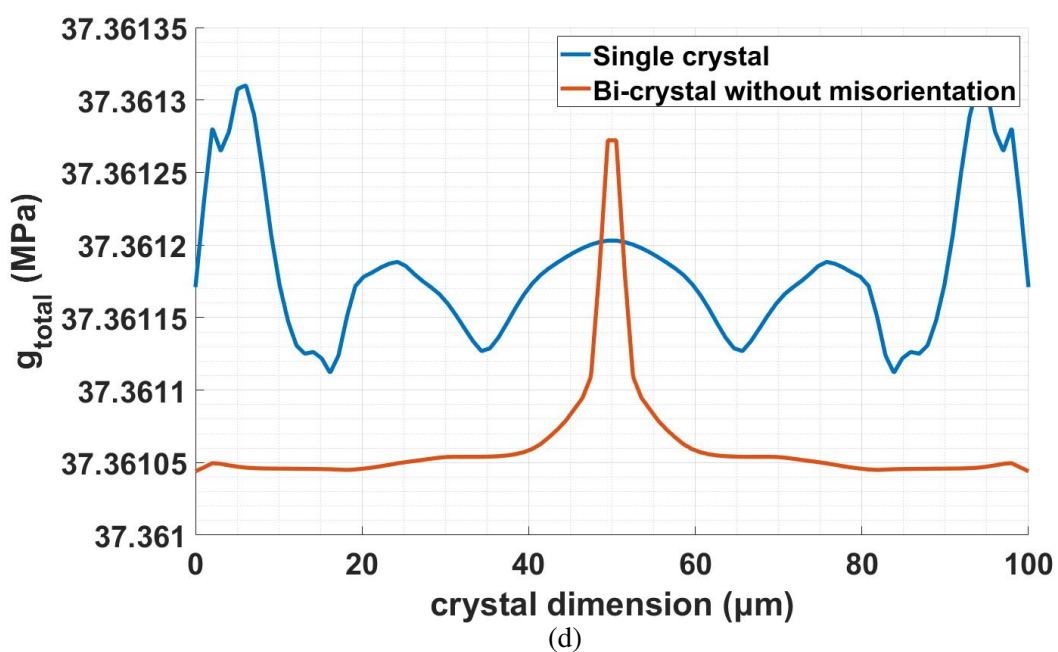
(a)



(b)



(c)



(d)

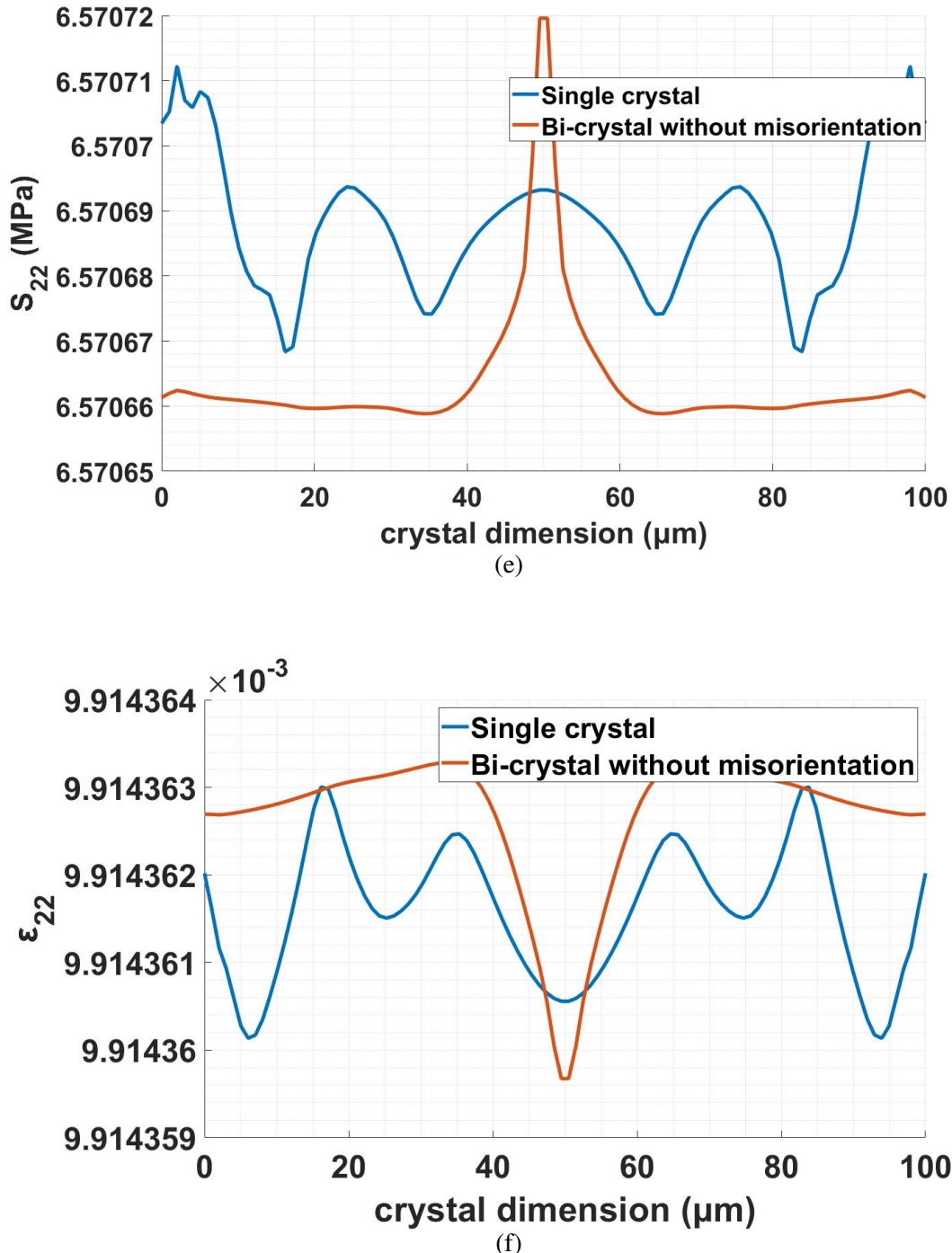


Figure 3.7: (a) Comparison of macroscopic stress vs strain between bicrystal with zero misorientation and single crystal. Comparison of (b) maximum of all slip system resistances caused by GNDs, (c) maximum of all slip system resistances caused by SSDs, (d) maximum of all total slip system resistances, (e) normal stress component in the loading direction, and (f) normal strain component in the loading direction, between bicrystal with zero misorientation and single crystal on a line $(0, L_2/2)$ to $(L_1, L_2/2)$ at applied uniaxial strain of 1%.

3.5 Independence of GB Resistance to Relative Orientation of Grains

The slip transmission across an interface should depend on the misorientation $\theta_1 - \theta_2$ and not on the relative location of the grains with orientation θ_1 and θ_2 . Therefore, if we simply interchange the orientations of the grains on the two sides of the GB region, neither the macroscopic nor the local responses of the two individual grains should be affected. For checking this we take two similar bicrystals both having grain size (D) = $49.5\mu m$ and a GB region thickness (W_{GB}) = $1\mu m$. The macroscopic boundary condition and deformation scheme remains the same for both of them as represented in Figure 3.1. For the two crystals two different Euler angles are chosen as 45° and 0° . In one of the cases the 45° grain is on the left and 0° grain is on the right side of GB region while in the other case 45° grain is kept on the right and 0° grain is on the left side of GB region as shown in Figure 3.8.

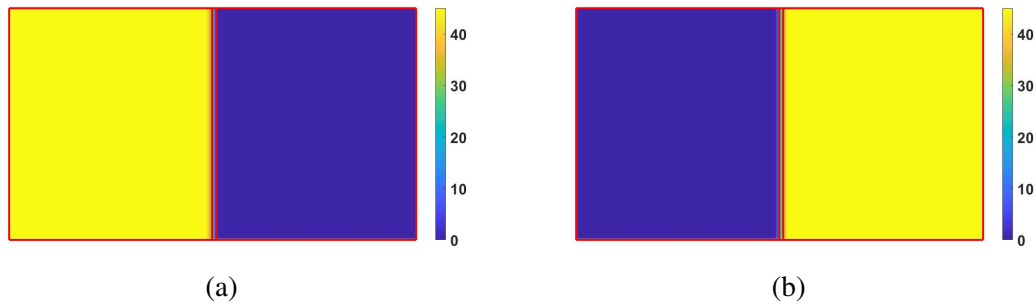
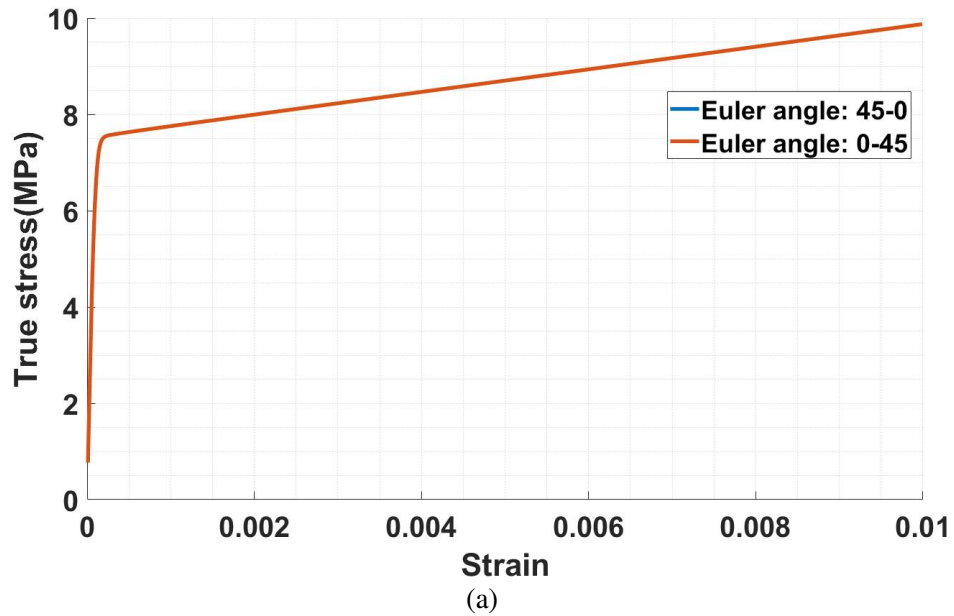
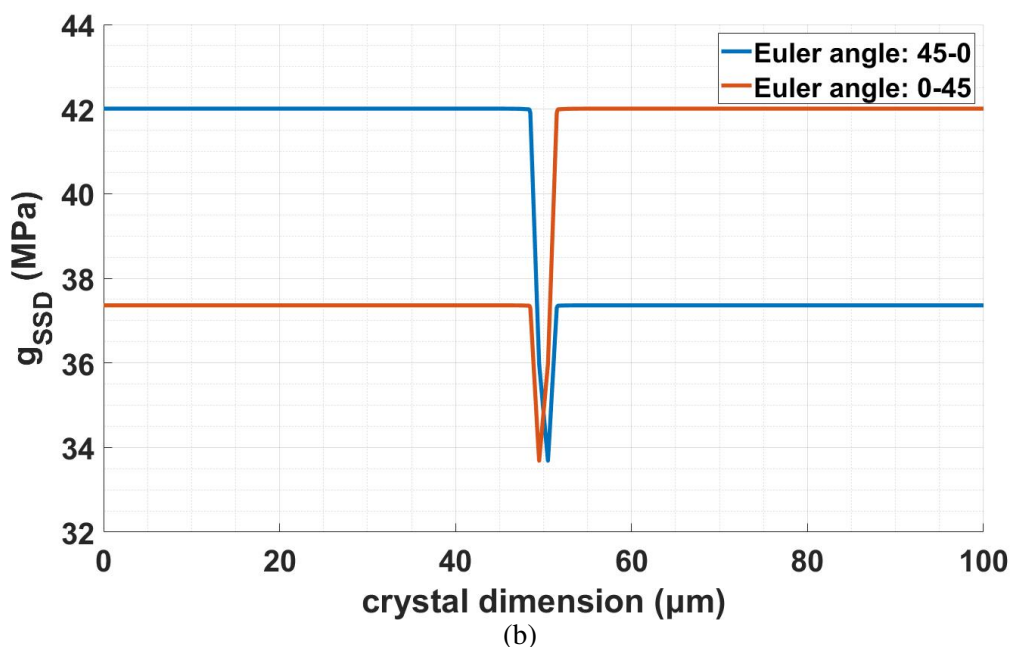


Figure 3.8: Two bicrystals with the following grain orientations: (a) Euler angle of left grain = 45° and right grain = 0° ; (b) Euler angle of left grain = 0° and right grain = 45° .

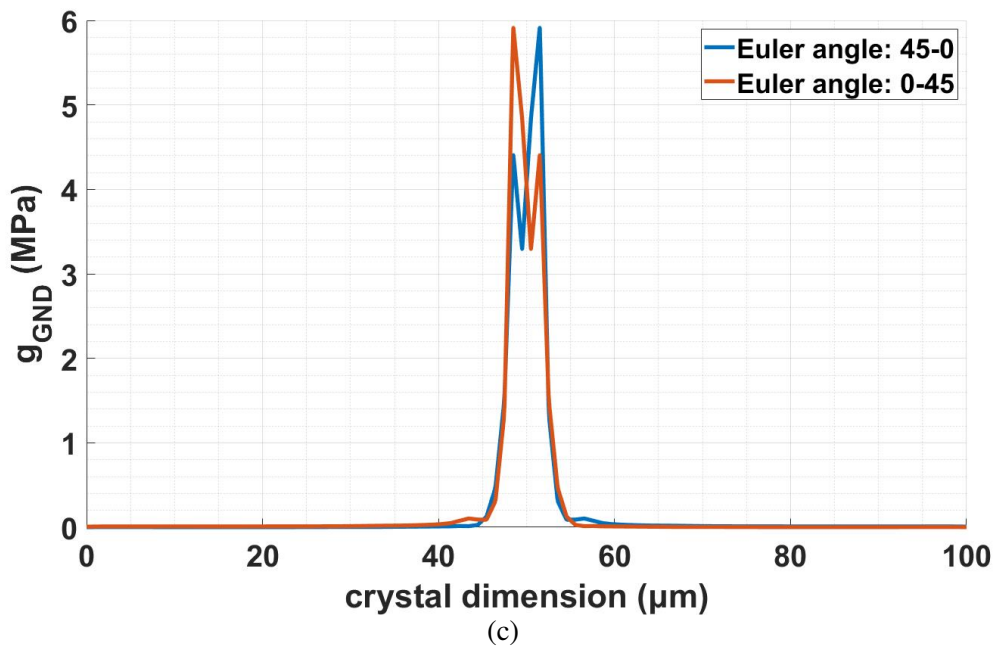
A comparison of the macroscopic and local responses of the bicrystals under uniaxial strain is shown in the figures below. From Figure 3.9 (a) we can see that the macroscopic response of both bicrystals are identical. The comparison of the other variables such as stress, strain, slip system resistances, etc. on the line $(0, L_2/2)$ to $(L_1, L_2/2)$ in Figures 3.9 (b) to (f) shows that they are mirrored, which clearly demonstrates that the GB region model is able to capture the invariance on relative orientation.



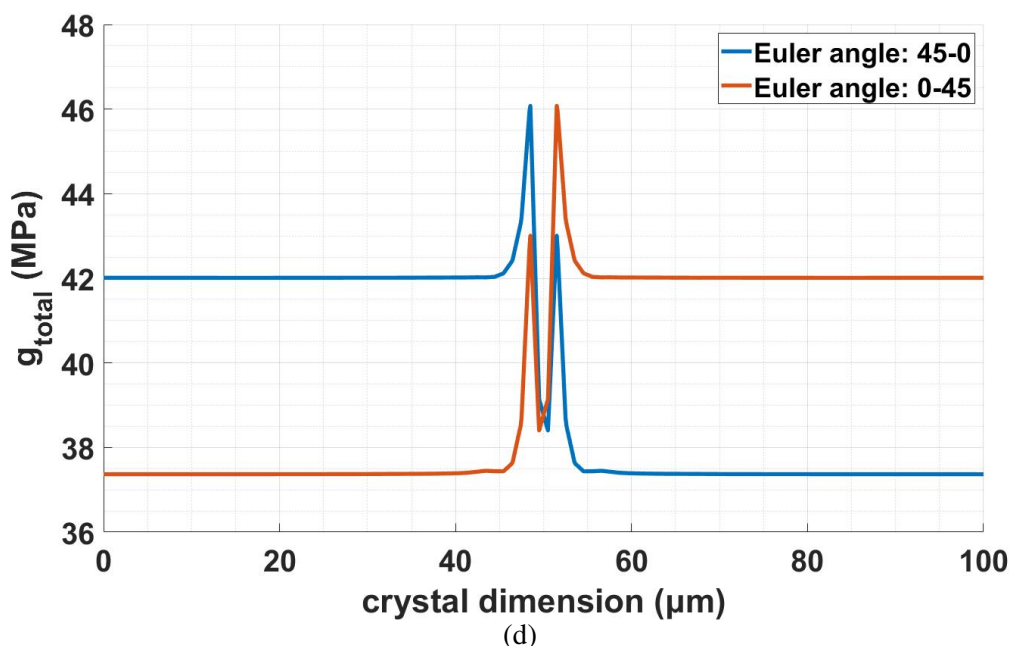
Strain
(a)



crystal dimension (μm)
(b)



(c)



(d)

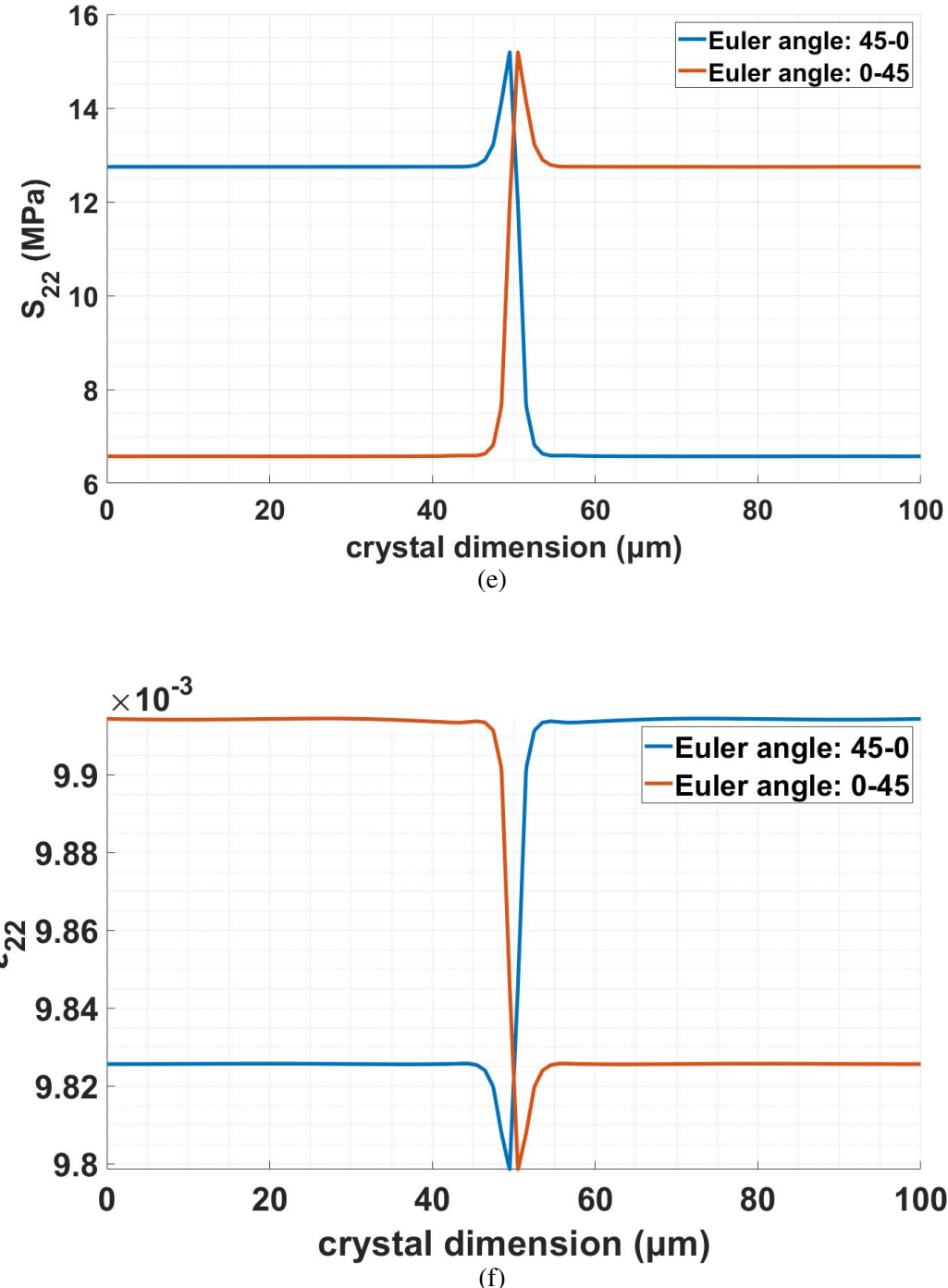


Figure 3.9: (a) Comparison of macroscopic stress vs strain between the bicrystals with different orientations. Comparison of (b) maximum of all slip system resistances caused by GNDs, (c) maximum of all slip system resistances caused by SSDs, (d) maximum of all total slip system resistances, (e) normal stress component in the loading direction, and (f) normal strain component in the loading direction, between the bicrystals with different orientations on a line $(0, L_2/2)$ to $(L_1, L_2/2)$ at applied uniaxial strain of 1%.

3.6 Initialization of Size Dependent GND Density in a Microstructure

As discussed in Chapter 1, for most of the GND based models developed to capture the effect of grain size on the elasto-plastic behaviour, the responses in the first yield appears to be independent of grain size and the size effect is observed only later in the hardening region. The reason behind such response is that, these models capture the effect of grain size on yield stress by capturing the developed gradient of the plastic strain. Thereafter, the size effect is brought in by relating this gradient of plastic strain to the slip system resistance using various GND density formulations. Depending upon their geometrical nature as discussed above, GNDs evolve in the plastic deformation region, while the responses in the near elastic region is controlled by SSDs which are independent of grain size. To make these models capable of capturing size effect, some size dependent initial GND density must be introduced. W.A.Counts et al. [27] have introduced an initial fictitious kinematics in their model to define initial state of microstructure.

To incorporate the above discussed effect in the model developed in this work, we employ an unloading-reloading technique. In this method, the crystal is first deformed in the displacement controlled mode up to a strain level in the plastic deformation region and then allowed to relax in the load controlled mode by removing the applied deforming conditions until the tractions on all the free surfaces of the specimen are zero. This relaxed state is then considered as the initial state to perform uniaxial tensile simulation.

The unloading is done in load controlled mode to avoid developing reactive tractions of opposite nature. The unloaded and reloaded states for a plastically deformed bicrystal is shown in Figure 3.10(a). In this figure, We can see that the reactive tractions are zero in unloaded state. However, it can also be seen that the unloading path does not trace back the initial loading path. There is a slight increase in strain during the load controlled unloading process and is caused by the stresses developed at the end of the strain controlled loading step.

To verify the implementation and technique, the same procedure is applied on an elastic specimen Figure 3.10(b). Here it can be seen that the loading, unloading and reloading

paths trace each other as expected. For the elasto-plastic bicrystal, the distribution of maximum slip system resistance due to GND (g_{GND}) amongst all the slip systems after unloading is shown in Figure 3.11. As can be seen from the figure, there is a heterogeneous distribution of g_{GND} that shows the workability of this approach.

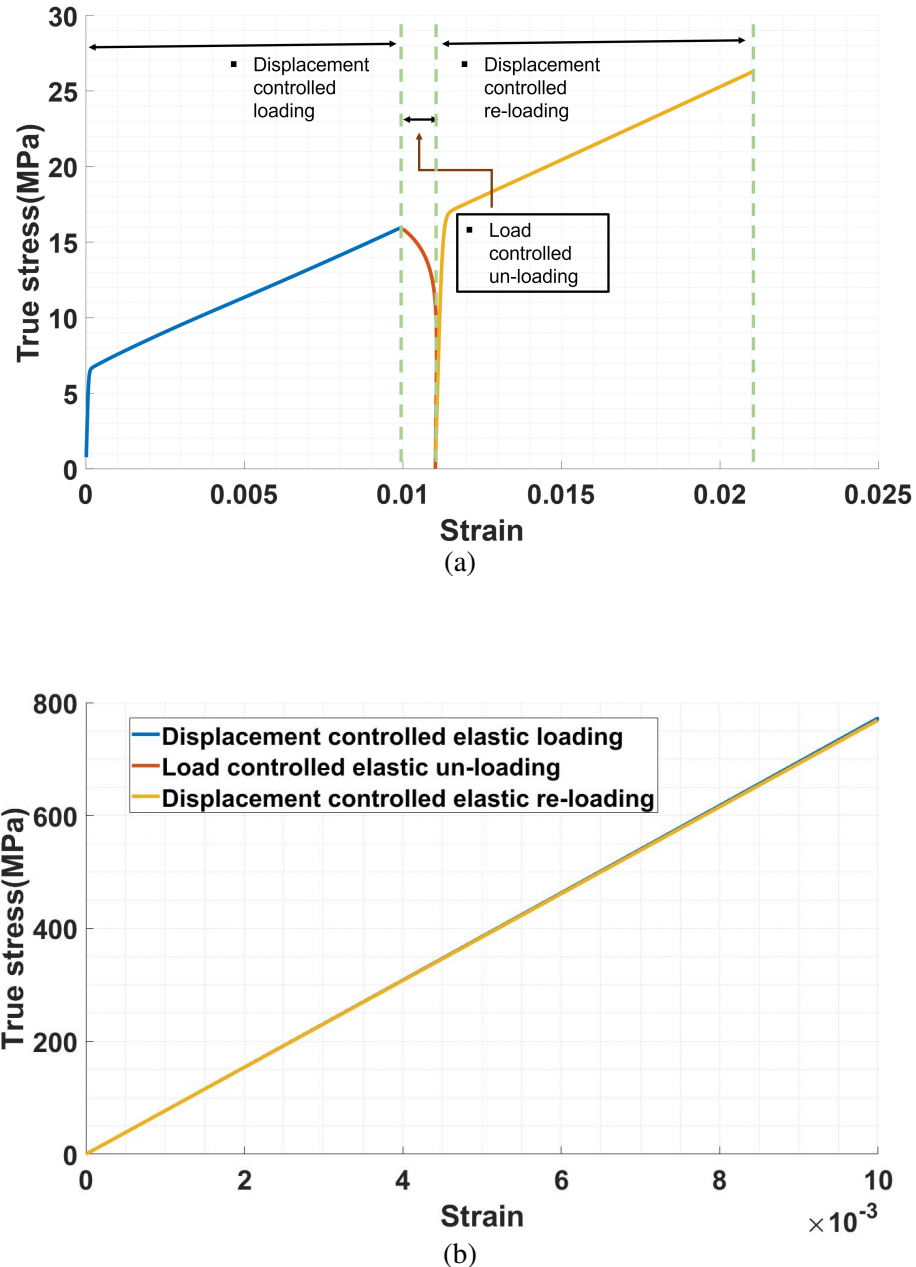


Figure 3.10: Macroscopic stress-strain response for unloading-reloading technique applied to (a) elasto-plastically deformed specimen, and (b) elastically deformed specimen, for initializing the size dependent GND density in a microstructure.

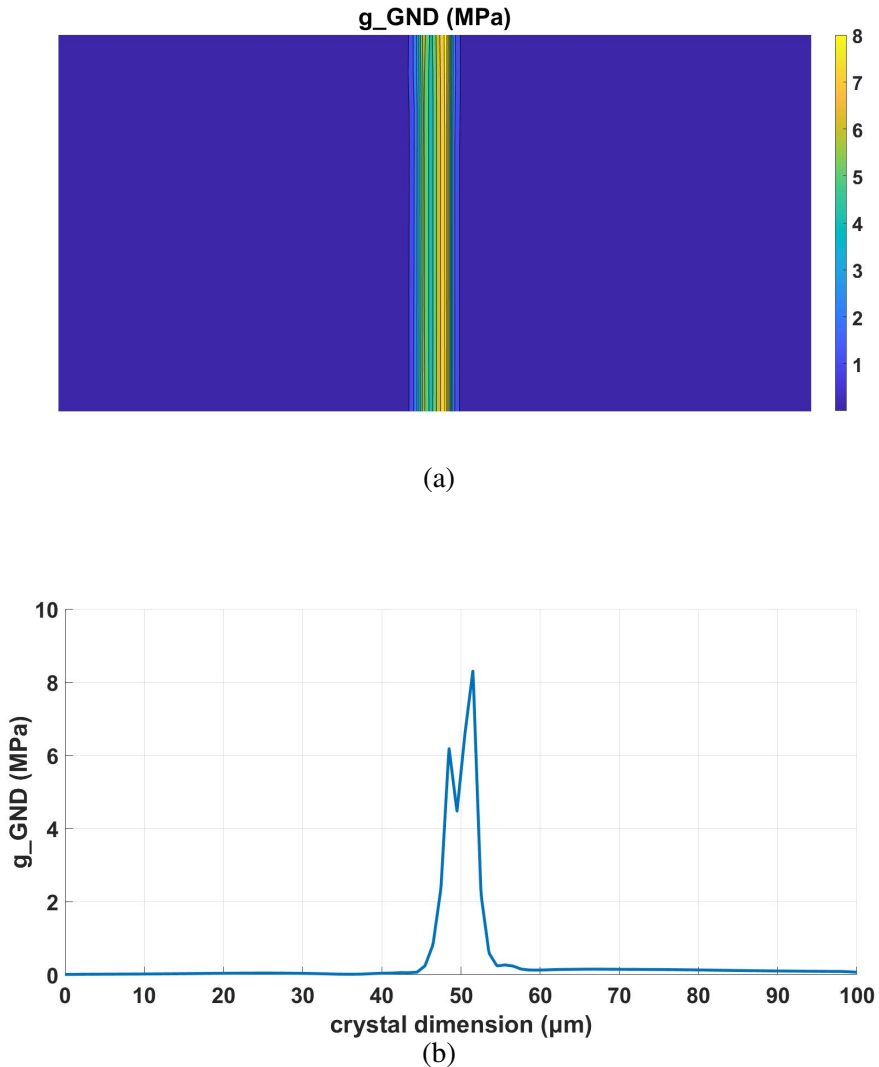


Figure 3.11: Distribution of maximum slip system resistance due to GND amongst all the slip systems after unloading for the bicrystal with grains having 45° and 0° Euler angles. (a) Contour, and (b) line plot along $(0, L_2/2)$ to $(L_1, L_2/2)$.

3.7 Hall-Petch Effect in Bicrystal

It is well established that the materials having smaller grains have higher strength compared to those with larger grain size. Various processing methods in which the grain size can be controlled by controlling the cooling time and mechanical working, use this characteristic to tailor material mechanical properties. As discussed in Chapter 1, movements of dislocations cause plastic deformation and obstructions offered to the motion of these dislocations results in strengthening of the material. The GB regions have distinctly dif-

ferent behavior compared to the grain interior regions which results in development of plastic strain gradient near these regions. The gradient of plastic strain can be accommodated through the development of GND, which can further increase the slip system resistance near the GB region. For the microstructure with smaller grain size, the effect of the increased slip system resistances due to GND influences a relatively larger volume of the material than for larger grains. Thus, the GBs induce strengthening effect by disrupting the motion of dislocations resulting in the well known Hall-Petch behaviour [11; 12].

The Hall-Petch relation expresses the yield strength of a material with the grain diameter (D) following

$$\sigma_y = \sigma_0 + \frac{K}{\sqrt{D}} \quad (3.1)$$

where σ_y and D represent the yield stress and grain diameter of material respectively, and σ_0 and K are constants. To verify the effect of grain size on macroscopic yield stress a bicrystal problem as described in Section 3.1 is chosen. The set of Euler angle is chosen as 45° and 0° , which is shown schematically in Figure 3.12. The three set of grain diameters (D) chosen to verify the Hall-Petch effect are $50\mu m$, $100\mu m$ and $150\mu m$. The thickness of GB region is taken as 2% of the grain diameter for which the convergence is verified in Section 3.3.1.

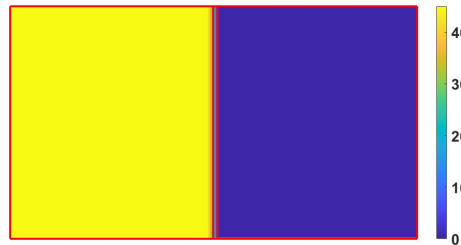
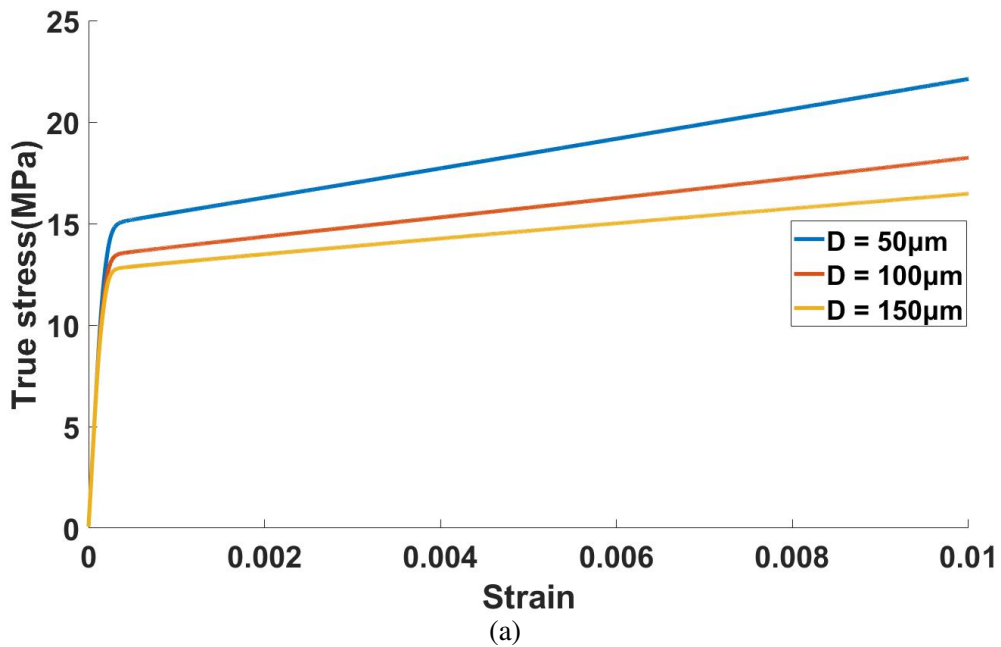


Figure 3.12: Bicrystal microstructure used for verifying the Hall-Petch effect. In the bicrystal the Euler angle of the left grain = 45° and the Euler angle of the right grain = 0° .

Figure 3.13(a) shows the effect of grain size on the macroscopic stress-strain response. For $D = 50\mu m$ we are getting the highest yield stress and hardening slope followed by that for $D = 100\mu m$ and $D = 150\mu m$ respectively. To verify that the grain size de-

pendence of yield stress follows Hall-Petch relation (Equation (3.1)), the yield stress (σ_y) at three different strain offset levels is plotted against $1/\sqrt{D}$ in Figure 3.13(b). It gives a linear fit with the slope representing the constant K of Hall-Petch relation. From this figure we can conclude that the Hall-Petch slope increases with the increasing strain level because of the stronger strain hardening effect induced by the piled-up dislocations. The calculated Hall-Petch constants at three different strain levels are presented in Table 3.2. Here the 0.03% corresponds to first yield region which the model is able to capture because of the unloading-reloading technique discussed in Section 3.6.



(a)

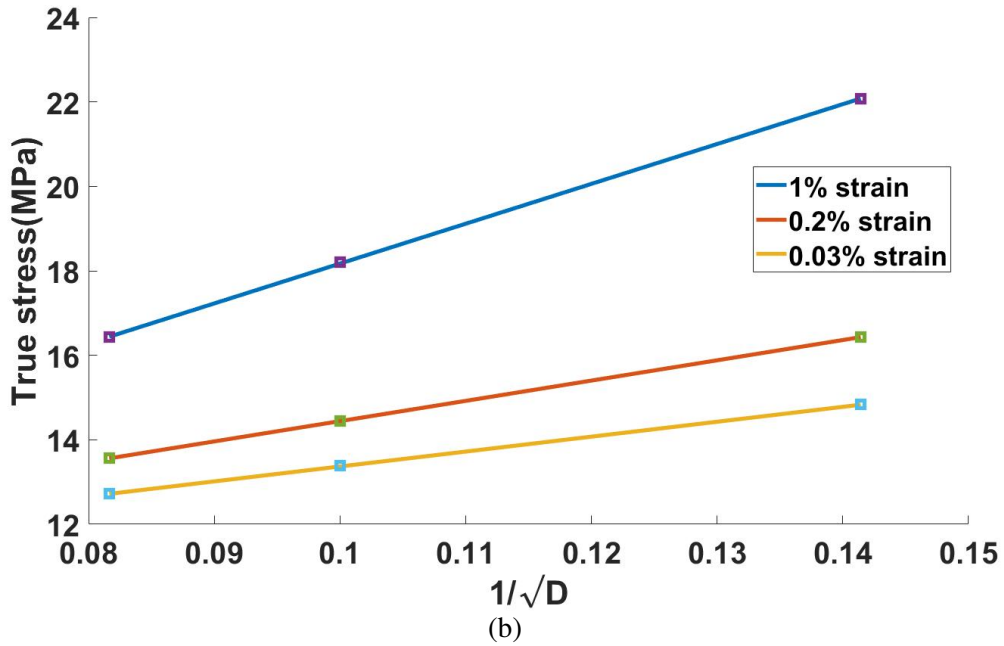


Figure 3.13: Effect of grain size on yield stress of the material. (a) Macroscopic stress-strain response for three different grain sizes; (b) Hall-Petch slope at three different strain levels.

Table 3.2: Hall-Petch slopes at three different strain levels for a bicrystal with 45° misorientation.

Strain level	K (MPa $m^{0.5}$)
0.03 %	0.035
0.2 %	0.048
1 %	0.095

3.7.1 Spatial Variation of CPFEM Variables under Bicrystal Deformation

For better understanding of the working mechanism of GB model presented in this work, some of the local response parameters including accumulated slip, slip system resistance, components of plastic strain and stresses are elaborated below using contours and variation across the crystal on a horizontal line passing through center of the crystal. In

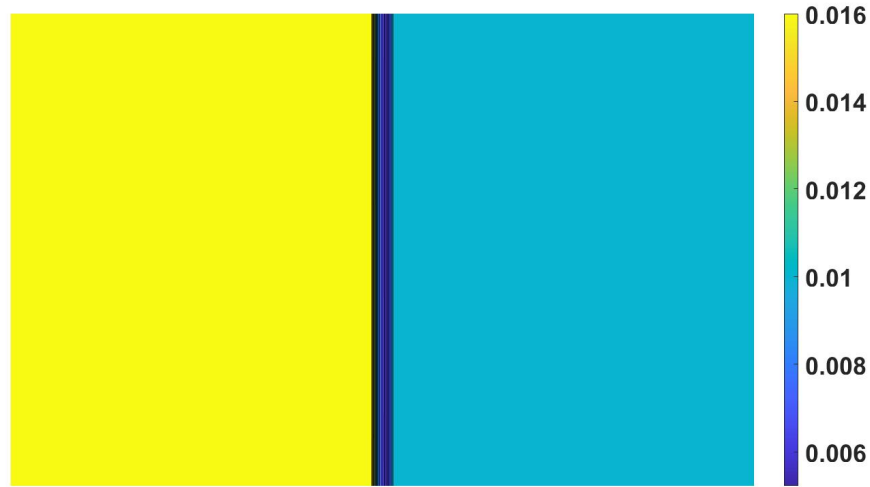
reference to Figure 3.1 the end point coordinates of this line can be described as $(0, L_2/2)$ and $(L_1, L_2/2)$. Hereafter the line will be referred as A-B.

Accumulated slip

Figure 3.14 shows the variation of maximum accumulated slip amongst all the slip systems on A-B at 1% strain level. Here accumulated slip is defined as

$$\gamma_a^\alpha = \int \dot{\gamma}^\alpha dt \quad (3.2)$$

Where γ_a^α and $\dot{\gamma}^\alpha$ are the accumulated slip and slip rate on a slip system α . We can clearly see in the figure shown below, that the gamma accumulated values are higher for 45° grain as compared to that for 0° grain. Moreover, these values get their minimum in the GB region because dislocation motion is difficult in this region.



(a)

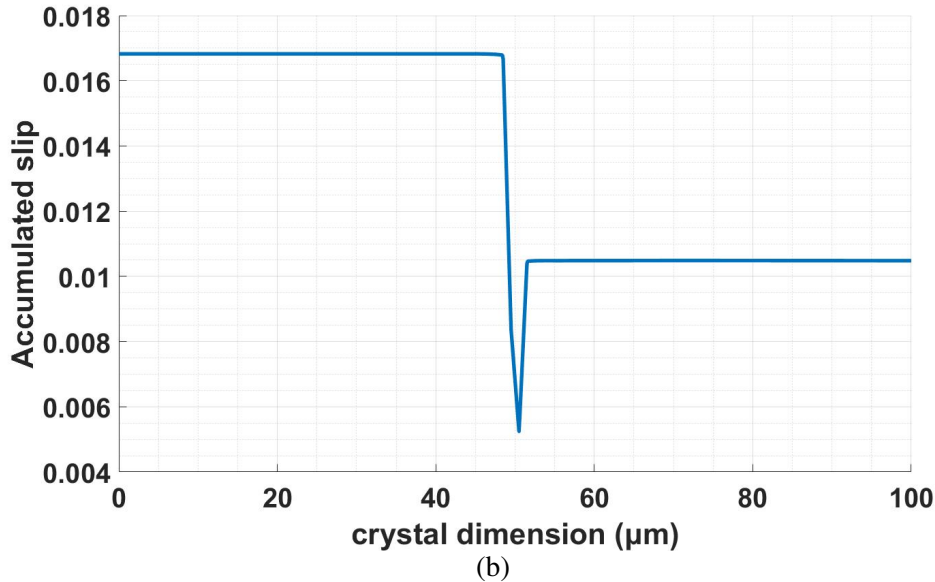


Figure 3.14: Variation of accumulated slip on the slip system having the maximum value for a bicrystal with Euler angle of left grain = 45° and Euler angle of right grain = 0° at applied uniaxial strain of 1%. (a) Contour plot and (b) variation on a line $(0, L_2/2)$ to $(L_1, L_2/2)$.

The accumulated slip on individual slip systems is shown in Figure 3.15. From the figure we can see that some of the slip system are having significant activation while some of them remain inactive; for example the 3^{rd} and 7^{th} are the most activated slip systems in 45° grain while the 2^{nd} and 6^{th} are the most activated slip systems for 0° grain . The 1^{st} and 5^{th} slip systems remain almost inactive. The spike appearing in the GB region for the 5^{th} slip system is because of transmitted slip.

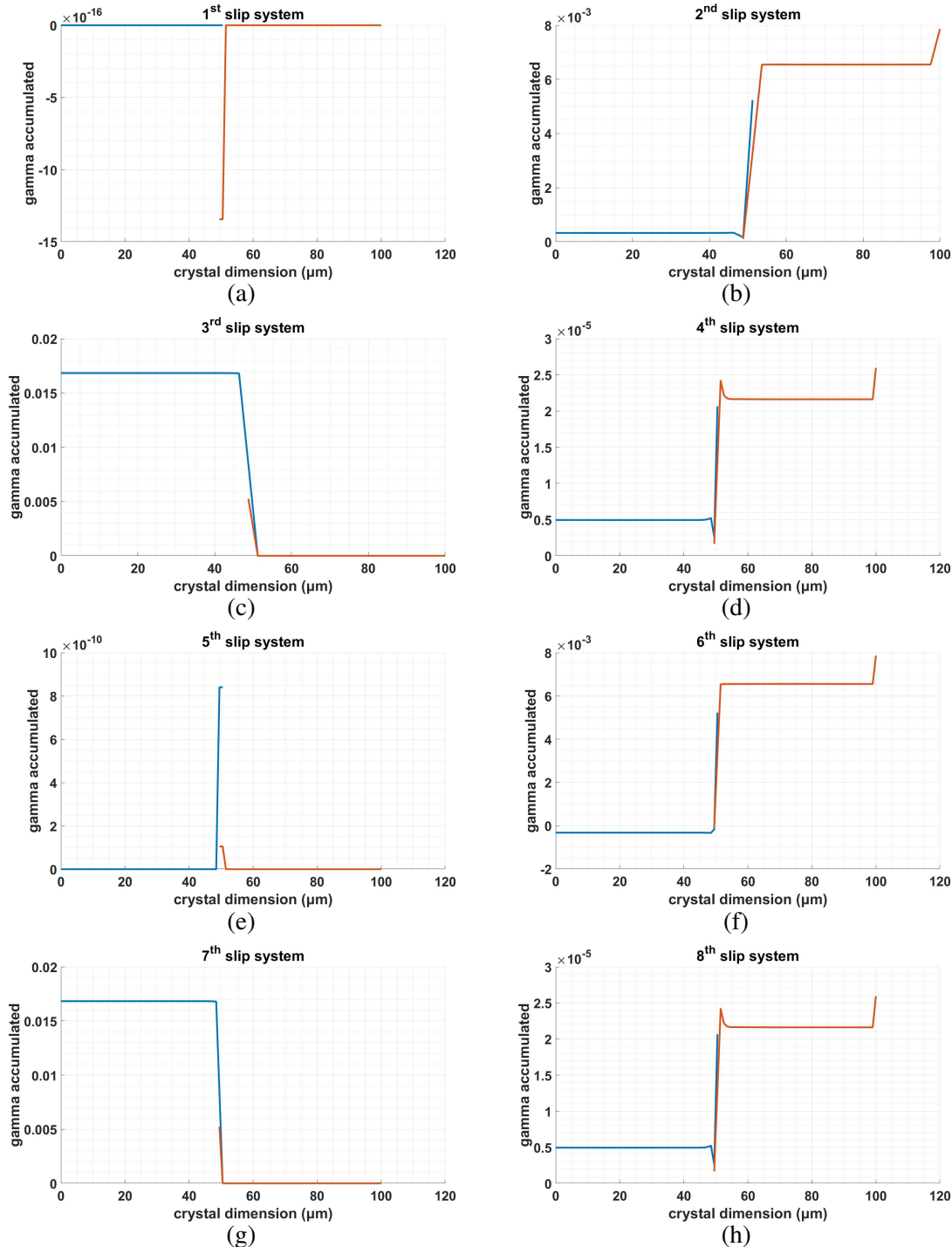


Figure 3.15: Variation of accumulated slip on individual slip systems for a bicrystal with Euler angle of left grain = 45° and Euler angle of right grain = 0° . (a) to (h) represent the eight slip systems of the grains.

Slip System Resistance

The contour and line plots shown below are the variations of slip resistance caused because of SSDs, GNDs and their cumulative effect. The values maximum of all the slip system is used to obtain the contour and line plots. From Figure 3.16, we can clearly see that GNDs mainly evolve near the GB region. This is so, because the gradient of plastic deformation calculate from Equation (2.16) is significant only near the GB region. In the grain interior region the plastic deformation is nearly homogeneous and hence the slip resistance caused by GNDs is almost zero.

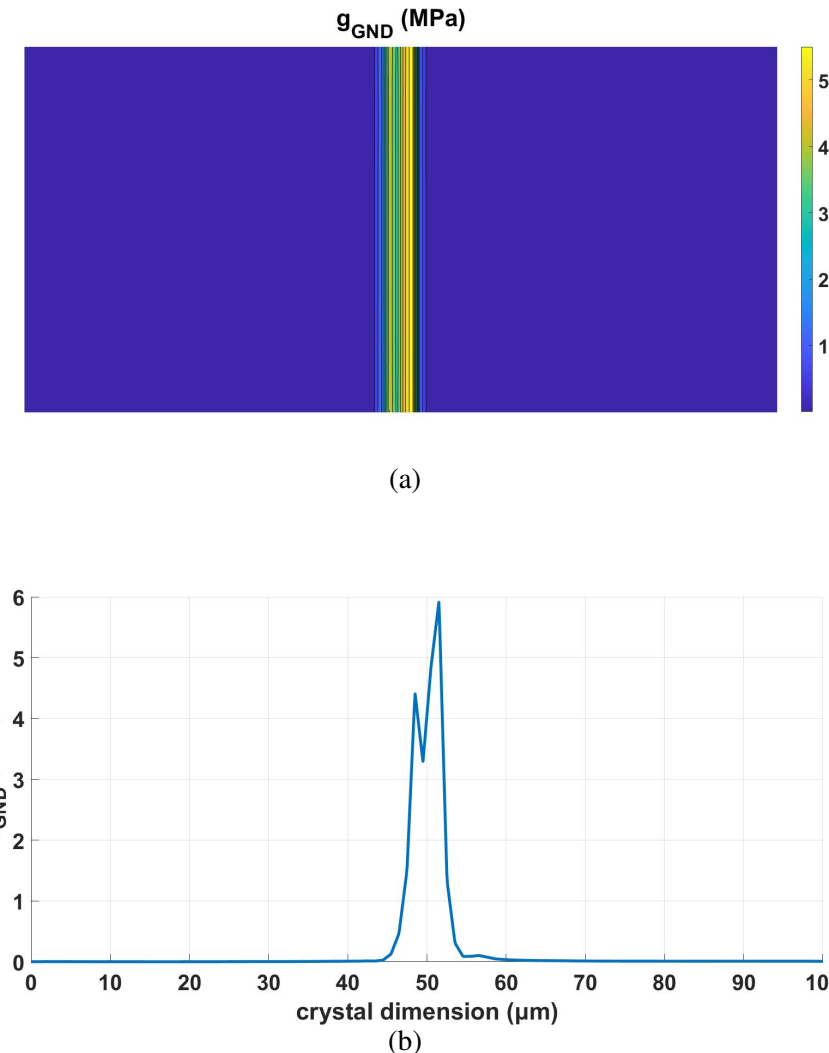
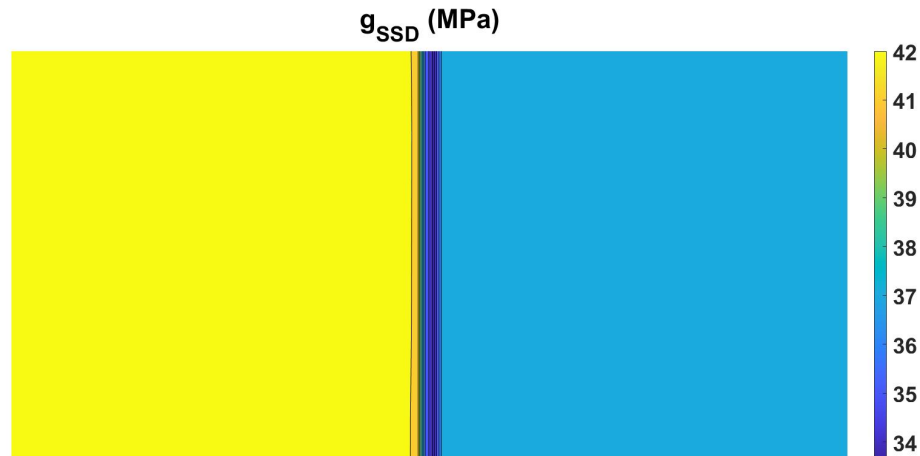
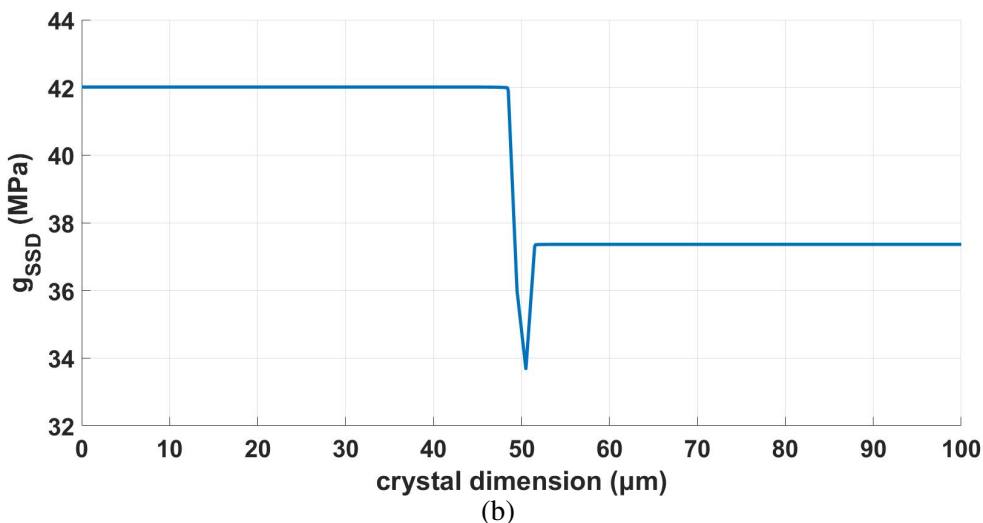


Figure 3.16: Variation of maximum GND based slip system resistance amongst all the slip systems at 1 % applied strain for the bicrystal with grains having 45° and 0° Euler angles. (a) Contour, and (b) line plot along $(0, L_2/2)$ to $(L_1, L_2/2)$.

The SSDs mainly evolve in the grain interiors where the motion of dislocations is easy when compared to the GB region as discussed in Chapter 1. In the model this behavior is incorporated by the use of additional energy penalty term in Equation (2.21). Due to the additional energy penalty, the slip rate is reduced in the GB which in turn reduces the evolution rate of the SSD caused slip system resistance (see Figure 3.17). The level of the slip resistance due to SSDs is different for the two grains depending upon their orientation which modifies the slip rates in them.



(a)



(b)

Figure 3.17: Variation of maximum SSD based slip system resistance amongst all the slip systems at 1 % applied strain for the bicrystal with grains having 45° and 0° Euler angles. (a) Contour, and (b) line plot along $(0, L_2/2)$ to $(L_1, L_2/2)$.

Figure 3.18 shows the variation of the maximum total slip system resistance amongst all the slip systems at a material point and is the cumulative effect of the slip system resistances offered by the SSDs and the GNDs. The total slip system resistance controls the rate of slip on the system and is governed by Equation (2.10). The effect of SSDs and GNDs can be distinctly verified in the plots shown in Figure 3.18. The difference in the level of maximum total slip system resistance in the two grain interior regions is due to the SSDs while the peak on the two sides of GB region is induced by the effect of GNDs.

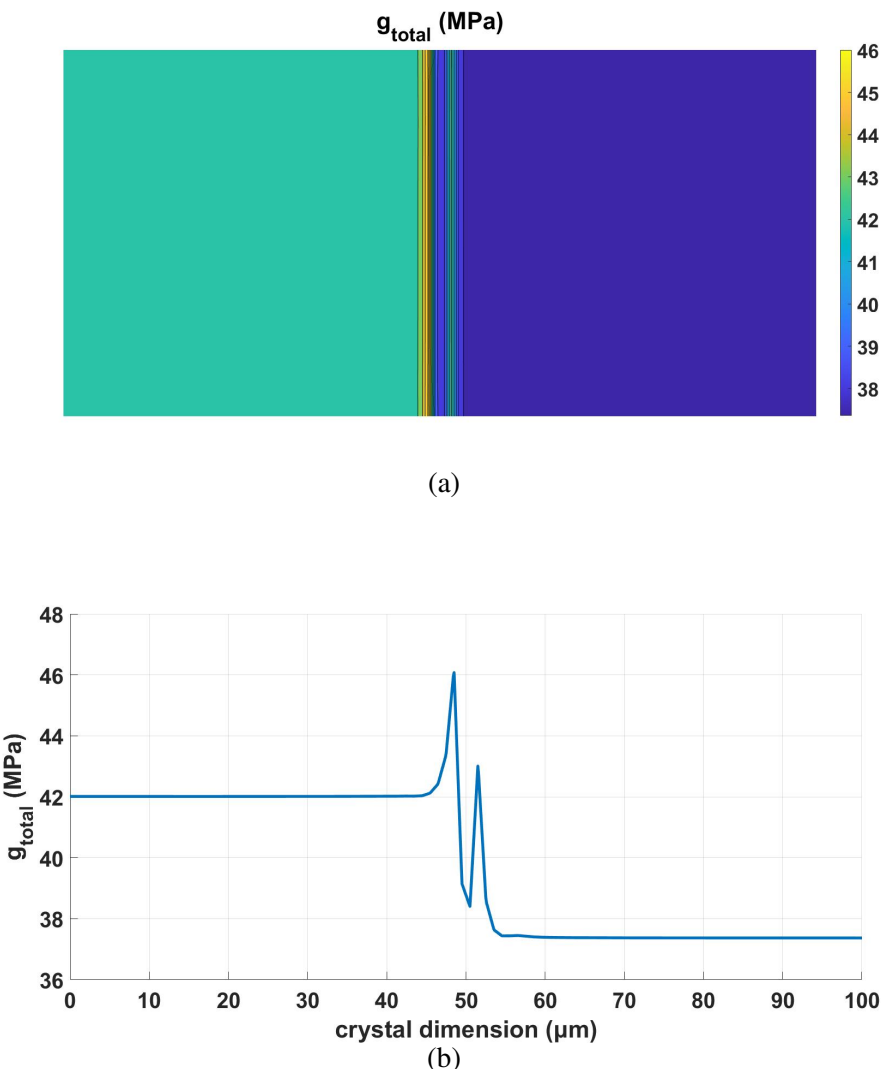


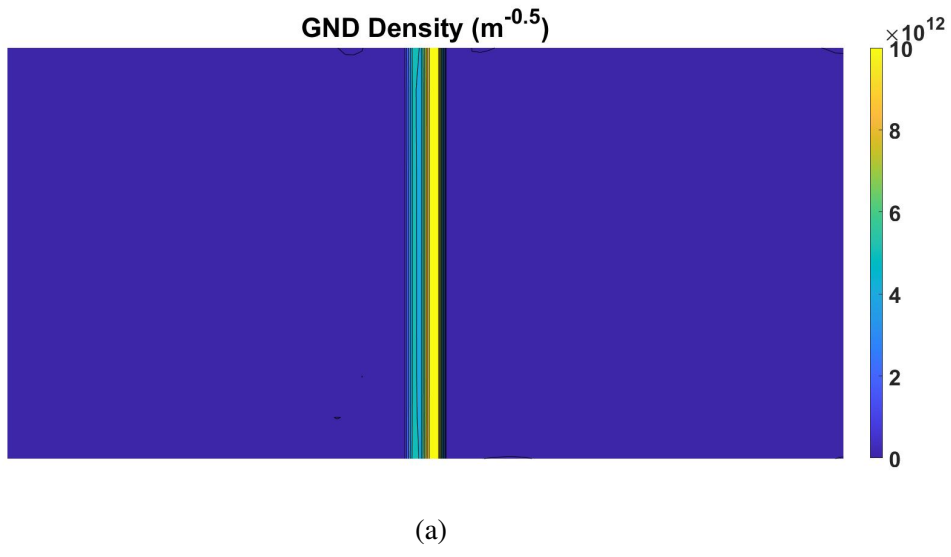
Figure 3.18: Variation of maximum total lip system resistance amongst all the slip systems at 1 % applied strain for the bicrystal with grains having 45° and 0° Euler angles. (a) Contour, and (b) line plot along (0, $L_2/2$) to (L_1 , $L_2/2$).

Dislocation Density

The term dislocation density is defined as the total number dislocation present per unit area or the total length of dislocation line per unit volume. Slip resistance (g) is related to dislocation density (ρ) as following

$$g = c G b \sqrt{\rho} \quad (3.3)$$

where G represents the shear modulus, b is the magnitude of Burgers vector and c is some constant [13]. By using this equation, the GND and SSD densities can be calculated from the corresponding slip system resistances. The variation of maximum GND density is shown below in the Figure 3.19. In the figure we can see that the GND density is almost zero in the grain interiors because the plastic deformation is nearly homogeneous in these regions. However in the near GB region the GND density has significantly evolved.



(a)

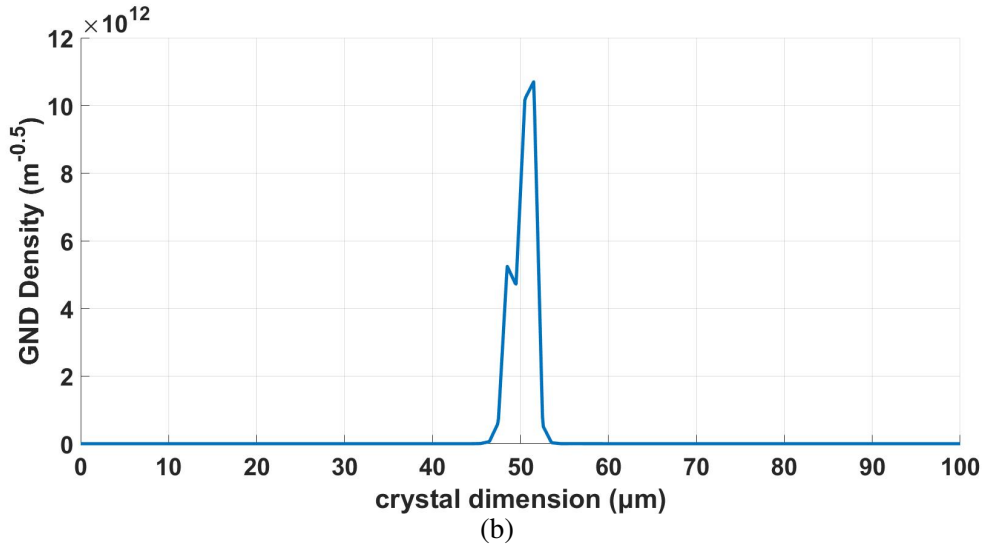
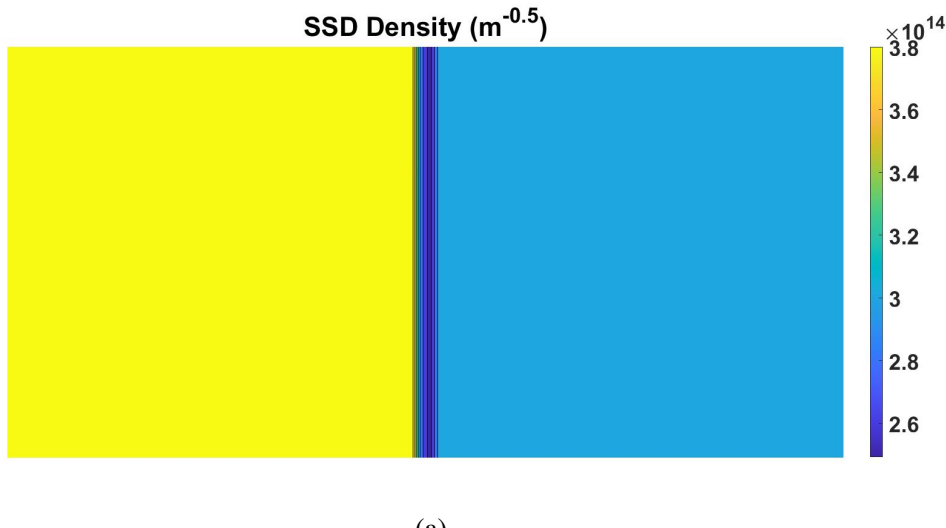


Figure 3.19: Variation of maximum GND density amongst all the slip systems at 1 % applied strain for the bicrystal with grains having 45° and 0° Euler angles. (a) Contour, and (b) line plot along $(0, L_2/2)$ to $(L_1, L_2/2)$.

Figure 3.20 shows the variation of maximum SSD density amongst all the slip systems at 1% applied strain. Here we can see that the SSDs have evolved in significantly in the grain interior regions where the motion of dislocations is easy and intensive. However, it can also be seen that the applied energy penalty in the GB region reduces the slip rate and hence reduces the evolution of SSD density in the GB region.



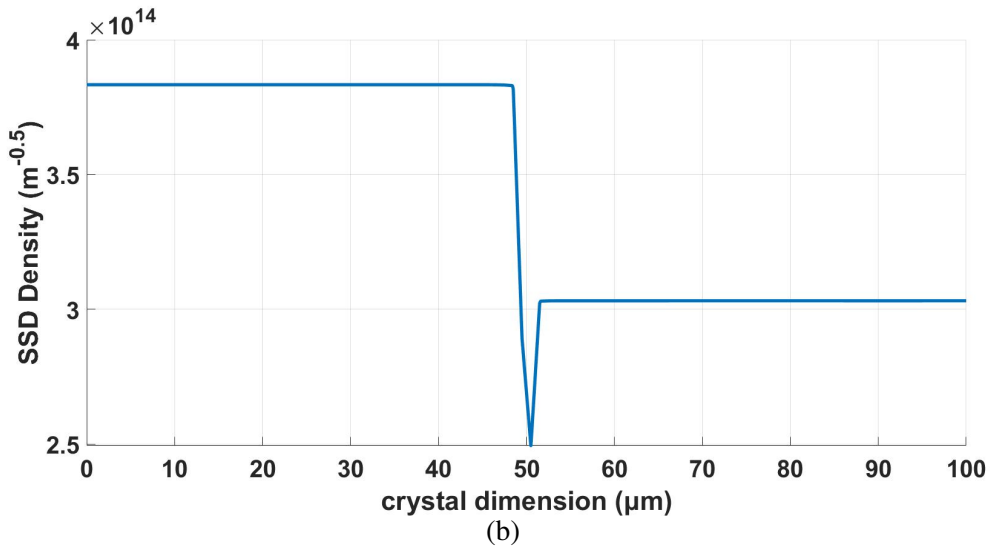


Figure 3.20: Variation of maximum SSD density amongst all the slip systems at 1 % applied strain for the bicrystal with grains having 45° and 0° Euler angles. (a) Contour, and (b) line plot along $(0, L_2/2)$ to $(L_1, L_2/2)$.

Components of Plastic Strain:

Variation of the four components of plastic strain for the 2D plane strain problem described in Section 3.1 are shown in Figures 3.21 to 3.24. The out of plane shear and normal strain components vanish for the chosen problem. For the applied uniaxial tensile deformation and the chosen reduced slip systems as described in Section 3.2, the planer shear strain component of the plastic strain (ϵ_{12}^p) is also very small compared to the normal in-plane plastic strain components ϵ_{22}^p and ϵ_{11}^p . The component ϵ_{22}^p is the applied plastic strain in the loading direction for which we are getting a corresponding lateral strain of opposite nature ϵ_{11}^p so that the volume of the specimen remains conserved. Moreover, from the distribution of ϵ_{22}^p we can see that the GB region has the least plastic strain value. This can be physically understood from that fact the motion of dislocation in the GB region is difficult as compared to grain interior regions. In the formulation it is incorporated in Equation (2.21), where the applied energy penalty reduces the slip rate in the GB region. The two grains have different levels of plastic strains (nearly uniform throughout the grain interior region) depending upon their orientations which modifies the respective slip rates.

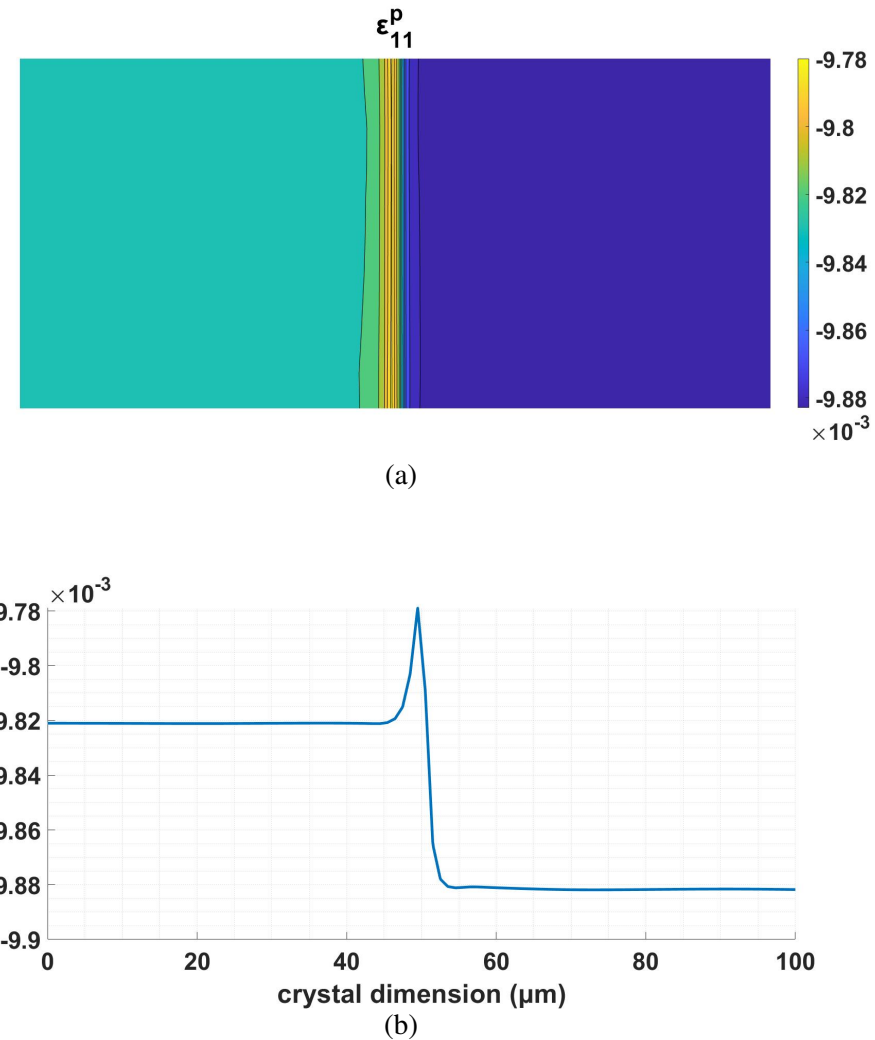
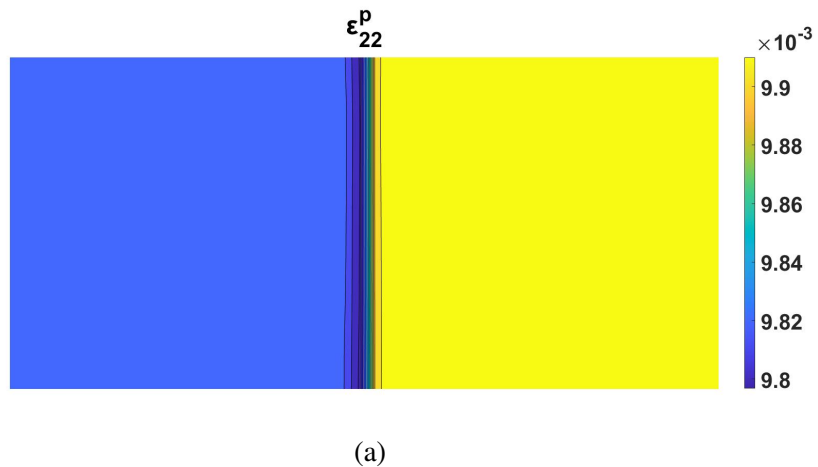


Figure 3.21: Variation of ϵ_{11}^p at 1 % applied strain for the bicrystal with grains having 45° and 0° Euler angles. (a) Contour, and (b) line plot along line A-B.



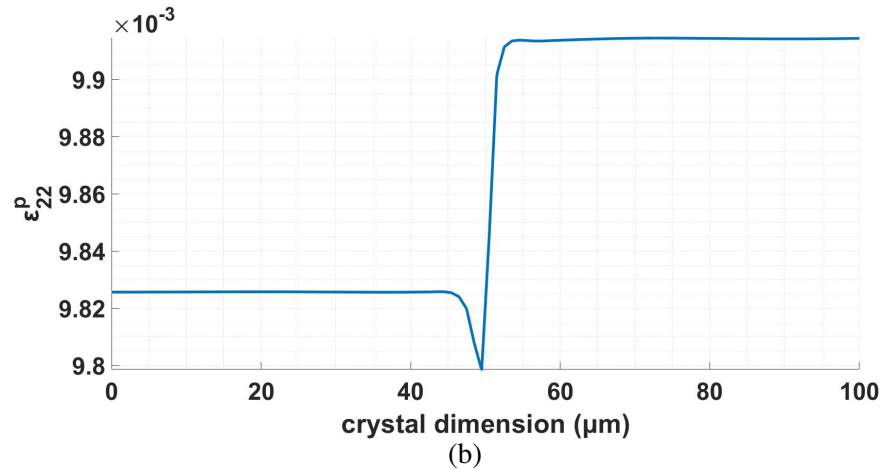


Figure 3.22: Variation of ϵ_{22}^p at 1 % applied strain for the bicrystal with grains having 45° and 0° Euler angles. (a) Contour, and (b) line plot along line A-B.

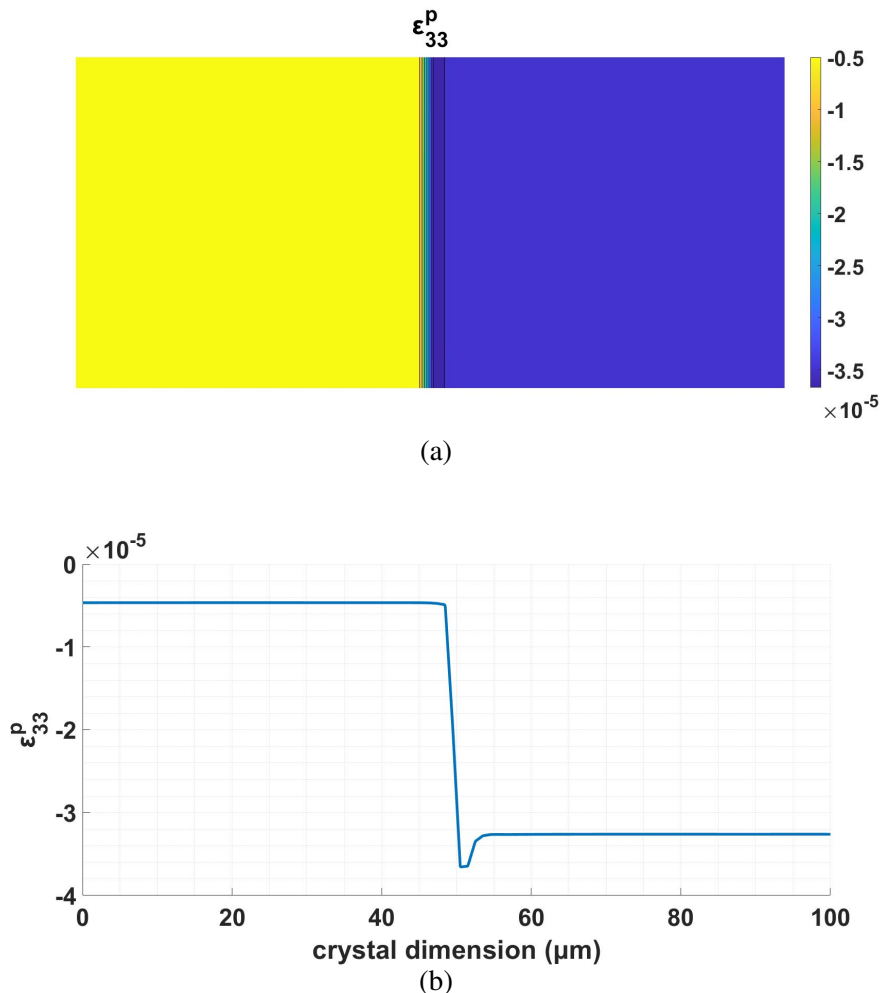


Figure 3.23: Variation of ϵ_{33}^p at 1 % applied strain for the bicrystal with grains having 45° and 0° Euler angles. (a) Contour, and (b) line plot along line A-B.

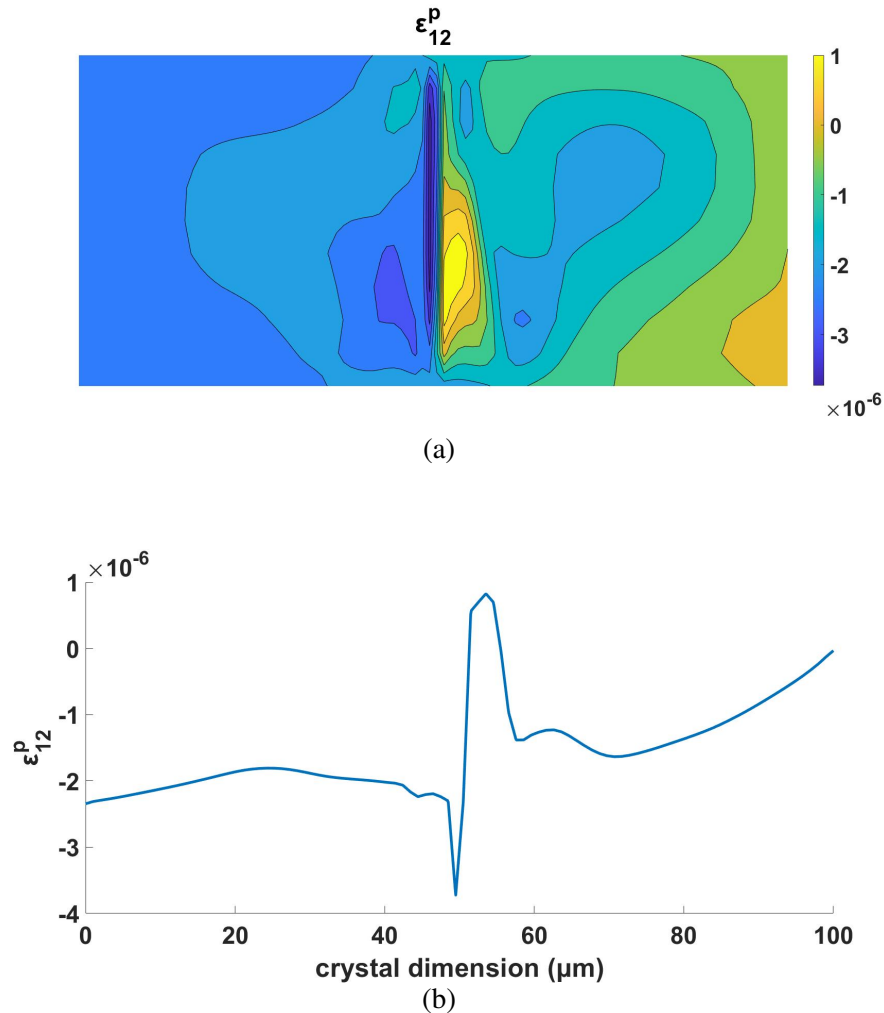


Figure 3.24: Variation of ϵ_{12}^p at 1 % applied strain for the bicrystal with grains having 45° and 0° Euler angles. (a) Contour, and (b) line plot along line A-B.

Components of Stress

The variation of the four components of stresses are shown in Figures 3.21 to 3.24 for the 2D plane strain problem described in Section 3.1. The variation these stress components can be explained in reference with the plastic strain components, boundary conditions and loading direction. The two out of plane shear stress components vanish as there are no out of plane shear strain. Moreover, we have seen in the Figure 3.24 that the in plane shear strain component is also very small for the applied loading and hence the planer shear stress component is also very small. The applied boundary conditions are described in Section 3.1 from which we can see that the both left and right faces of the domain are left

as free surfaces and therefore to maintain the stress equilibrium in 11 direction, the lateral normal stress component S_{11} gets balanced to a nearly zero value. S_{22} and S_{33} are having significant values.

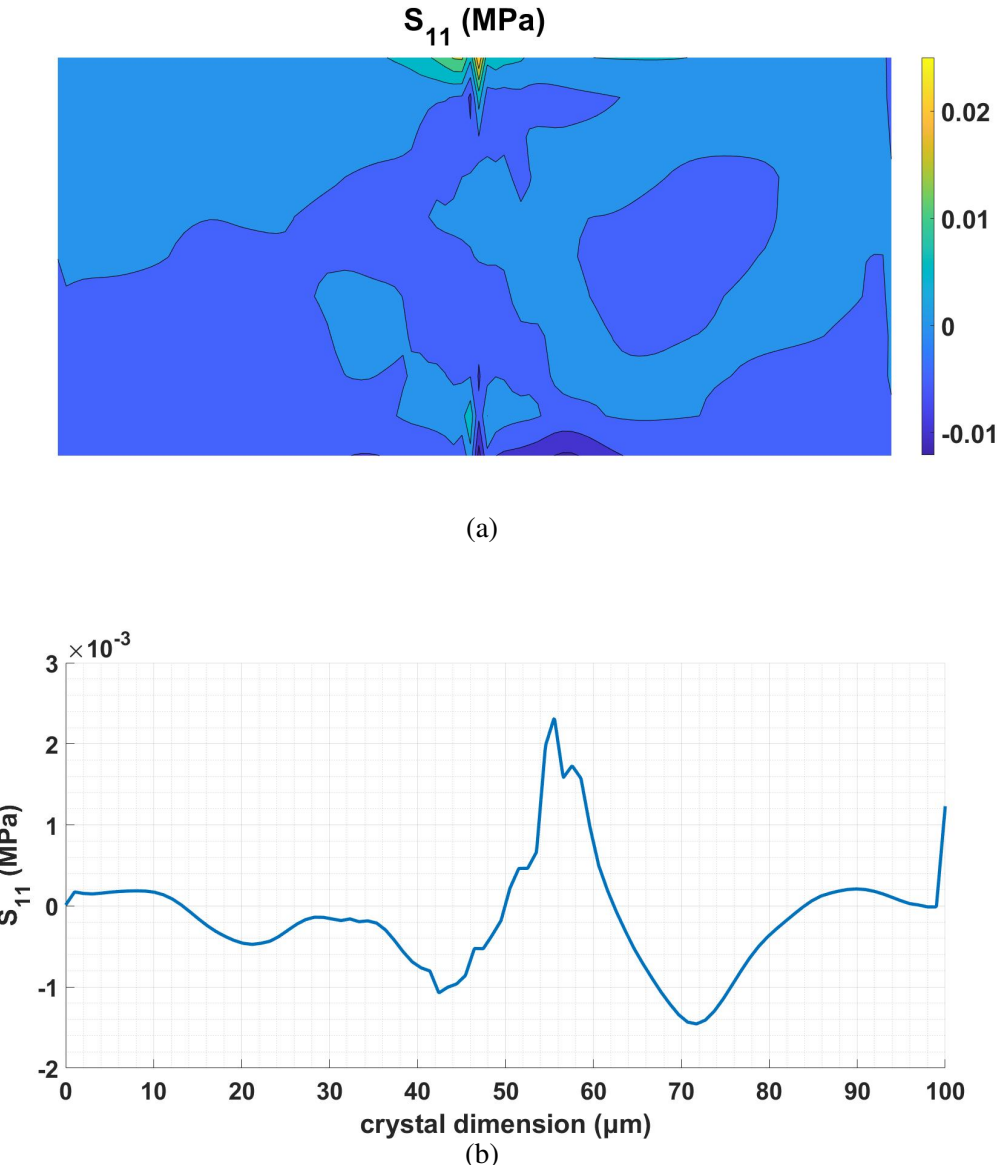


Figure 3.25: Variation of σ_{11} at 1 % applied strain for the bicrystal with grains having 45° and 0° Euler angles. (a) Contour, and (b) line plot along $(0, L_2/2)$ to $(L_1, L_2/2)$.

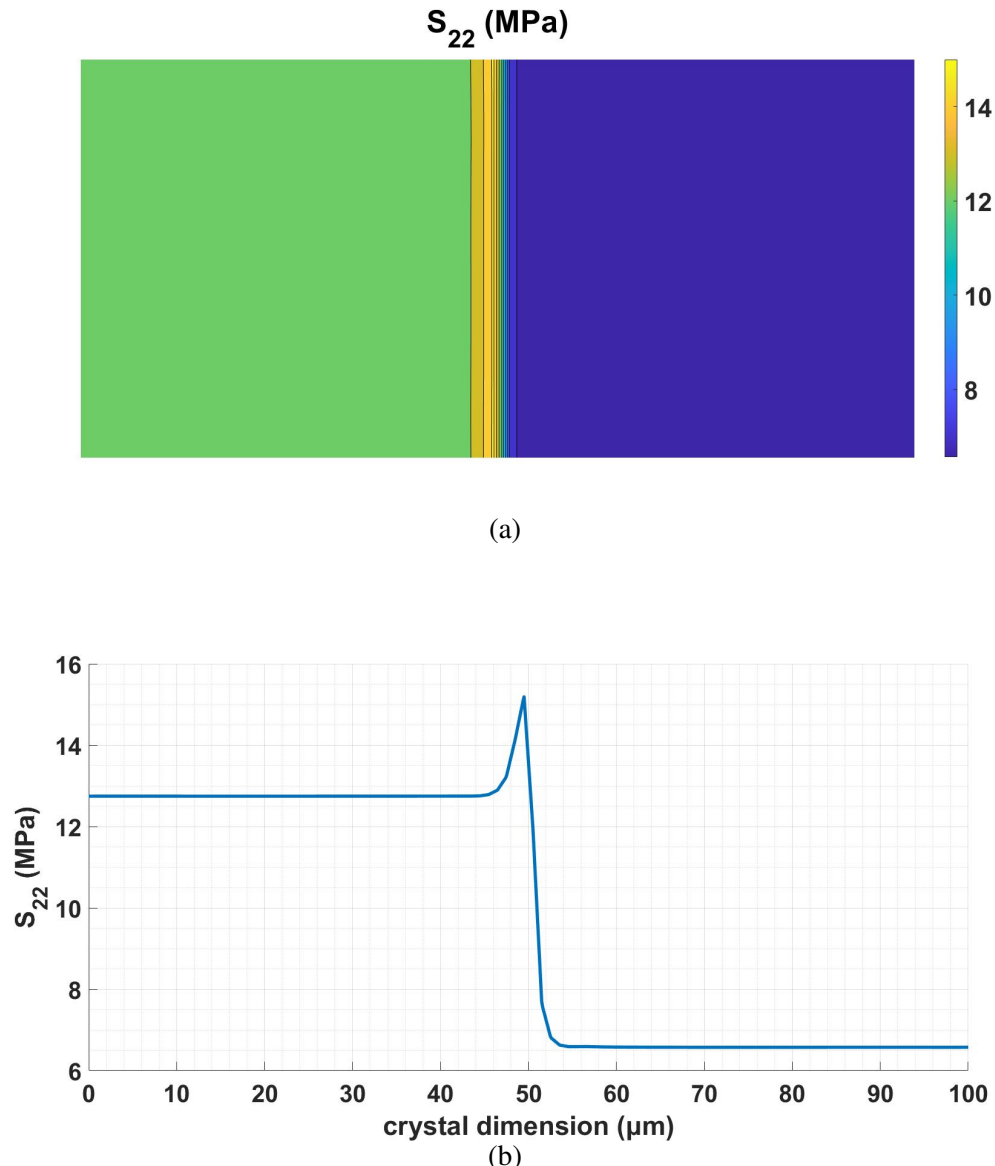


Figure 3.26: Variation of σ_{22} at 1 % applied strain for the bicrystal with grains having 45° and 0° Euler angles. (a) Contour, and (b) line plot along $(0, L_2/2)$ to $(L_1, L_2/2)$.

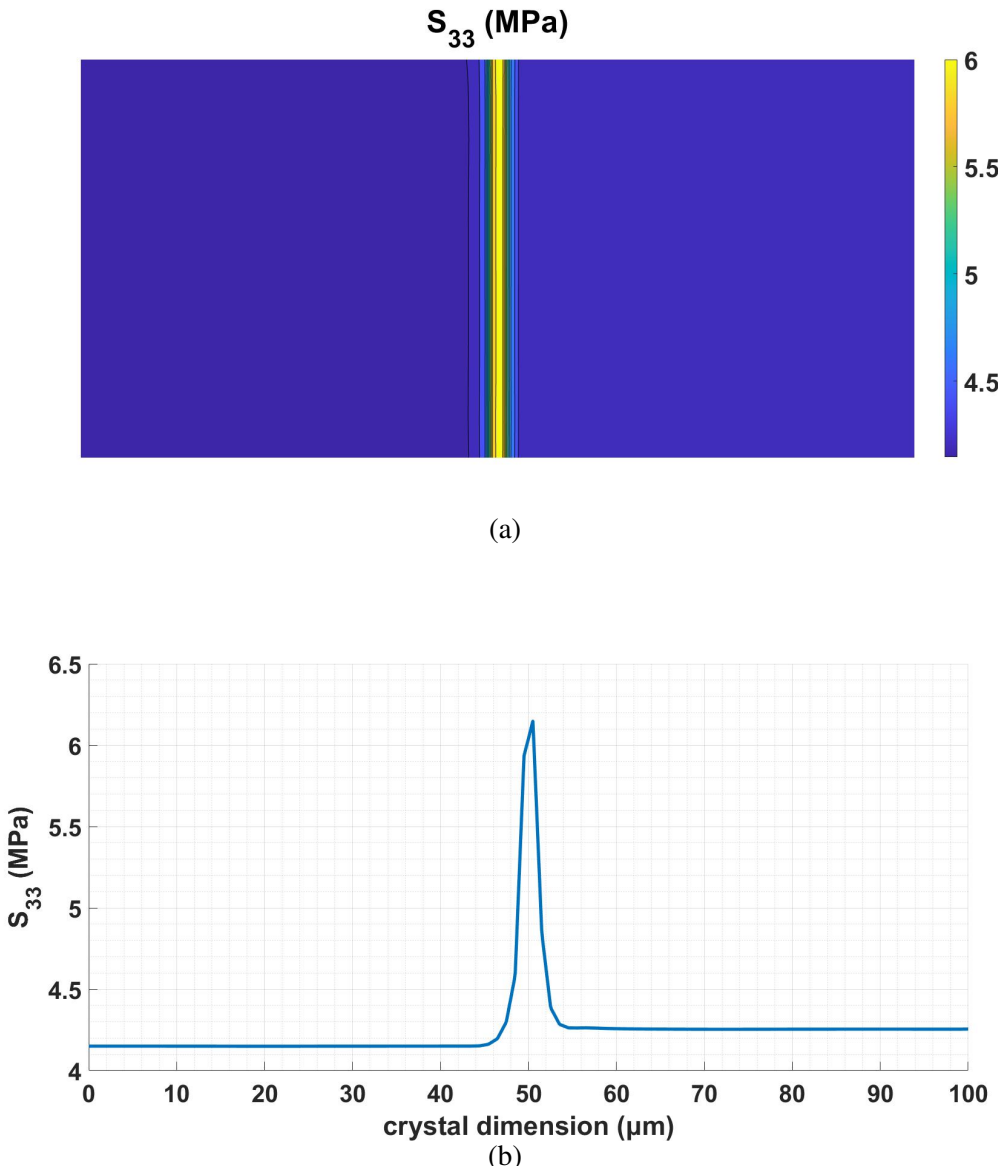


Figure 3.27: Variation of σ_{33} at 1 % applied strain for the bicrystal with grains having 45° and 0° Euler angles. (a) Contour, and (b) line plot along $(0, L_2/2)$ to $(L_1, L_2/2)$.

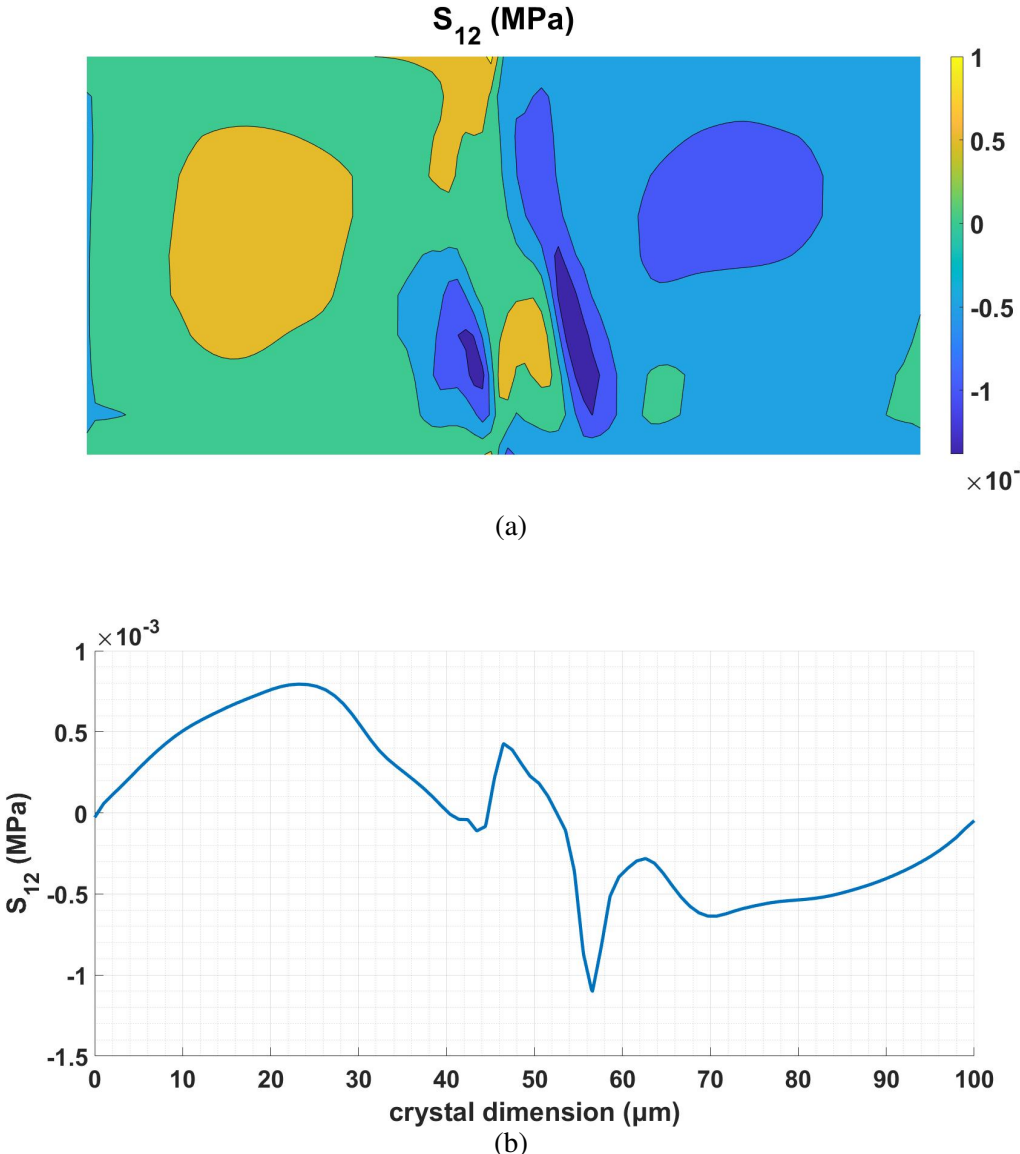


Figure 3.28: Variation of σ_{12} at 1 % applied strain for the bicrystal with grains having 45° and 0° Euler angles. (a) Contour, and (b) line plot along $(0, L_2/2)$ to $(L_1, L_2/2)$.

3.8 Effect of Misorientation of Grains on Hall-Petch Behavior

Depending upon the misorientation of neighbouring grains the GBs are classified as low and high angle GBs. The high angle GBs offer higher resistance for penetration events across the interface [29]. In our model this effect is brought through the calculation of

energy penalty based on misalignment of slip systems. It is hypothesized that the Q_{GB} calculated from Equation (2.33) will be higher for GBs with higher misorientation. To find the effect of misorientation on Hall-Petch constants, we consider two bicrystals with misorientations of 30° and 15° . The schematic of the two cases is shown in Figure 3.29. For both these cases, three different grain sizes $50\mu m$, $75\mu m$ and $150\mu m$ are considered. The thickness of GB region is taken as 2% of the grain diameter based on the study in Section 3.3.1.

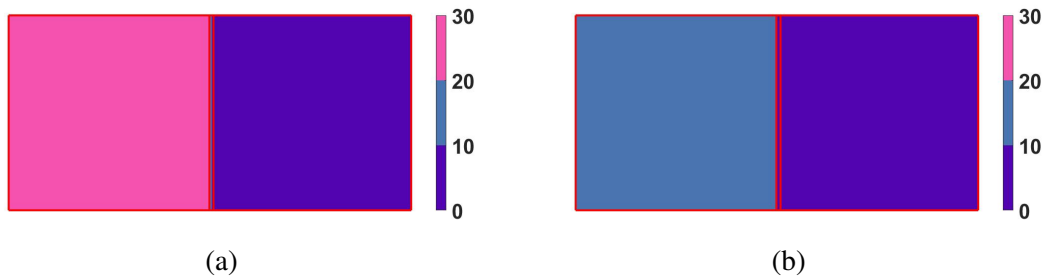


Figure 3.29: Bicrystal microstructures to evaluate the influence of misorientation on Hall-Petch behavior. (a) Grains having Euler angles of 30° and 0° , and (b) Grains having Euler angles of 15° and 0° .

The macroscopic stress-strain responses for the different misorientations and grain sizes are plotted in Figure 3.30(a). The figure shows that the case with 30° misorientation has higher initial yield stress as well as higher hardening slope when compared with that for 15° misorientation. Such difference in the response of the two cases is caused by combined orientation and misorientation effect. The change in the initial yield stress is brought in because of the change in slip resistance caused by SSDs while the difference in hardening is caused due to change in slip resistance cause by GNDs because the two cases have different misorientation resulting in different gradient in plastic deformation.

The effect of misorientation on Hall-Petch parameters are evident from Figure 3.30 which shows that the Hall-Petch constant (K) is higher for larger misorientation at all values of applied strain. The calculated Hall-Petch constants are presented in Table 3.3.

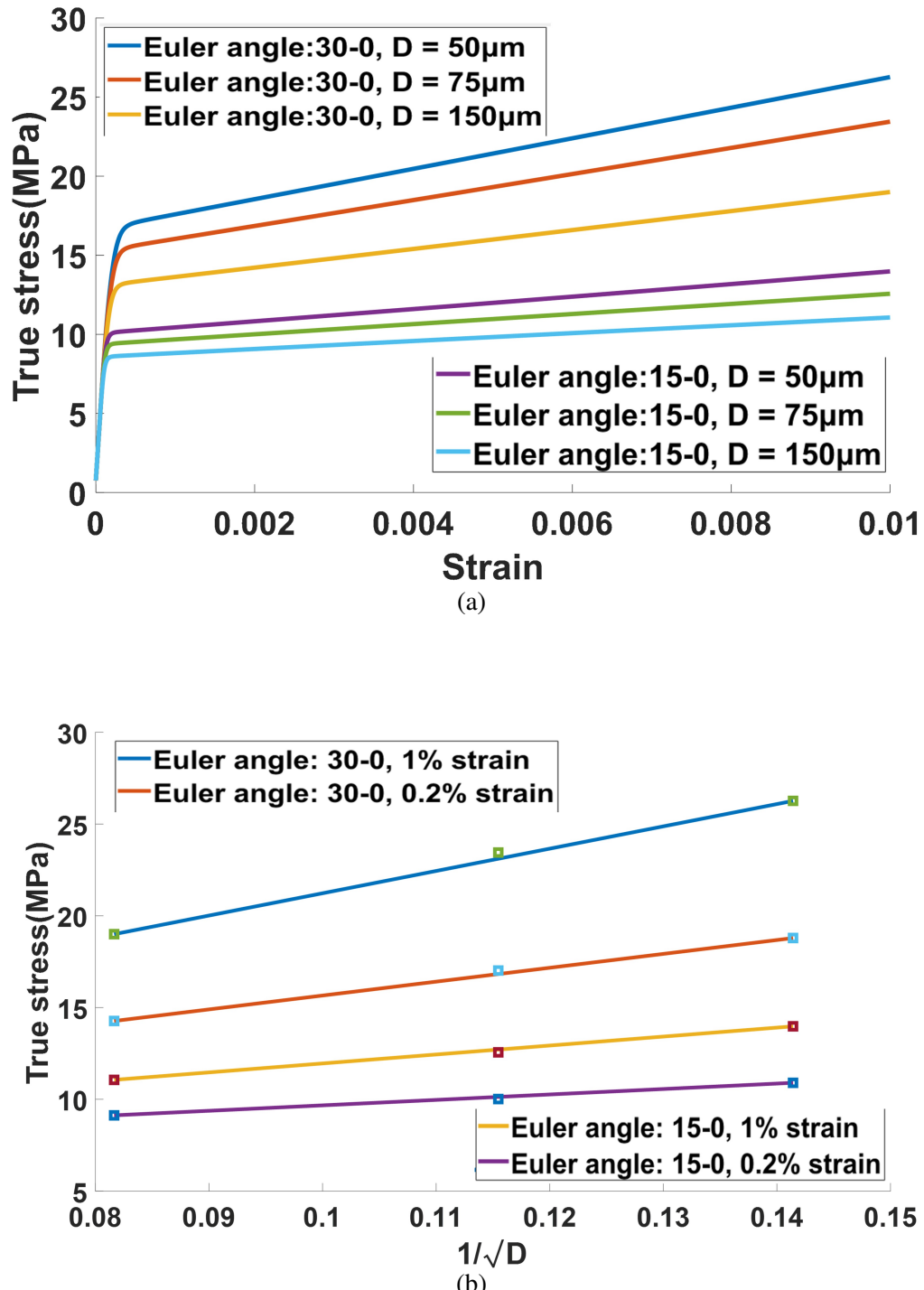


Figure 3.30: Misorientation effect in bicrystal. (a) Macroscopic stress vs strain for three grain sizes and (b) Variation of yield stress with grain size highlighting Hall-Petch behavior.

Table 3.3: Effect of misorientation of grains on Hall-Petch behaviour.

Euler angle	Strain level	σ_0 (MPa)	K (MPa $m^{0.5}$)
$30^\circ - 0^\circ$	0.2 %	11.15	0.038
$30^\circ - 0^\circ$	1 %	14	0.06
<hr/>			
$15^\circ - 0^\circ$	0.2 %	7.9	0.015
$15^\circ - 0^\circ$	1 %	9	0.025

3.9 Effect of Energy Penalty Evolution

The effective barrier offered by GBs for dislocation transmission increases with accumulated dislocations as discussed in Section 2.3. This can be modeled by increasing the energy penalty of a slip system for slip transmission across GBs (Equation (2.23)) with accumulated slip on that system. This evolved energy penalty results in development of higher plastic strain gradient and hence higher slip resistance offered by GNDs. The effect of this energy penalty evolution on macroscopic response is shown in Figure 3.31, in which a higher strain hardening behavior can be observed when the evolution for energy penalty is taken into consideration.

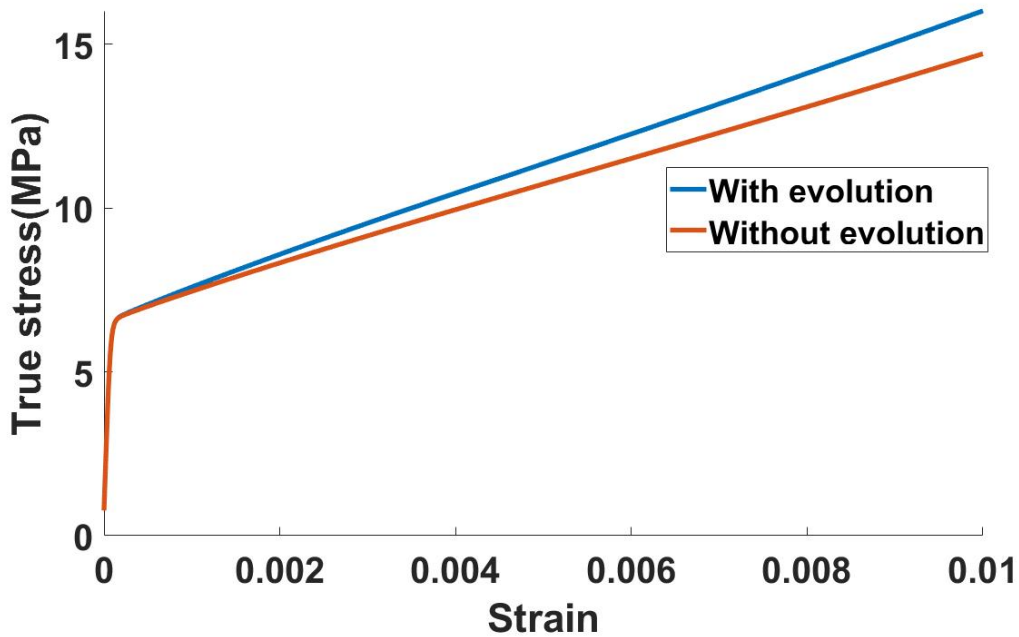


Figure 3.31: Effect of energy penalty evolution on macroscopic response.

The evolution of effective energy penalty for the first two slip systems of 45° grain is shown in Figure 3.32. It can be seen from Figure 3.32 (a) that the evolution of effective Q_{GB}^{eff} on 1st slip system is minimal and is due to near zero slip activity on this system. On the contrary, slip system 2 shows significant evolution of Q_{GB}^{eff} and is due to significant slip activity on this system. The variation of slip activities on these two slip systems have already been presented in Section 3.7.1.

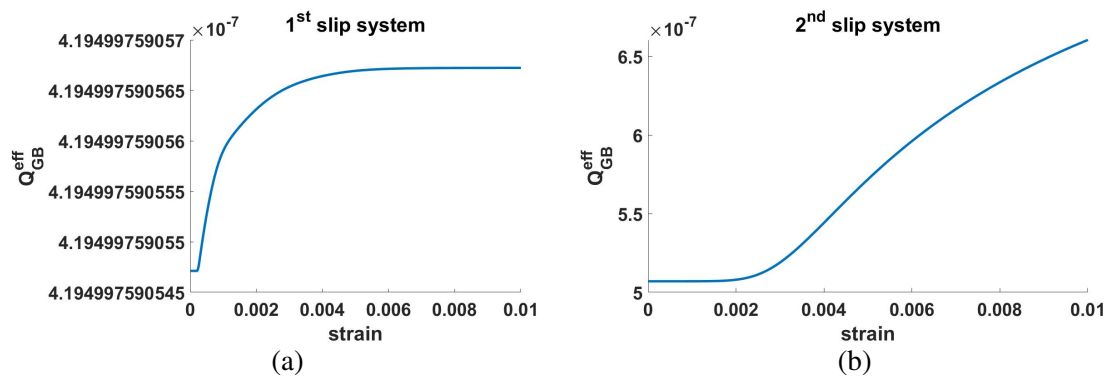


Figure 3.32: Evolution of energy penalty for individual slip systems of $45^\circ - 0^\circ$ bicrystal.

The use of an evolving energy penalty model signifies that the transmissibility across GBs reduce with deformation and finally the dislocations are unable to travel to any energetically favorable slip system of the neighboring grains. Most of the earlier models assumed the transmission-less behavior to develop the size dependent models. However, such an assumption leads to a higher yield stress as evident from Figure 3.31. Thus, the incorporation of dislocation transmission across GBs needs to be considered to obtain physically realistic size dependent crystal plasticity models.

CHAPTER 4

Hall-Petch Effect in Polycrystals

The effect of grain size on the macroscopic elasto-plastic behaviour is already verified for the bicrystal problems using three different misorientations in Sections (3.2 and 3.8). Polycrystals have certain added complications, where several number of grains are randomly oriented resulting in number of interface regions having different misorientations. Depending upon their orientation, the grains also show preferential yielding where some of the grains are yielded before others. Moreover, unlike bicrystal the internal grains of a polycrystal are surrounded by GBs on all the sides hence the plastic strain gradients developed in all the directions and affect the elasto plastic deformation behaviour. In this chapter, the Hall-Petch effect is verified for a 16 grain polycrystal and the evolution of slip system resistances, stress and strain components are discussed for uniaxial plane strain problem.

4.1 Model Description

The polycrystal specimen having 16 grains is subjected to uniaxial plane strain tensile deformation. The macroscopic boundary conditions are kept the same as those for the bicrystal problem described in Section 3.1. The thickness of the GB region is kept as 2% of the grain size. The four grain sizes chosen for verifying the Hall-Petch effect are $25\mu m$, $50\mu m$, $75\mu m$ and $100\mu m$. The Euler angles for the 16 grains are randomly selected ranging from 0° to 45° . The spatial distribution of Euler angles are presented in Figure 4.1 (a) in which the color bar shown represents the Euler angle of that specific grain. Figure 4.1 (b) shows a schematic representation of FEM mesh and GB regions separating the grain interiors. Using this figure we can express $L = 4D + 3W_{GB}$, where L , D and W_{GB} represent the size of domain, grain size and width of GB region respectively.

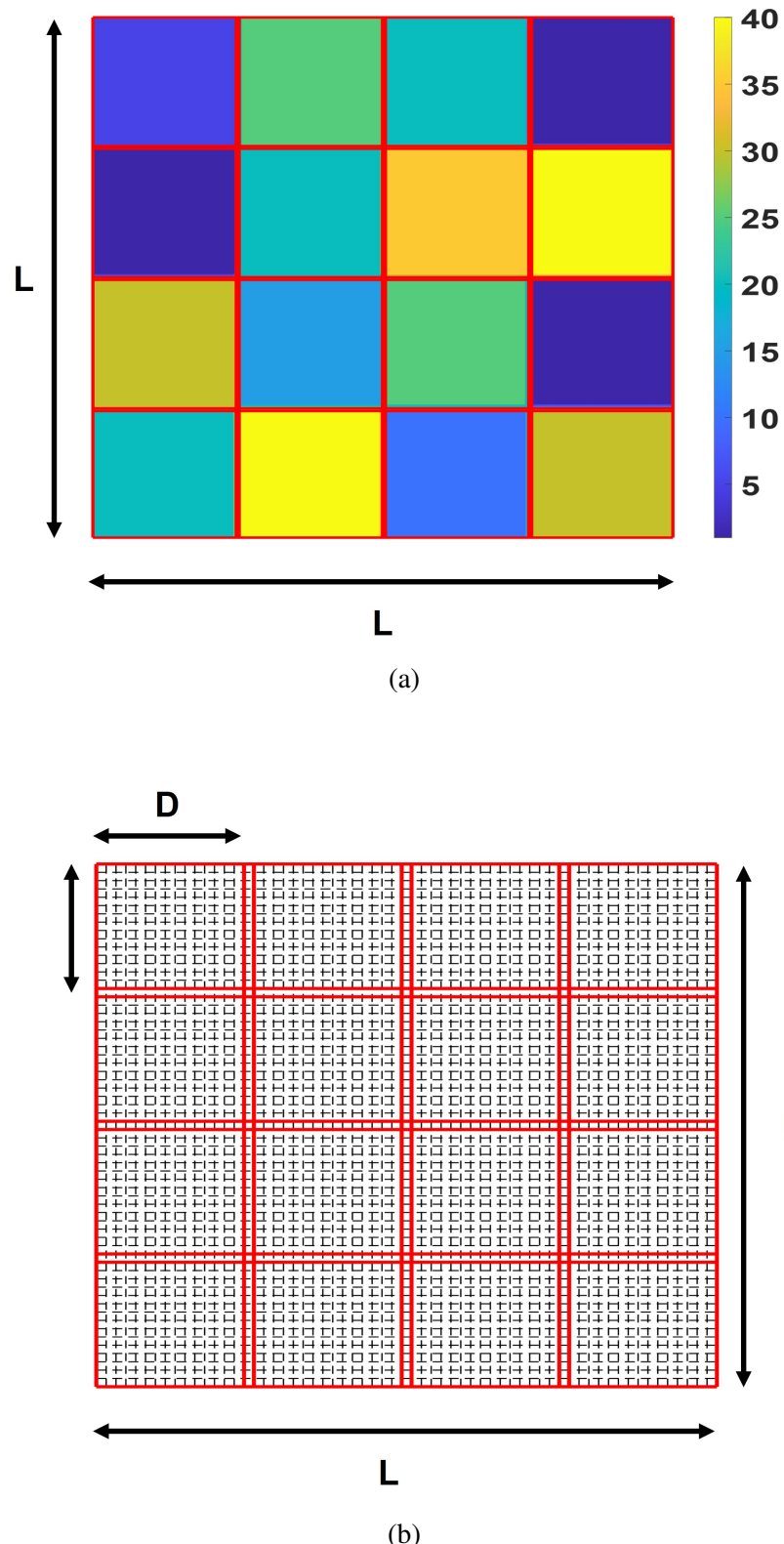
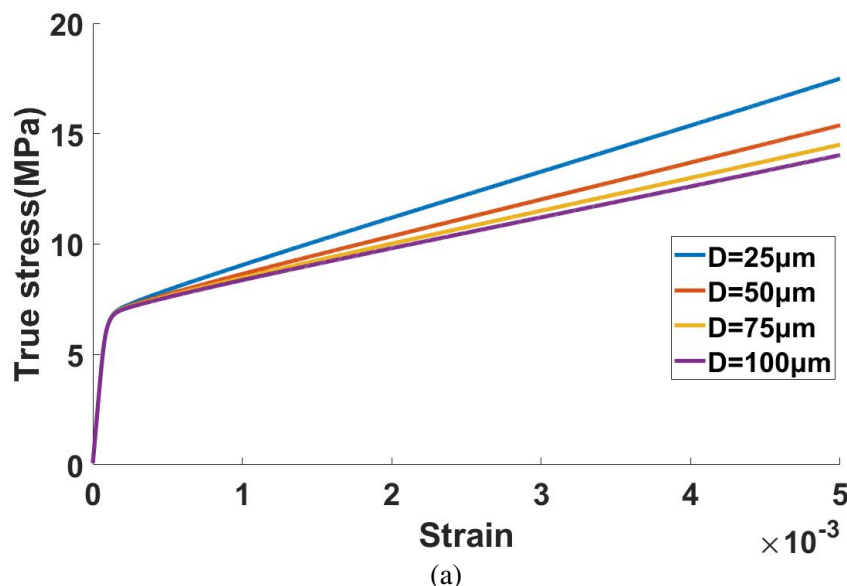


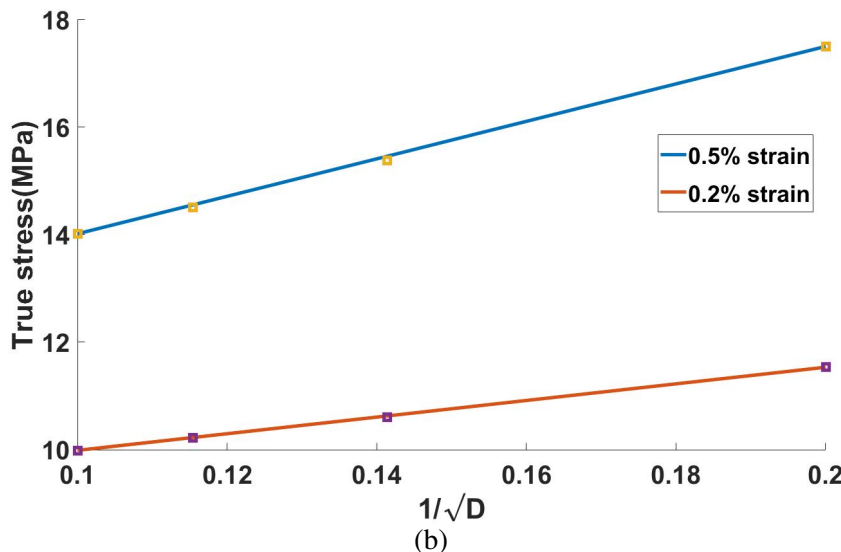
Figure 4.1: (a) Distribution of Euler angles in the polycrystalline domain. (b) Geometrical parameters of the polycrystal domain and FEM mesh.

4.2 Verification of Hall-Petch Effect

The polycrystal domain corresponding to the four different grain sizes, are uniaxially deformed up to 0.5% strain. The macroscopic stress-strain responses for the different grain diameters are shown in Figure 4.2 (a). The macroscopic stresses are plotted against the inverse of square root of grain sizes in Figure 4.2 (b).



(a)



(b)

Figure 4.2: (a) Macroscopic stress strain response on the polycrystal for four different grain sizes. (b) Variation of yield stress with grain size highlighting Hall-Petch behavior.

From the above figures we can easily visualize the grain size effect and the increase of Hall-Petch slope when the strain level is increased from 0.2% to 0.5%. The calculated Hall-Petch constants are presented in Table 4.2.

Table 4.1: Hall-Petch constants for 16 grain polycrystal

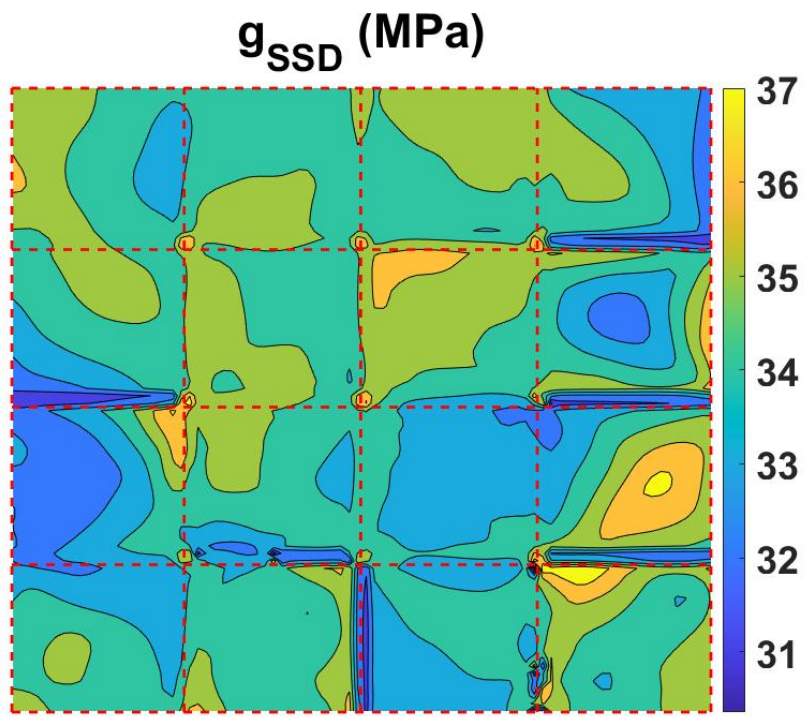
Strain level	σ_0 (MPa)	K (MPa $m^{0.5}$)
0.2 %	8.43	0.0155
0.5 %	10.5	0.035

4.3 Spatial Variation of CPFEM Variables under Polycrystal Deformation

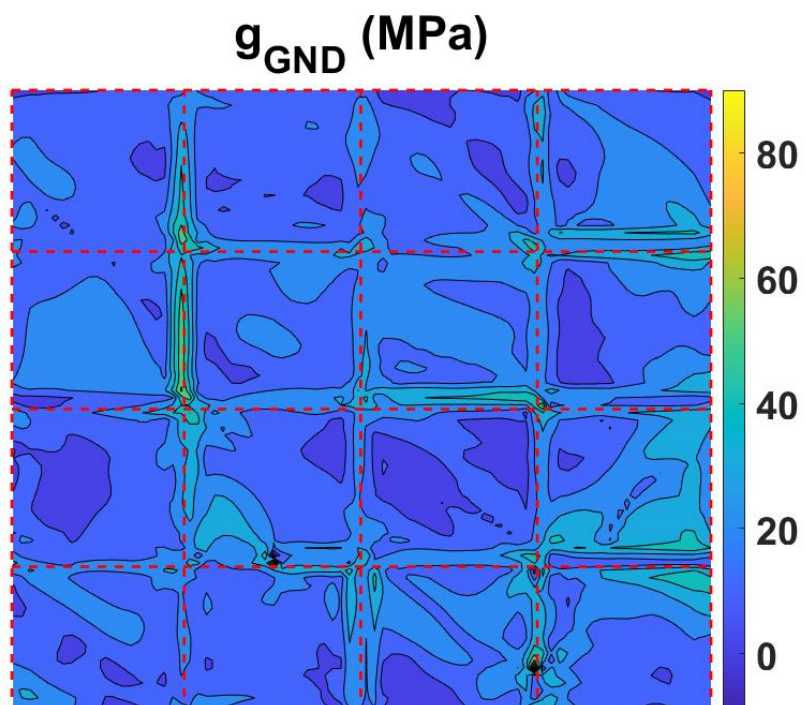
In this section some of the important characteristics of the polycrystalline deformation is discussed using various contour plots. The dotted lines are plotted to identify the boundaries of the grains.

4.3.1 Slip System Resistance Components

Figures 4.3 (a), (b) and (c) shows the contours of slip system resistance because of SSDs, GNDs and the total slip system resistance respectively. Here we can see that the SSDs are mainly evolved in the grain interior regions depending upon their orientation. We can also visualize the blue strips of lower g_{SSDs} values in the GB region due to the rate of shear getting penalized in this region with extra energy penalty as discussed in Chapter 2. While in contrast to SSDs, the GNDs are mainly concentrated in near GB region caused by stronger plastic strain gradient. The GNDs are having smaller values in the grain interior regions which are governed by homogeneous plastic deformation. The total slip system resistance is shown to have the combined effect of SSDs and GNDs in which the values in grain interior regions is defined by grain orientation controlled by SSDs while in near GB region it is dependent on misorientation across interfaces controlled by GNDs.



(a)



(b)

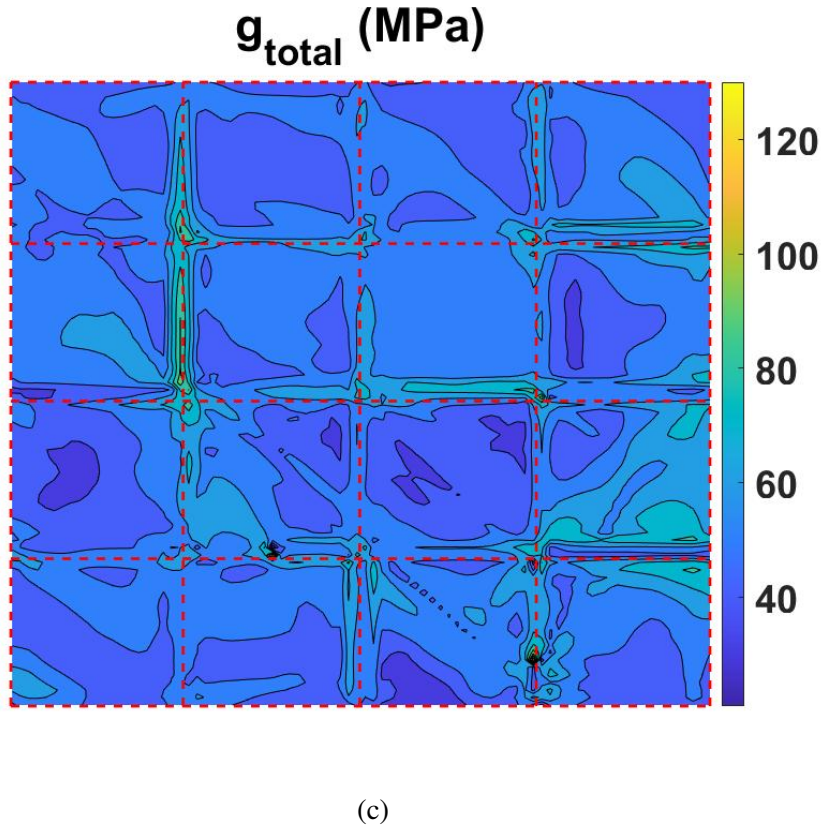
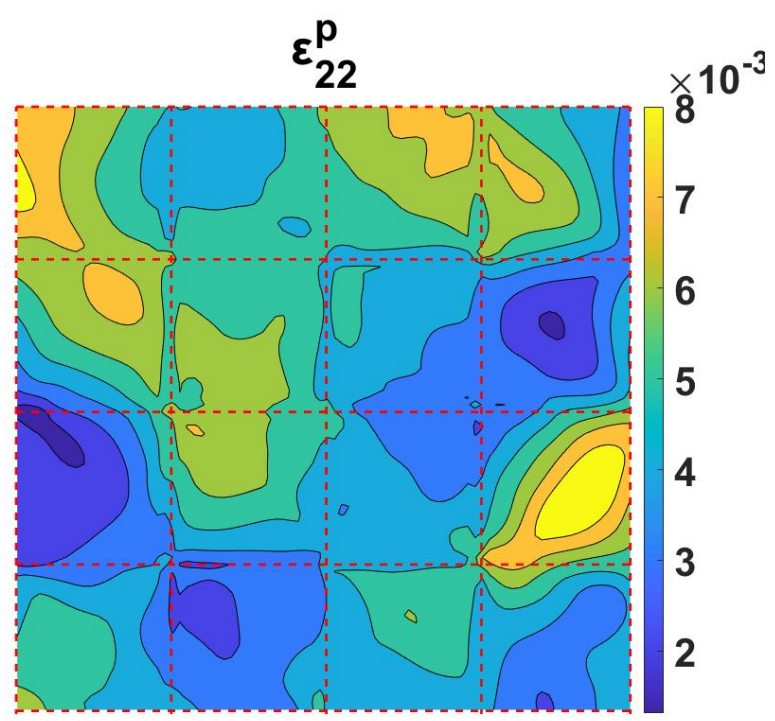
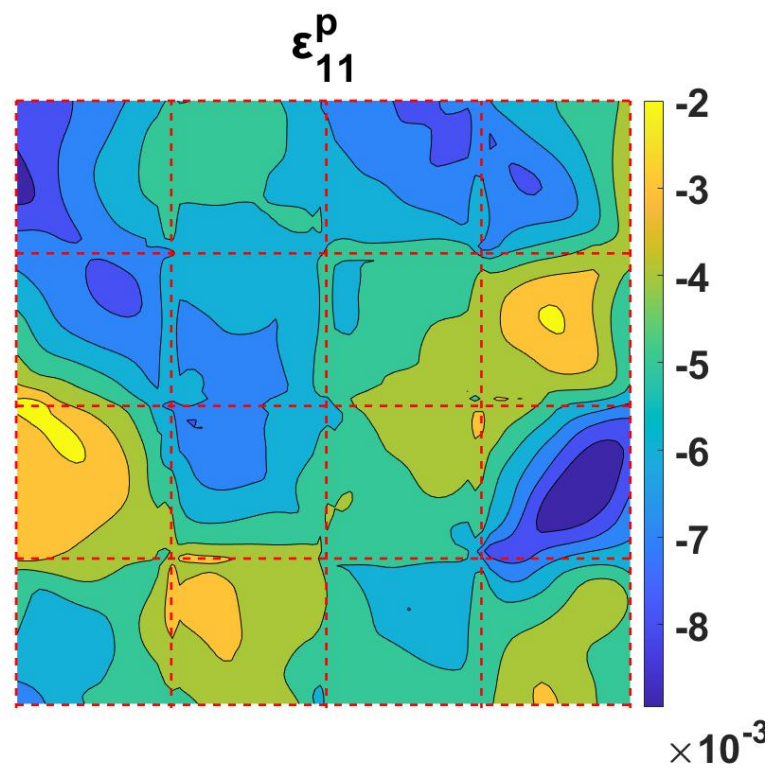


Figure 4.3: Spatial distribution of maximum slip system resistance amongst all the slip systems at applied strain of 0.5%. (a) g_{SSD} , (b) g_{GND} , and (c) total slip resistance.

4.3.2 Components of Plastic Strain

Figures 4.4 (a), (b), (c) and (d) shows the contours of plastic strain components ϵ_{11}^P , ϵ_{22}^P , ϵ_{33}^P and ϵ_{12}^P respectively. We can verify that the ϵ_{33}^P is small, due to plane stain condition. Moreover depending upon the loading condition i.e. uniaxial tensile deformation the shear strain component is also ϵ_{12}^P small. Here ϵ_{22}^P is dominant strain component since the polycrystal domain is deformed in the 22 direction. The contours also show that the grains with higher euler angle have undergone lesser plastic deformation. The compressive strain ϵ_{11}^P is appearing because of the lateral deformation to satisfy the isochoric condition of plastic flow.



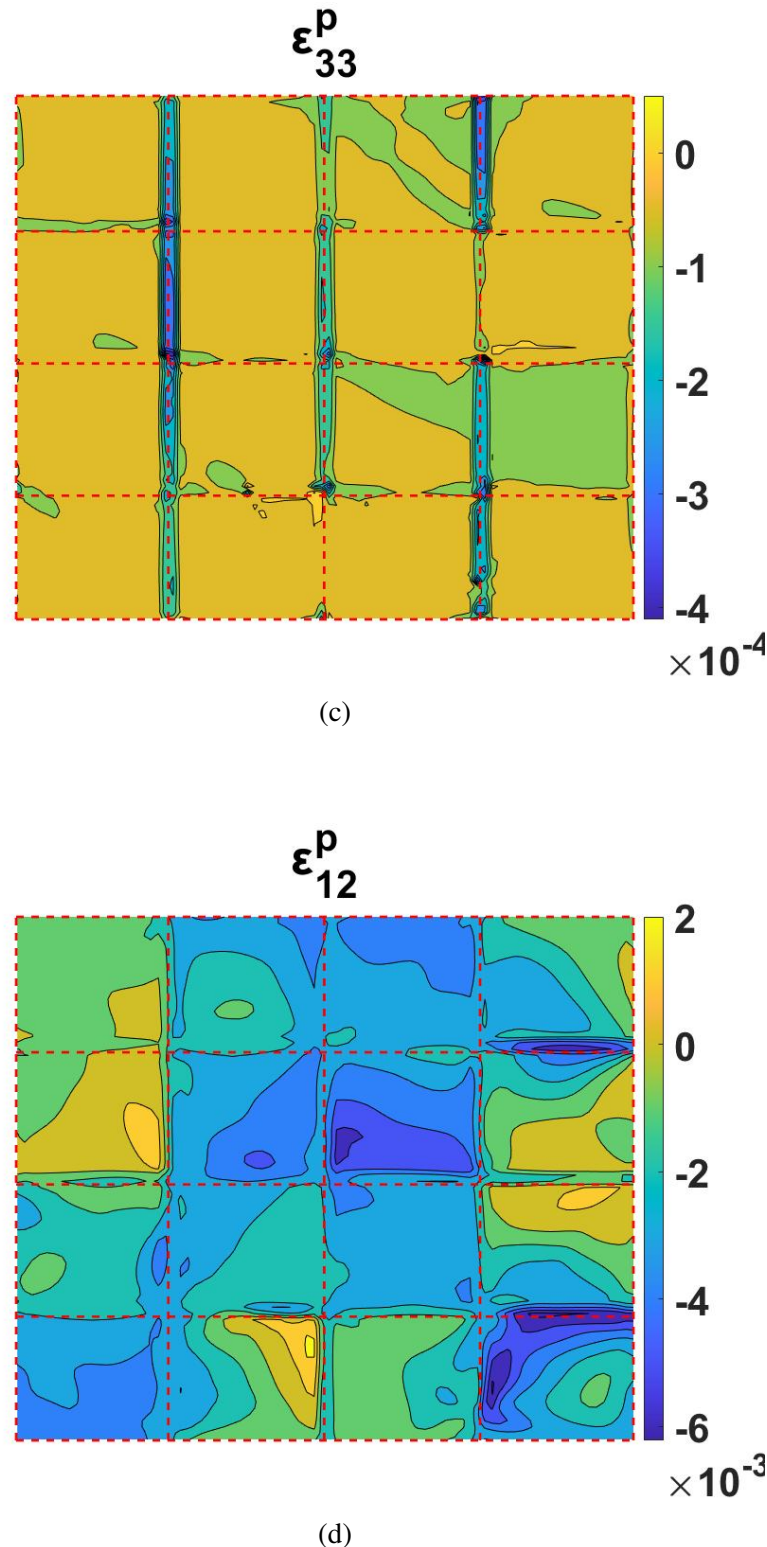
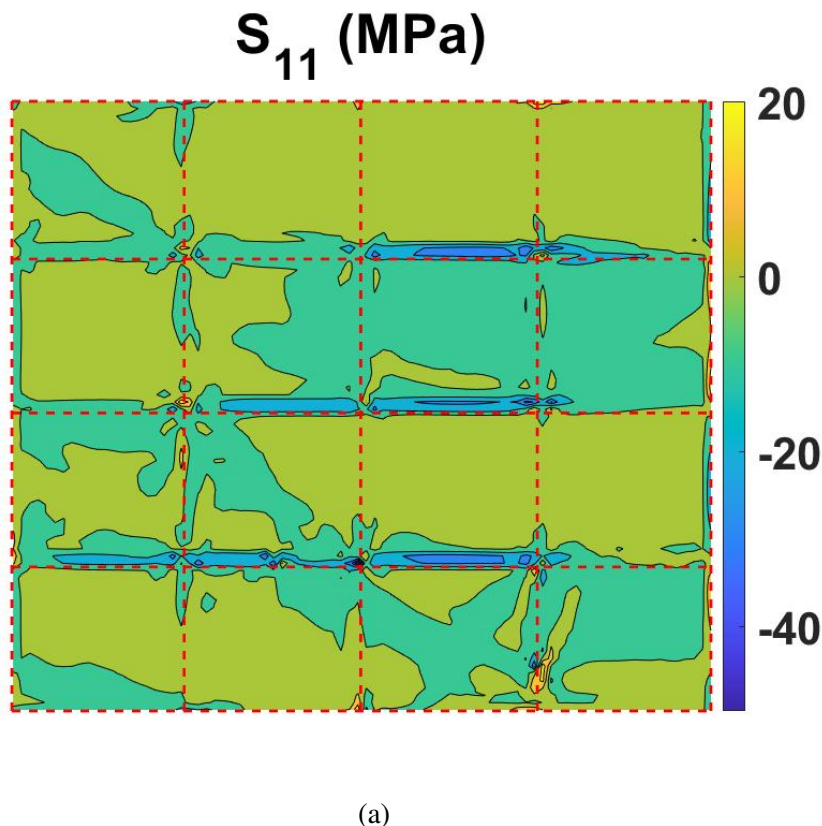
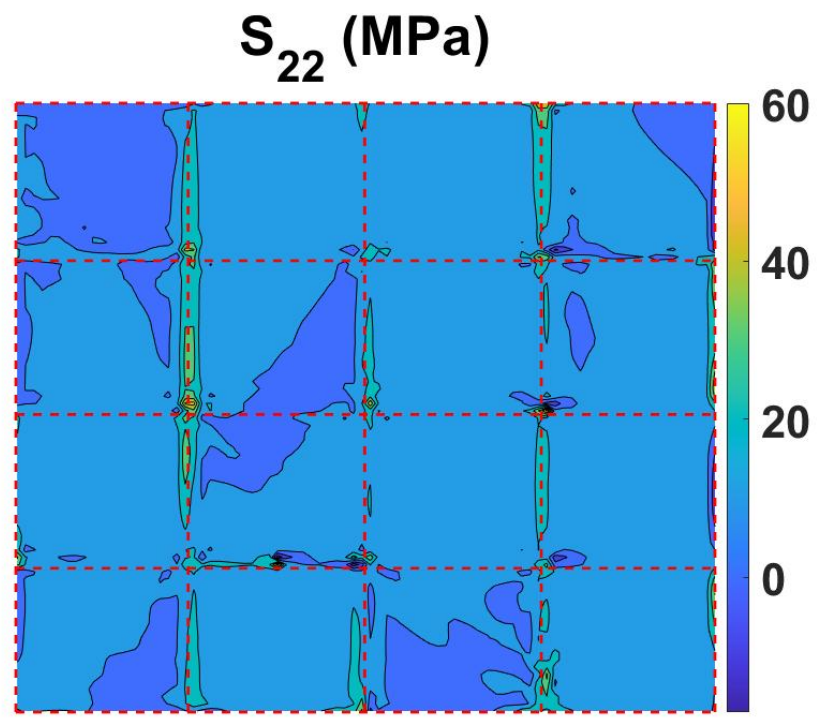


Figure 4.4: Spatial distribution of components of plastic strain (a) ϵ_{11}^p , (b) ϵ_{22}^p , (c) ϵ_{33}^p and (d) ϵ_{12}^p for uniaxial plane strain deformation of polycrystal at applied strain of 0.5%.

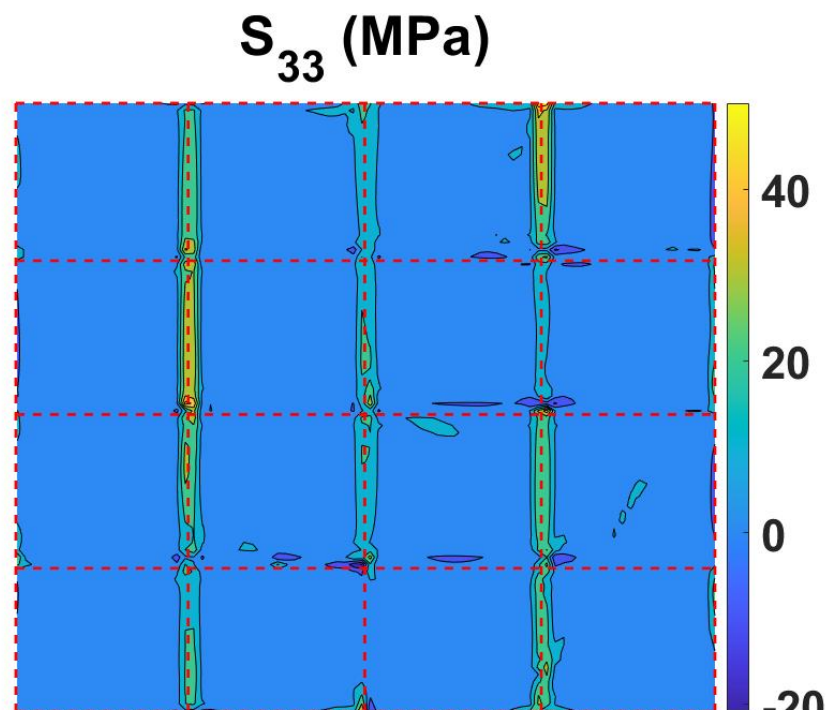
4.3.3 Components of Stress

The four stress components of stresses σ_{11} , σ_{22} , σ_{33} and σ_{12} are shown below in Figure 4.5. Since the shear strain component of plastic strain was shown to be very small in previous section (see Figure 4.4 (d)) , the σ_{12} component also appears to be small. Moreover, by the applied macroscopic boundary conditions described in Section 3.1, both left and right faces of domain are free surface therefore to maintain the stress equilibrium in 11 direction, the σ_{11} components gets balanced to a nearly zero value. σ_{22} and σ_{33} are having significant values resulting from ϵ_{22}^e and ϵ_{33}^e component of elastic strain.





(b)



(c)

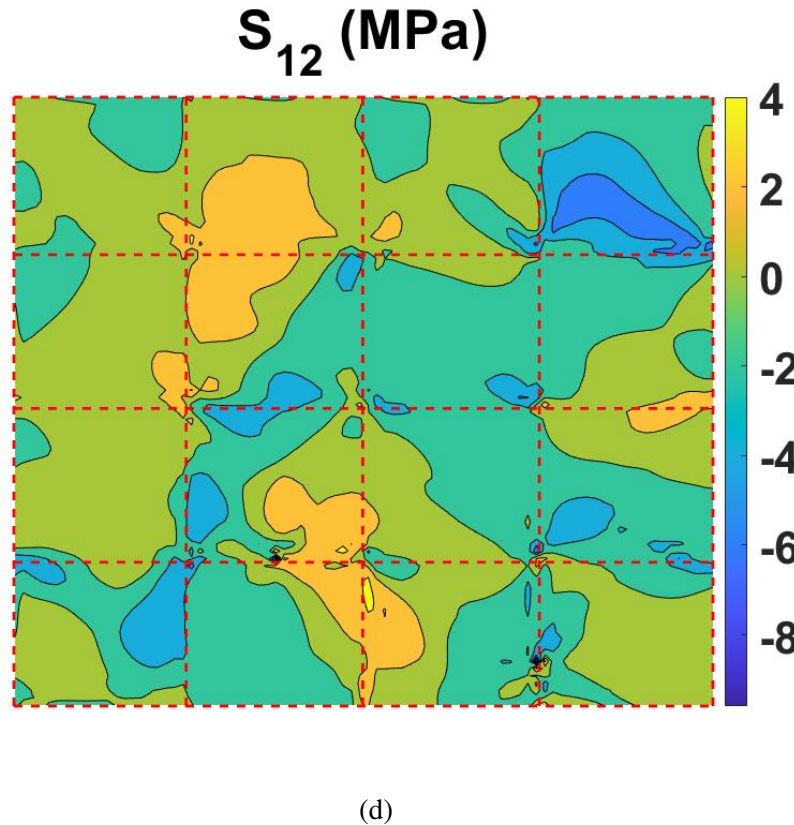
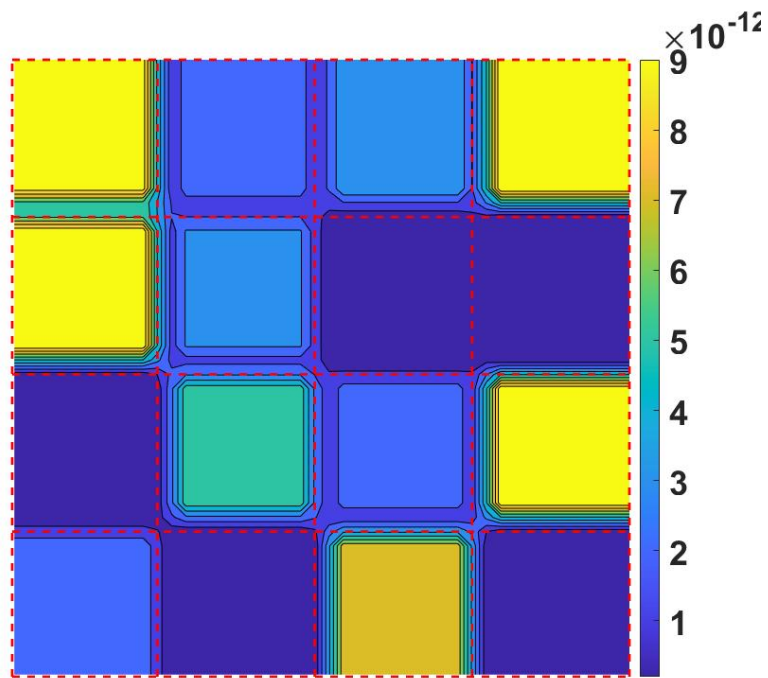
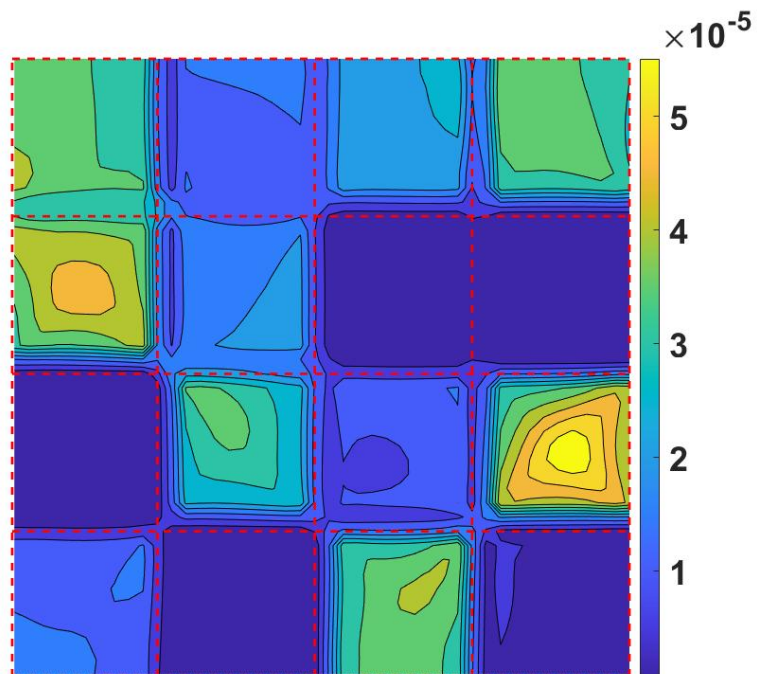


Figure 4.5: Spatial distribution of components of Cauchy stress (a) σ_{11} , (b) σ_{22} , (c) σ_{33} and (d) σ_{12} for uniaxial plane strain deformation of polycrystal at applied strain of 0.5%.

4.4 Orientation Dependent Yielding of Grains in a Polycrystal

As we have discussed in the beginning of this chapter, the various grains in a polycrystal start yielding in a selective sequential pattern depending upon their orientation. To demonstrate this, the contours of ϵ_{22}^P are shown at different strain levels viz. 0.01%, 0.05%, 0.1% and 0.3% in Figure 4.6. From these contours we can visualize that for 0.01% strain none of the grains have yielded, while when reaching at 0.05% the grains with preferential orientations have slowly started yielding. At 0.1% more number of grains appear to be start yielding while at 0.3% almost all the grains have yielded by some amount.

(a) ϵ_{22}^P at 0.01% strain(b) ϵ_{22}^P at 0.05% strain

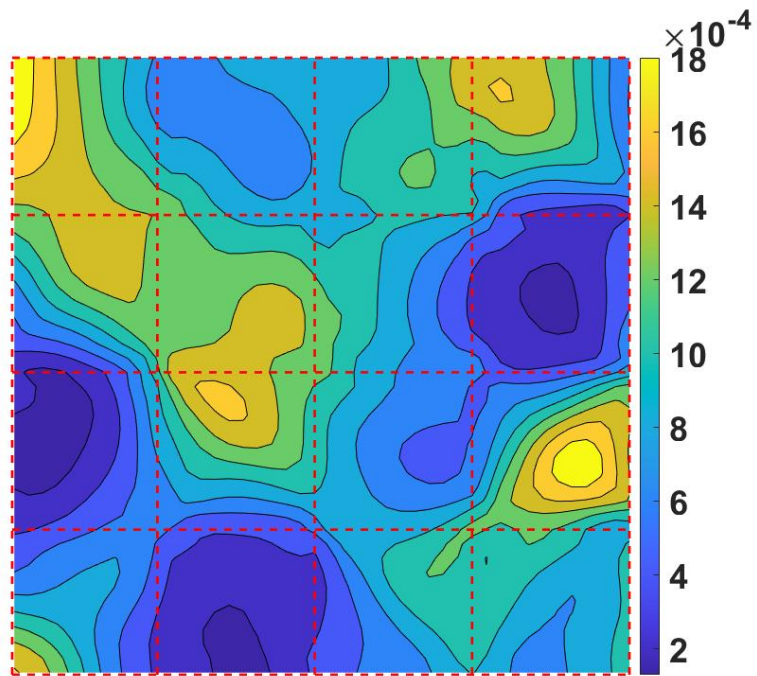
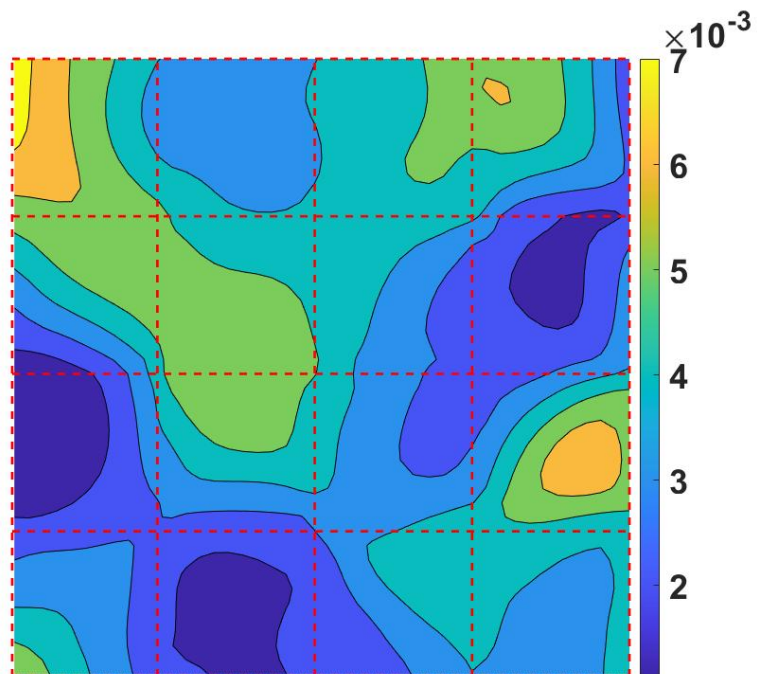
(c) ϵ_{22}^P at 0.1% strain(d) ϵ_{22}^P at 0.3% strain

Figure 4.6: Orientation dependent yielding of grains.

4.5 Discussion of Experimentally Observed Hall-Petch Effect

The effect of grain size on the elasto-plastic deformation behaviour of metallic alloys is experimentally verified in many of the references available in the literature. The material parameters chosen in this work are for annealed aluminum. Z.N Farhat et al. [21] have reviewed the various experimental studies of Hall-Petch effect on aluminum with varying impurity level and range of grain diameters. The table shown below is taken from [21] in which they have provided the citations for individual studies.

Table 4.2: Comparision of Hall-Petch parameters for Aluminum

Material	σ_0 (MPa)	K (MPa $m^{0.5}$)	Grain size(μm)
99.97% Al	15.0	0.07	20 – 150
99.999% Al	15.5	0.04	150 – 250
99.99% Al	22.4	0.07	30 – 100
1100 Al	14.3	0.07	20 – 200
Al – 6% Ni	11.0	0.14	0.5 – 20

The table shows that the value of the Hall-Petch slope for Aluminum alloys varies from $0.04 \text{ MPa } m^{0.5}$ to $0.07 \text{ MPa } m^{0.5}$, depending upon composition and range of grain sizes. N.Hansen et al. [20] have verified experimentally that the Hall- Petch slope increases with increasing strain level. The Hall-Petch slope obtained in our simulation for the polycrystal is of the range $0.035 \text{ MPa } m^{0.5}$ at 0.5% strain which also increases with the increasing strain level. The value is close to the experimentally observed range of values. Similarly the Hall-Petch slope from our bicrystal simulations typically varied from $0.025 \text{ MPa } m^{0.5}$ for smaller misorientation of grains to $0.95 \text{ MPa } m^{0.5}$ for high misorientation. The polycrystals simulation showed an intermediate value when compared with bicrystal results because in the polycrystal domain a mix of low and high misoriented grains are present. Therefore, we can verify that the results of simulations are close

to experimentally observed data. However, the accuracy of simulation results can still be improved by calibrating various modelling parameters.

CHAPTER 5

Conclusion and Future Scope

5.1 Conclusion

CPFEM based diffused interface model including the GB physics to study the polycrystal micro-mechanics is developed in this thesis. An improvement is made to the conventional sharp or stepped interface representation of the interface region by introducing a finitely thick GB region which incorporates the properties of all the adjoining grains. A modified flow rule is developed to incorporate the GB dislocation interaction mechanism. A slip transmission model has been developed considering a triple point and is schematically elaborated. The distribution of slip rate between the slip system of various constituent grains in GB region resulting from dislocation transmission across the GB is shown and discussed. The GB barrier is modelled by introducing an extra energy penalty term in the slip rate equation. This energy penalty is based on minimizing the remnant dislocation line on GB for incoming and outgoing slip systems. The energy penalty is also allowed to evolve with accumulated slip which models the change in characteristics of GB region due to increased concentration of dislocation debris left behind during slip transmission events across GBs. For capturing the plastic strain gradient developed because of the GBs and prevent lattice compatibility GNDs are also incorporated in the model in addition to the SSDs. The slip resistance caused by GNDs is calculated in terms of Nye dislocation density tensor. The numerical technique to calculate the Nye tensor and CPFEM implementation of the model is also presented. The actual three dimensional slip systems of a FCC crystal are reduced to 8 pseudo slip systems for analysing the problem in two dimensional plane strain.

The model is used to perform various case studies of bicrystal and polycrystal domains subjected to uniaxial plane strain tensile deformation. Model parameters for getting accurate results are determined using various convergence studies. The mesh sensitivity

analysis shows that the macroscopic stress-strain responses are almost converged for the elements size less than or equal to $1\mu m \times 1\mu m$. The converged time step size which produces accurate results with minimal computational effort is found to be less than or equal to 0.001 second. From the convergence study performed for determining the optimal physical GB thickness of GB region, it is concluded that the macroscopic responses are almost converged if the chosen thickness of GB region is less than or equal to 2% of grain diameter.

The independence of GB resistance to relative orientation of grains is verified by analysing the results of the case study where the spatial distribution of grains is varied keeping the relative misorientation to be constant. The single crystal effect is also verified where it is observed that a bicrystal with zero misorientation behaves as a single crystal. The evolution of the energy penalty has shown to produce stronger strain hardening effect. The Hall-Petch effect is verified for the bicrystal problem, which shows that crystals have smaller grain size have higher yield strength. Moreover, it is also observed that higher misorientation between the grains across GB produces higher strain hardening slope. The obtained Hall-Petch slope also increases with the strain. The variation of various local response parameters is also presented using contour and line plots. It is observed that SSDs mainly evolve in the grain interior regions where the motion of dislocations is easy and intensive. However, the GNDs are concentrated in the near GB region due to the gradient of plastic strain developed by the GBs. The variation of accumulated slip for individual slip systems of a bicrystal is studied which shows that some of the slip systems are getting activated while a few of them remain inactive during the deformation process. From the contour and line plots of various stress and plastic strain components, it is observed that the GB region have smaller plastic deformation compared to grain interiors resulting in stress concentration in the near GB region.

Orientation dependent yielding of grains in polycrystals is observed which shows that depending upon their orientations various grains of a polycrystal yield progressively. The dependence of polycrystal yield strength on grain size is observed to follow the Hall-Petch behaviour. Moreover, the evaluated Hall-Petch slope increases with increasing strain level. The local variation of slip system resistance shows that the deformation behaviour

in the grain interior regions is controlled by SSDs while the influence of GNDs is concentrated in the near GB region. The comparison of obtained simulation results with the experimental observation in literature shows that the model is able to capture the Hall-Petch behaviour in polycrystals with good accuracy. However, various modelling parameters can be better calibrated to match with the experimental results.

5.2 Scope of Future Work

The current work can be extended in future in the below mentioned possible ways

- Executing polycrystal simulations with uniform mesh becomes computationally inefficient. Developing a biased meshing technique can significantly reduce the simulation time.
- Two-dimensional computations may predict a too simplified material response that is far from the actual crystal behavior. Therefore, the model should be extended to 3D for capturing realistic deformation behavior in crystals.
- The grain boundary model can be improved by checking the direction of dislocation motion to ensure that the energy penalty is applied only for the dislocations moving towards the GB.
- The developed CPFEM model should be implemented in *Umat* to use it with commercial simulation softwares.

REFERENCES

- [1] G. I. Taylor. Plastic strain in metals. *Journal of the Institute of Metals*, 62:307–324, 1938.
- [2] A.Needleman, R.J.Asaro, and J.Lemnonds. Finite element analysis of crystalline solids. *Computer Methods in Applied Mechanics and Engineering*, 52:689–708, 1985.
- [3] SV Harren and RJ Asaro. Nonuniform deformations in polycrystals and aspects of the validity of the taylor model. *Journal of the Mechanics and Physics of Solids*, 37:191–232, 1989.
- [4] E Kroner. Zur plastischen verformung des vielkristalls. *Acta metallurgica*, 9:155–161, 1961.
- [5] Budiansky, Bernard, and TAI TE WU. Theoretical prediction of plastic strains of polycrystals. Technical report, Harvard University, Cambridge, Massachusetts, 1961.
- [6] S.R. Kalidindi, C.A. Bronkhorst, and L. Anand. Crystallographic texture evolution in bulk deformation processing of fcc metals. *Journal of the Mechanics and Physics of Solids*, 40:537–569, 1992.
- [7] A. Ma and F. Roters. A constitutive model for fcc single crystals based on dislocation densities and its application to uniaxial compression of aluminium single crystals. *Acta Materialia*, 52:3603–3612, 2004.
- [8] F. Roters, P. Eisenlohr, L. Hantcherli, D.D. Tjahjanto, T.R. Bieler, and D. Raabe. Overview of constitutive laws, kinematics, homogenization and multiscale methods in crystal plasticity finite-element modeling: Theory, experiments, applications. *Acta Materialia*, 58:1152–1211, 2010.
- [9] Sarra Haouala, Javier Segurado, and Javier LLorca. An analysis of the influence of grain size on the strength of fcc polycrystals by means of computational homogenization. *Acta Materialia*, 148:72–85, 2018.
- [10] Srihari Balasubramanian. *Polycrystalline plasticity: application to deformation processing of lightweight metals*. PhD thesis, Massachusetts Institute of Technology, 1998.
- [11] E. O. Hall. The deformation and ageing of mild steel: Iii discussion of results. *Proceedings of the Physical Society. Section B*, 64:747–753, 1951.

- [12] N. J. Petch. The cleavage strength of polycrystals. *Journal of the Iron and Steel Institute*, 174:25–28, 1953.
- [13] M.F. Ashby. The deformation of plastically nonhomogenous materials. *Philosophical Magazine*, 21:399–424, 1970.
- [14] J.P. Hirth. The influence of grain boundaries on mechanical properties. *Metallurgical Trans.*, 3:3047–3067, 1972.
- [15] L.P. Evers, D.M. Parks, W.A.M. Brekelmans, and M.G.D. Geers. Crystal plasticity model with enhanced hardening by geometrically necessary dislocation accumulation. *Journal of the Mechanics and Physics of Solids*, 50:2403–2424, 2002.
- [16] W.A. Soer, K.E. Aifantis, and J.Th.M. De Hosson. Incipient plasticity during nanoindentation at grain boundaries in body-centered cubic metals. *Acta Materialia*, 53:4665–4676, 2005.
- [17] Hong Dai. *Geometrically necessary dislocation density in continuum plasticity theory, FEM implementation and applications*. PhD thesis, Massachusetts Institute of Technology, 1997.
- [18] A. Ma, F. Roters, and D. Raabe. Studying the effect of grain boundaries in dislocation density based crystal-plasticity finite element simulations. *International Journal of Solids and Structures*, 43:7287–7303, 2006.
- [19] Masoud Anahid, Mahendra K. Samal, and Somnath Ghosh. Dwell fatigue crack nucleation model based on crystal plasticity finite element simulations of polycrystalline titanium alloys. *Journal of the Mechanics and Physics of Solids*, 59:2157–2176, 2011.
- [20] N. Hnasen. The effect of grain size and strain on the tensile flow stress of aluminium at room temperature. *Acta Metallurgica*, 25:863–869, 1977.
- [21] Z.N. Farhat, Y. Ding, D.O. Northwood, and A.T. Alpas. Effect of grain size on friction and wear of nanocrystalline aluminum. *Materials Science and Engineering*, A206:302–313, 1996.
- [22] N. A. Fleck, G. M. Muller, M. F. Ashby, and J. W. Hutchinson. Strain gradient plasticity: theory and experiment. *Acta Metall. Mater*, 42:475–487, 1994.
- [23] S.H. Chen and T.C. Wang. A new hardening law for strain gradient plasticity. *Acta mater*, 48:3997–4005, 2000.
- [24] Atefeh Alipour, Stefanie Reese, and Stephan Wulffinghof. A grain boundary model for gradient-extended geometrically non-linear crystal plasticity: Theory and numerics. *International Journal of Plasticity*, 118:17–35, 2019.
- [25] Waseem Amin, Muhammad Adil Ali, Napat Vajragupta, and Alexander Hartmaier. Studying grain boundary strengthening by dislocation-based strain gradient crystal plasticity coupled with a multi-phase-field model. *Materials*, 12:2977, 2019.

- [26] S. Haouala, S. Lucarini, J. LLorca, and J. Segurado. Simulation of the hall-petch effect in fcc polycrystals by means of strain gradient crystal plasticity and fft homogenization. *Journal of the Mechanics and Physics of Solids*, 134:103755, 2020.
- [27] William A. Counts, Michael V. Braginsky, Corbett C. Battaile, and Elizabeth A. Holm. Predicting the hall–petch effect in fcc metals using non-local crystal plasticity. *International journal of plasticity*, 24:1243–1263, 2008.
- [28] L. P. Evers, W. A. M. Brekelmans, and M. G. D. Geers. Scale dependent crystal plasticity framework with dislocation density and grain boundary effects. *International Journal of Solids and Structures*, 41:5209–5230, 2004.
- [29] Risabh D. Guha, Arnab J. Sharma, Pranaydhar Diwan, and Prasenjit Khanikar. Effect of grain orientation on high strain rate plastic deformation. *Procedia engineering*, 173:1048–1055, 2017.
- [30] S. Haouala, R. Alizadeh, T. R. Bieler, J. Segurado, and J. LLorca. Effect of slip transmission at grain boundaries in al bicrystals. *International Journal of Plasticity*, 126:102600, 2020.
- [31] A. Ma, F. Roters, and D. Raabe. On the consideration of interactions between dislocations and grain boundaries in crystal plasticity finite element modeling – theory, experiments, and simulations. *Acta Materialia*, 54:2181–2194, 2006.
- [32] Xiang-Long Peng, Gan-Yun Huang, and Swantje Bargmann. Gradient crystal plasticity: A grain boundary model for slip transmission. *Materials*, 12:3761, 2019.
- [33] Long-Qing Chen and Yunzhi Wang. The continuum field approach to modeling micro-structural evolution. *The Journal of the Minerals*, 48:13–18, 1996.
- [34] Hojun Lim, Fadi Abdeljawad, Steven J Owen, Byron W Hanks, James W Foulk, and Corbett C Battaile. Incorporating physically-based microstructures in materials modeling: Bridging phase field and crystal plasticity frameworks. *Modelling Simul. Mater. Sci. Eng.*, 24:045016, 2016.
- [35] Robert J. Asaro. Geometrical effects in the inhomogeneous deformation of ductile single crystals. *Acta Metallurgica*, 27:445–453, 1979.
- [36] Jeffrey W. Kysar, Yong X. Gan, and Gilberto Mendez-Arzuza. Cylindrical void in a rigid-ideally plastic single crystal. part i: anisotropic slip line theory solution for face-centered cubic crystals. *International Journal of Plasticity*, 21:1481–1520, 2005.
- [37] Christian F. Niordson and Jeffrey W. Kysar. Computational strain gradient crystal plasticity. *Journal of The Mechanics and Physics of Solids*, 62:31–47, 2014.
- [38] Mitsutoshi Kuroda. Description of plane strain deformation of fcc crystals by a gradient theory of crystal plasticity. *Extreme Mechanics Letters*, 44:101221, 2021.

- [39] James R. RICE. Tensile crack tip fields in elastic-ideally plastic crystals. *Mechanics of Materials*, 6:317–335, 1987.
- [40] K.J.Juul, K.L.Nielsen, and C.F.Niordson. Steady-state crack growth in single crystals under mode i loading. *Journal of The Mechanics and Physics of Solids*, 101:209–222, 2017.
- [41] J.W. Kysar, Y. Saito, M.S. Oztop, D. Lee, and W.T. Huh. Experimental lower bounds on geometrically necessary dislocation density. *International Journal of Plasticity*, 26:1097–1123, 2010.
- [42] Craig S. Hartley and Jeffrey W. Kysar. Plane strain deformation by slip in fcc crystals. *Journal of The Mechanics and Physics of Solids*, 133:102842, 2020.